

## High pressure fluidization

**Citation for published version (APA):**

Godlieb, W. (2010). *High pressure fluidization*. [Phd Thesis 2 (Research NOT TU/e / Graduation TU/e), Chemical Engineering and Chemistry]. Technische Universiteit Eindhoven. <https://doi.org/10.6100/IR693317>

**DOI:**

[10.6100/IR693317](https://doi.org/10.6100/IR693317)

**Document status and date:**

Published: 01/01/2010

**Document Version:**

Publisher's PDF, also known as Version of Record (includes final page, issue and volume numbers)

**Please check the document version of this publication:**

- A submitted manuscript is the version of the article upon submission and before peer-review. There can be important differences between the submitted version and the official published version of record. People interested in the research are advised to contact the author for the final version of the publication, or visit the DOI to the publisher's website.
- The final author version and the galley proof are versions of the publication after peer review.
- The final published version features the final layout of the paper including the volume, issue and page numbers.

[Link to publication](#)

**General rights**

Copyright and moral rights for the publications made accessible in the public portal are retained by the authors and/or other copyright owners and it is a condition of accessing publications that users recognise and abide by the legal requirements associated with these rights.

- Users may download and print one copy of any publication from the public portal for the purpose of private study or research.
- You may not further distribute the material or use it for any profit-making activity or commercial gain
- You may freely distribute the URL identifying the publication in the public portal.

If the publication is distributed under the terms of Article 25fa of the Dutch Copyright Act, indicated by the "Taverne" license above, please follow below link for the End User Agreement:

[www.tue.nl/taverne](http://www.tue.nl/taverne)

**Take down policy**

If you believe that this document breaches copyright please contact us at:

[openaccess@tue.nl](mailto:openaccess@tue.nl)

providing details and we will investigate your claim.

## **High Pressure Fluidization**

Samenstelling promotiecommissie:

prof.dr. P.J. Lemstra	Eindhoven University of Technology
prof.dr.ir. J.A.M. Kuipers, promotor	Eindhoven University of Technology
dr.ir. N.G. Deen, assistent promotor	Eindhoven University of Technology
prof.dr.-Ing habil. S.Heinrich	Hamburg University of Technology
prof.dr.ir. J.C. Schouten	Eindhoven University of Technology
prof.dr.ir. G.J.F. van Heijst	Eindhoven University of Technology
dr.ir. J.R. van Ommen	Technische Universiteit Delft
dr.ir. B.P.B. Hoomans	DSM

The research in this thesis was financially supported by the Dutch Polymer Institute (DPI), the Netherlands.

© W. Godlieb, Enschede, The Netherlands, 2010

No part of this work may be reproduced in any form by print, photocopy or any other means without written permission from the author.

Publisher: *Ipskamp Drukkers B.V.*, P.O box 333, 7500 AH, Enschede, the Netherlands

ISBN: 978-90-386-2407-5

# High Pressure Fluidization

## PROEFSCHRIFT

ter verkrijging van de graad van doctor aan de  
Technische Universiteit Eindhoven, op gezag van de  
rector magnificus, prof.dr.ir. C.J. van Duijn, voor een  
commissie aangewezen door het College voor  
Promoties in het openbaar te verdedigen  
op maandag 13 december 2010 om 14.00 uur

door

Willem Godlieb

geboren te Groningen

Dit proefschrift is goedgekeurd door de promotor:

prof.dr.ir. J.A.M. Kuipers

Copromotor:

dr.ir. N.G. Deen





# Contents

<b>Summary</b>	<b>1</b>
<b>Samenvatting</b>	<b>5</b>
<b>1 Introduction</b>	<b>9</b>
1.1 Fluidization . . . . .	9
1.2 Objective . . . . .	11
1.3 Modelling fluidized beds . . . . .	11
1.4 Experimental investigation of fluidization . . . . .	13
1.5 Organisation of the thesis . . . . .	14
<b>2 Numerical methods</b>	<b>15</b>
2.1 Introduction . . . . .	15
2.2 Discrete particle model . . . . .	18
2.3 Two-fluid model . . . . .	31
2.4 Computing hardware . . . . .	35
<b>3 Electrical capacitance tomography</b>	<b>37</b>
3.1 Introduction . . . . .	37
3.2 Basic principle . . . . .	39
3.3 Calibration . . . . .	44
3.4 Reconstruction . . . . .	47
3.5 Concentration models . . . . .	54
3.6 Conclusion . . . . .	58
<b>4 Particle and bubble behaviour in fluidized beds at elevated pressure</b>	<b>61</b>
4.1 Introduction . . . . .	61
4.2 Governing equations . . . . .	62
4.3 Simulation settings . . . . .	63
4.4 Results . . . . .	64
4.5 Conclusions . . . . .	82
<b>5 Solids mixing in fluidized beds at elevated pressure</b>	<b>85</b>
5.1 Introduction . . . . .	85
5.2 Governing equations . . . . .	86



5.3	Methods for characterizing mixing . . . . .	90
5.4	Simulation settings . . . . .	102
5.5	DPM results . . . . .	103
5.6	TFM results . . . . .	107
5.7	Discussion and conclusions . . . . .	114
<b>6</b>	<b>Experimental study of large scale fluidized beds at elevated pressure</b>	<b>117</b>
6.1	Introduction . . . . .	117
6.2	Experimental set-up . . . . .	119
6.3	Results . . . . .	127
6.4	Conclusion . . . . .	142
<b>7</b>	<b>Epilogue</b>	<b>143</b>
7.1	Comparison of models and experiments . . . . .	143
7.2	Effects of pressure . . . . .	146
7.3	Outlook . . . . .	149
	<b>Nomenclature</b>	<b>151</b>
	<b>Bibliography</b>	<b>154</b>
	<b>List of publications</b>	<b>163</b>
	<b>Curriculum Vitae</b>	<b>165</b>

# Summary

Polymers are often produced in pressurized fluidized beds. Large surface area and good mixing properties are key advantages of a fluidized bed. Despite decades of research, fluidization is still not completely understood. Especially since most academic research on fluidized beds is performed at atmospheric conditions. The objective of this work is to gain knowledge on fluidization of polymeric particles at elevated operating pressure, employing a combined modelling and experimental approach.

The discrete particle model (DPM) and the two-fluid model (TFM) are used to gain detailed information of porosity distribution, bubble properties and solids mixing. Electrical capacitance tomography (ECT) was used to measure porosity distributions in a 30 cm diameter gas-fluidized bed. ECT is a relatively cheap and fast technique based on the difference in permittivity of air and polymeric particles. ECT requires a sophisticated reconstruction technique, for which the Landweber [1951] iteration method was used in this work. Since the permittivity and porosity are not linearly correlated, a concentration model is needed. In this work, an inverted Maxwell model is used for this purpose, since it represents the bubble emulsion structure best.

Since opening and emptying the pressure vessel requires about 2 days, an advanced calibration method was developed to prevent frequent opening of the vessel. In this approach the permittivity of a packed bed is measured at the beginning and at the end of each measurement. If the calibration has changed during the measurement, the measurement is not used.

Solids mixing is key in industrial reactors, since it prevents hot spots, it prevents undesired clustering and it ensures mixed product removal. Solids mixing is investigated using the DPM and TFM. A new method to quantify the degree of mixing based on the distance between particles and their initial neighbour was developed. The initial neighbour method performed better than existing methods since it is independent of the computational grid and the particle colouring, it can be used in all directions and it is highly reproducible.

With increasing pressure six observations were made, which are explained below

**Emulsion phase becomes more porous.**

The emulsion phase becomes more porous with increasing operating pressure. At atmospheric operating pressure the porosity of the emulsion phase is similar to the porosity of a randomly packed bed (0.4), while at 20 bar the porosity of the emulsion phase rises to 0.5.

**Bubble-emulsion structure becomes less distinct.**

In both simulations and experiments it is observed that the clear distinction between bubbles and the emulsion phase gradually disappears with increasing pressure. At atmospheric pressure the emulsion phase is dense and the bubbles are clear voids containing little particles. At high pressure it is no longer possible to observe separate bubbles, although dense and porous regions in the bed still prevail, intermediate porosities occur as frequent compared to low pressure.

**Fluidization is more vigorous and bubbles behave more chaotic.**

From animations of simulations results (pressure drop fluctuations and bubble properties) it was observed that the fluidization is more vigorous at elevated pressure. Bubbles move chaotically through the bed and bubbles coalescence and break-up takes place frequently, although it is hard to distinct individual bubbles.

**(Micro) mixing is improved via increased granular temperature only caused by increased porosity.**

From DPM and TFM simulations it is observed that solids mixing is improved with increasing operating pressure. Based on DPM simulation results is found that this effect is caused by increased granular temperature. Granular temperature is not directly increased by the elevated operated pressure, but rather via the increased porosity of the emulsion phase, which creates more space for the neighbouring particles to attain different velocities.

**Bed expansion limits macro mixing.**

Micro mixing is mixing at the scale of individual bubbles, while macro mixing is at the scale of the entire bed. The micro mixing rate is in-

creased with pressure because of the increased granular temperature. For pressures below 8 bar, macro mixing is enhanced with increasing operating pressure. At higher pressures, the bed expands, which decreases the mixing rate, since particles have to travel larger distances before they can become fully mixed.



# Samenvatting

Polymere worden op grote schaal geproduceerd in wervelbedden. Wervelbedden zijn hiervoor zeer geschikt vanwege de grote oppervlakte volume verhouding en de goede menzeigenschappen. Alhoewel er al decennia lang onderzoek wordt gedaan aan wervelbedden is er nog altijd onvoldoende kennis over het stromingsgedrag in wervelbedden. Doordat academisch onderzoek zich vooral richt op experimenten bij atmosferische omstandigheden, ontbreekt er kennis over het effect van druk op fluïdisatie. Het doel van dit onderzoek is het verkrijgen van kennis over het effect van druk op fluïdisatie gedrag van polymeerdeeltjes door middel van computersimulaties en experimenten.

Met behulp van het discrete deeltjes model (DPM) en het "two-fluid" model (TFM) zijn porositeitsverdelingen, bel-eigenschappen en informatie over deeltjesmenging verkregen. Met behulp van elektrische capaciteits-tomografie (ECT) zijn in een 30 cm diameter wervelbed porositeitsverdelingen gemeten. ECT is een goedkope, snelle techniek die is gebaseerd op het verschil in diëlektrische constante (permittiviteit) tussen lucht en polymeer. De Landweber iteratie methode is gebruikt om vanuit de ECT metingen een porositeitsverdeling te reconstrueren. Omdat de permittiviteit niet lineair schaalt met de volumefractie, is een concentratie-model noodzakelijk. In dit proefschrift is hiervoor gebruik gemaakt van een geïnverteerd Maxwell model, omdat het de bellen en emulsie structuur het beste weergeeft.

Het openen, legen en sluiten van het drukvat kost ongeveer twee dagen. Een uitgebreide kalibratie techniek maakt het mogelijk te kalibreren, zonder dat regelmatig openen van het vat noodzakelijk is. Bij deze techniek wordt aan het begin en aan het einde van een experiment de permittiviteit van het met deeltjes gevulde bed gemeten. Als de waarde verandert gedurende de meting, wordt deze meting niet gebruikt.

Deeltjesmenging speelt een belangrijke rol in industriële reactoren. Het gaat lokale oververhitting tegen, voorkomt clustering van deeltjes en zorgt voor een goede deeltjesgrootteverdeling van het product. Met behulp van het DPM en TFM is deeltjesmenging onderzocht. Er is een

nieuwe methode ontwikkeld, waarmee de mate van menging wordt gekwantificeerd. Deze methode is gebaseerd op de verandering van de afstand tussen initiële buurdeeltjes. Deze methode geeft goede resultaten en is onafhankelijk van de numerieke celgrootte en deeltjeskleuring. De methode kan gebruikt worden in alle richtingen en geeft reproduceerbare resultaten.

Hieronder worden zes effecten van het verhogen van de druk genoemd.

### **De emulsiefase wordt poreuzer**

Bij verhoogde druk wordt de emulsiefase poreuzer. Bij atmosferische omstandigheden is de emulsiefase dicht gepakt ( $\epsilon=0.4$ ), terwijl bij 20 bar de porositeit van de emulsiefase stijgt tot 0.5.

### **Bellen en emulsiefase zijn moeilijker te onderscheiden**

Simulaties en experimenten laten zien, dat het onderscheid tussen bellen en de emulsiefase verdwijnt. Bij atmosferische omstandigheden zijn de bellen duidelijk herkenbaar, terwijl bij hogere druk afzonderlijke bellen niet meer herkenbaar zijn. Alhoewel bij hoge druk dicht gepakte en ijle gebieden nog steeds voorkomen, komen gebieden met een gemiddelde porositeit even vaak voor.

### **Fluïdisatie is heftiger en bellen bewegen chaotischer**

Uit animaties van simulatie resultaten (drukfluctuaties en belgedrag) blijkt dat fluïdisatie heftiger wordt. Individuele bellen moeilijk te herkennen en bewegen chaotisch door het bed.

**Verbetering van (micro) menging wordt slechts veroorzaakt door een verhoogde porositeit.**

Uit DPM en TFM simulaties blijkt dat deeltjes beter mengen bij verhoogde druk. Dit wordt veroorzaakt door een verhoogde granulaire temperatuur. De granulaire temperatuur wordt niet rechtstreeks beïnvloed door de druk, maar via de porositeit van de emulsiefase. Door de hogere porositeit hebben deeltjes meer ruimte om een andere snelheid aan te nemen dan de naastgelegen deeltjes.

### **Bed-expansie beperkt macro menging**

Micro menging is menging op het niveau van individuele bellen, terwijl macro menging zich afspeelt op de schaal van het gehele bed. Micro menging versnelt, doordat toenemende druk de granulaire temperatuur verhoogt. Tot ongeveer 8 bar neemt de mengsnelheid toe met toenemende druk. Bij een nog hogere druk verslechtert de mengsnelheid, omdat het bed expandeert. Deeltjes moeten grotere afstanden afleggen alvorens ze gemengd worden.





# 1

## Introduction

### 1.1 Fluidization

Fluidization refers to the suspension of granular material by a continuous fluid (gas or liquid). Fluidization is widely used in industry. A fluidized bed is a container with solid particles fed by an upwards gas stream from beneath. At a sufficiently high gas flow rate the gravity force acting on the particles is balanced by the drag force exerted by the gas. Particles in fluidized beds mimic boiling fluid behaviour with gas bubbles flowing through fluid-like emulsion phase consisting of particles. The fluid-like behaviour can be illustrated by the occurrence of horizontal free surface and the fact that the principle of communicating vessels apply. The main advantage of fluidized beds compared to other gas-solid equipment is the large surface area and good mixing properties. These properties lead to high mass transfer rates between the gas and solid phase, and a uniform temperature in the bed. Furthermore a fluidized bed can be operated continuously. The major drawback of fluidized beds is the lack of fundamental knowledge on the flow behaviour, which leads to difficulties in design, scale-up and troubleshooting.

It is known that there are different regimes of fluidization. At low gas velocities, gas flows through a stationary bed particles. With increasing flow rate the drag force becomes sufficient to support the

weight of the particles and void bubbles are formed. The velocity at which the drag force is equal to the gravitational force is called the minimum fluidization velocity ( $u_{mf}$ ). At even higher flow rate different regimes can be distinguished from a bubbling regime with boiling fluid-like behaviour, through a slugging bed with layers of particles and voids, through finally turbulent fluidization where particles move chaotically and no bubbles can be discerned. At very high flow rates particles are blown out of the bed, which is called pneumatic conveying regime.

Fluidization behaviour of particles is strongly dependent on particle size and density. Geldart [1973] developed a method to classify all particles into four categories dependent on size and density. In this thesis only Geldart B particles are used. A bed containing this type of particles starts to form bubbles at minimum fluidization velocity and does not exhibit a state of homogeneous expansion.

Fluidized beds are widely used in industry for a multitude of applications. Fluidized beds are used to dry granular material and in the production of for instance fertilizers and detergents. In oil refineries fluidized beds are used in the fluid catalytic cracking (FCC) process in which catalyst particles are fluidized. Polymers can be synthesised in several ways, but one of the main methods is in a fluidized bed. Linear low density polyethylene (LLDPE) and polypropylene (PP) are produced in fluidized beds at million tonnes per annum. Two competing reactor designs are used: the Unipol<sup>TM</sup> process and the Spheripol<sup>TM</sup> process. Both designs have a similar approach and are operated continuously. As can be seen in Figure 1.1, catalyst particles are introduced into the bed, which gradually grow to form polymeric particles. Part of the polymeric particles is withdrawn from the bed and can be sold as a product. From beneath, a gas mixture containing monomer (either ethylene or propylene) is used as fluidizing agent. Since the polymerization reaction is very exothermic and the catalyst is very active, it is required to remove heat from the reactor. Therefore only 5% of the gas is used for reaction, while the rest is used for cooling and subsequently recycled (low conversion per pass). To improve the cooling capacity of the fluidization agent, nitrogen and suitable induced condensing agents (such as: iso-pentane or hexane) are added. These components are introduced as a liquid into the bed, so the evaporation of these agents effectively remove reaction heat. Beside these measures, solids mixing is key in preventing hot spots,

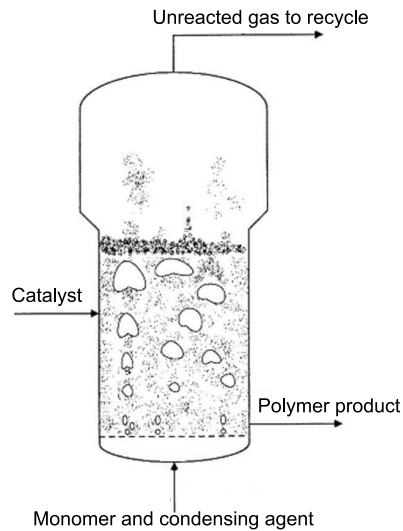


Figure 1.1: Schematic representation of the production of polymer in a fluidized bed.

which possibly leads to polymer degradation.

Industrial fluidized beds for the production of polymers operate at 20 to 25 bar to increase the reaction rate. Nevertheless, most research is performed at atmospheric conditions. Since the fluidization behaviour is known to change with the operating pressure, it is of paramount importance to study the effects of pressure based on first principles.

## 1.2 Objective

The objective of this project is to get a fundamental understanding of fluidization of polymeric particles at elevated operating pressures.

## 1.3 Modelling fluidized beds

In this thesis, computational models are used for the description of pressurized fluidized beds. These models comprise of computational

fluid dynamics (CFD) models, which are very powerful tools in addition to available experimental fluid dynamics (EFD) tools. With CFD data can be obtained in circumstances that are not obtainable otherwise. Furthermore, in CFD many fluid elements or particles can be continuously tracked and monitored, which is virtually impossible in EFD. In addition, it is rather simple to vary physical conditions in CFD or simulate even unphysical conditions. For example, extremely high pressures can be modeled by changing a single figure, whereas experiments at elevated pressures require special equipment. CFD has some drawbacks: thorough validation of CFD tools is time consuming. Furthermore, simulating large systems takes a lot of computational time and can only be done with confidence if proper modelling assumptions are made.

### 1.3.1 Multi-scale modelling

The multi-scale modelling approach comprises of different models of different levels of detail to describe relevant phenomena at different scales. For fluidized beds the multi-scale approach consists of a lattice Boltzmann model (LBM), a discrete particle model (DPM), a two-fluid model (TFM) and a discrete bubble model (DBM) (see Figure 1.2). Detailed models need little assumptions and closures, but can only simulate systems of limited size, while large scale models require many assumptions. With the LBM flow around individual particles is solved. From these simulations closures for the drag force are obtained, which are required in the DPM. In the DPM emulsion phase viscosity can be obtained which is used in the TFM. The DBM requires several closures for bubble break-up, bubble coalescence and bubble velocities. These can be obtained from DPM and TFM simulation.

In this thesis we used the discrete particle model (DPM) and the two-fluid model (TFM). We chose the DPM since it takes particle interaction into account in a detailed manner. It is important to describe the inter-particle interaction precisely as it competes with the gas-particle interaction which becomes increasingly important at elevated pressures. To study the fluidized bed behaviour in lab-scale systems we used the TFM. Both models will be discussed in detail in chapter 2.

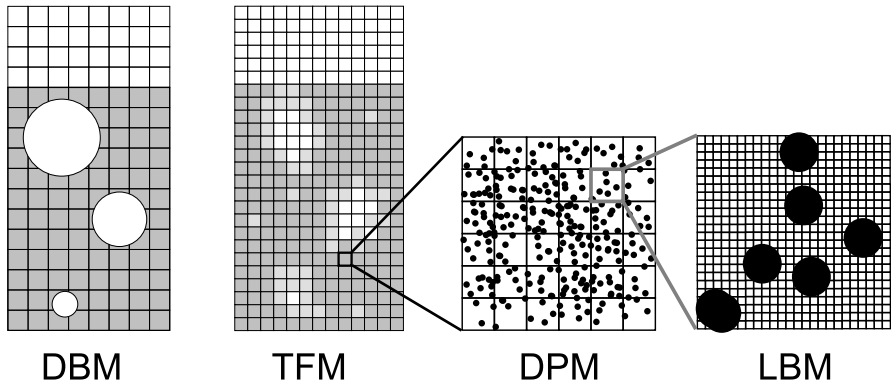


Figure 1.2: Multi-scale modelling for gas solid systems. Schematic representation of discrete bubble model (DBM), two-fluid model (TFM), discrete Particle Model (DPM) and Lattice Boltzmann Model (LBM). From left to right models have increased level of detail, require less closures and need more computational time. (Based on Van der Hoef et al. [2008])

## 1.4 Experimental investigation of fluidization

Many multiphase flow systems are not optically accessible. For experimental investigation of these systems optical techniques can only be used in a few special cases. More often however one needs to resort to non-optical techniques, in which 2D slices are obtained of phase fraction distributions in a multiphase system. There are several of these techniques available, such as Computer Aided Tomography (CAT-scan also known as X-ray tomography), Positron emission tomography (PET), Magnetic resonance imaging (MRI), Ocean acoustic tomography (Sonar), electrical capacitance tomography (ECT) and electrical resistance tomography (ERT). In this work we use ECT because it is a relatively cheap technique. Furthermore, ECT is a safe technique, where no radiation is present or dedicated technicians are required unlike CAT and MRI. Moreover, it is a fast technique that is able to measure at 100 Hz. There are three main drawbacks of ECT: contrary to the high temporal resolution, ECT has a low spatial resolution. ECT requires a sophisticated reconstruction technique to obtain the spatial distribution from individual capacitance measurements. Thirdly, ECT is not able to handle conducting material inside the bed, such as metals and water. The latter will pose restrictions to the experimental set-up, which will be discussed in detail in chap-

ter 3.

## 1.5 Organisation of the thesis

This thesis is organised as follows. In chapter 2 and 3 the applied numerical and experimental techniques is discussed, respectively. In chapter 4 and 5 simulation results are discussed, and in chapter 6 experimental results are discussed. The thesis is concluded with an epilogue in which experimental and simulation results are compared.

In chapter 2, the discrete particles model (DPM) and the two-fluid model (TFM) are introduced. Governing equations of both models are presented along with numerical implementations. Finally, the used computing hardware is discussed.

In chapter 3, the measuring principle of electrical capacitance tomography (ECT) is explained. This technique requires an advanced calibration technique which is explained in detail.

In chapter 4, DPM results are presented. For simulations at seven different operating pressures several properties are investigated, such as: porosity distributions, bubble sizes, pressure drop fluctuations and granular temperature.

In chapter 5, solids mixing in fluidized beds is discussed. Results from DPM and TFM are both presented and compared. Different methods to calculate the mixing index are discussed and compared.

In chapter 6, experimental results are presented. Several analysis methods are discussed. Results for polymeric particles, as well as for glass particles are shown. Furthermore a measurement series with a constant excess velocity is compared to results at three times the minimum fluidization velocity.

In chapter 7, porosity distributions and dynamic behaviour of experimental results are compared to simulation results. Finally, some overall conclusions are drawn.

# 2

## Numerical methods

### 2.1 Introduction

In this chapter the numerical models used in this thesis for the description of pressurized fluidized beds will be presented. These models comprise computational fluid dynamics (CFD) models, which are very powerful tools in addition to available experimental fluid dynamics (EFD) tools. With CFD data can be obtained with relative ease in circumstances that are otherwise pose severe experimental difficulties. Furthermore, in CFD many fluid parcels or particles can be tracked, which is virtually impossible in EFD. In addition, it is rather simple to vary physical conditions in CFD or simulate even unphysical conditions. For example, extremely high pressures can be modeled by changing a single figure, whereas experiments at elevated pressures require special equipment. CFD has some drawbacks: thorough validation of CFD tools is time consuming. Furthermore, simulating large systems requires a lot of computational time and can only be done if careful modelling assumptions are made. These assumptions concern for example the choice of the solids phase boundary conditions near walls (i.e. free slip or no slip) and the description of particles (i.e perfectly spherical particles). Even with modern computers it is impossible to account for all microscopic phenomena such as fluid flow around particles for systems with the size of industrial reactors.



Industrial reactors for PE and PP have dimensions in the order of  $10 \times 20$  meters. It remains impossible for the near future to simulate those systems with a discrete particles model in which each individual particle is tracked. Simulating one hour of operational time for an industrial reactor would take 100 million years with currently available computer hardware. Even if we would start the simulation today and replace our computer every year, assuming Moore's Law for increased computational time applies the next decades, it would still take a approximately 50 years to simulate one hour of real time for an industrial reactor. Not mentioning the memory usages needed to store data of a trillion ( $10^{12}$ ) particles. Since it will remain impossible to model industrial scale reactors with detailed models for the next decades, a multi-scale modelling approach as proposed by Van der Hoef et al. [2008] is required.

The multi-scale modelling approach comprises of different models of different levels of detail to describe relevant phenomena at different scales. For fluidized beds the multi-scale approach consists of a lattice Boltzmann model (LBM), a discrete particle model (DPM), a two-fluid model (TFM) and a discrete bubble model (DBM). As shown in Table 2.1 each of these models consider different scales. With the LBM detailed flow around particles can be solved without making any assumptions on the gas-particle interaction. With this type of simulations the particles are much larger then the computational grid size, so all flow details around the particles are captured. From LBM simulation data drag closures are obtained, see for example Beetstra et al. [2006], Van der Hoef et al. [2005] and Yin and Sundaresan [2009a,b]. In the DPM the particles are tracked individually, and the flow of the continuous (gas) phase is described by the Navier-Stokes equations. In the DPM the computational cells are much larger than the particles. Therefore, a closure for the drag is needed. In the TFM the particle and fluid phase are described as continuous interpenetrating fluids. In this description closures for interfacial drag, particle pressure and granular temperature are needed. But even with the TFM industrial scale simulations will take too long. Therefore the DBM was developed by Bokkers et al. [2006]. This model considers voids or bubbles as discrete elements, while the particulate phase is described as a continuous fluid. This model needs closures for bubble behaviour, such as: initial bubble size, bubble velocity, break-up and coalescence.

Table 2.1: Multi scale modeling for gas solids systems. Sets of equations used for particles and fluids are shown.

<b>Model</b>	<b>Scale</b>	<b>Particles</b>	<b>Particles</b>	<b>Fluid</b>
LBM	0.01 m	$10^3$	Static	Lattice Boltzmann
DPM	0.1 m	$10^6$	Newton's Law	Navier Stokes
TFM	1 m	$10^9$	Navier Stokes (KTGF)	Navier Stokes
DBM	10 m	$10^{12}$	Navier Stokes	Newton's Law

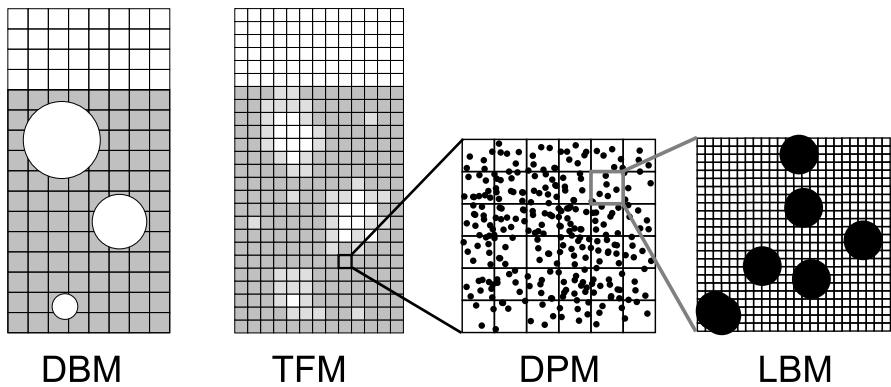


Figure 2.1: Multi scale modelling for gas solid systems. Schematic representation of discrete bubble model(DBM), two-fluid model (TFM), discrete Particle Model (DPM) and Lattice Boltzmann Model (LBM). From left to right models have increased level of detail, require less closures and need more computational time. (Based on Van der Hoef et al. [2008])

In this work we used the discrete particle model (DPM) and the two-fluid model (TFM). We chose the DPM since it takes particle interaction into account in a detailed manner. Particle interaction plays a key role in the effect of operation pressure on the fluidization behaviour. To study the fluidized bed behaviour in lab-scale systems we will use the TFM. Both models will be discussed in detail in this chapter.

## 2.2 Discrete particle model

The discrete particle model (DPM) is an Euler-Lagrange model, which was originally developed by Hoomans et al. [1996]. In the DPM particles are individually tracked accounting for particle-particle and particle-wall collisions. In this section the underlying equations and computational methods of the DPM are discussed.

### 2.2.1 Governing equations

#### Gas phase

In the DPM the gas phase hydrodynamics is described by the Navier-Stokes equations:

$$\frac{\partial}{\partial t} (\epsilon_f \rho_f) + \nabla \cdot (\epsilon_f \rho_f \bar{u}_f) = 0 \quad (2.1)$$

$$\frac{\partial}{\partial t} (\epsilon_f \rho_f \bar{u}_f) + \nabla \cdot (\epsilon_f \rho_f \bar{u}_f \bar{u}_f) = -\epsilon_f \nabla p - \nabla \cdot (\epsilon_f \bar{\tau}_f) - \bar{S}_p + \epsilon_f \rho_f \bar{g} \quad (2.2)$$

where  $\bar{u}_f$  is the gas velocity and  $\bar{\tau}_f$  represents the gas phase stress tensor. The sink term  $\bar{S}_p$ , represents the drag force per unit of volume exerted on the particles:

$$\bar{S}_p = \frac{1}{V_{cell}} \sum_{i=0}^{N_{part}} \frac{V_i \beta}{1 - \epsilon_f} (\bar{u}_f - \bar{v}_i) \int_{V_{cell}} D(\bar{r} - \bar{r}_i) dV \quad (2.3)$$

The distribution function  $D(\bar{r} - \bar{r}_i)$  is a discrete representation of a Dirac delta function that distributes the reaction force acting on the gas phase to the Eulerian grid via a volume-weighting technique, which will be explained in detail in section 2.2.3.

## Particles

The motion of every individual particle  $i$  in the system is calculated from Newton's second law:

$$m_i \frac{d\bar{v}_i}{dt} = -V_i \nabla p + \frac{V_i \beta}{\epsilon_s} (\bar{u} - \bar{v}_i) + m_i \bar{g} + \bar{F}_i^{pp} + \bar{F}_i^{pw} \quad (2.4)$$

where the forces on the right hand side are, respectively due to pressure, drag, gravity, particle-particle interaction and particle-wall interaction.

For the rotational motion of the particles the following equations is used.

$$\bar{I}_i \frac{d\bar{\omega}_i}{dt} = \bar{T}_i \quad (2.5)$$

where the moment of inertia is defined as:

$$I_i = \frac{2}{5} m r_i^2 \quad (2.6)$$

Drag forces ( $\beta$ ) and contact forces ( $\bar{F}_i^{pp} + \bar{F}_i^{pw}$ ) are described in the following sections.

## Drag models

The inter-phase momentum transfer coefficient,  $\beta$  describes the drag of the gas-phase acting on the particles. The Ergun [1952] and Wen and Yu [1966] equations are commonly used to obtain expressions for  $\beta$ . However, we use the closure relation derived by Koch and Hill [2001] based on lattice Boltzmann simulations, since it has no discontinuities at high Reynolds numbers and gives good results as reported by Bokkers et al. [2004] and Link et al. [2005].

$$\beta_{Koch\&Hill} = \frac{18\mu_f \epsilon_f^2 \epsilon_p}{d_p^2} (F_0(\epsilon_p) + \frac{1}{2} F_3(\epsilon_p) Re_p) \quad \text{if } Re_p > 40 \quad (2.7)$$

where:

$$Re_p = \frac{\epsilon_f \rho_f |\bar{u}_f - \bar{v}_p| d_p}{\mu_f} \quad (2.8)$$

$$F_0(\epsilon_p) = \begin{cases} \frac{1+3\sqrt{\frac{\epsilon_p}{2}} + \frac{135}{64}\epsilon_p \ln(\epsilon_p) + 16.14\epsilon_p}{1+0.681\epsilon_p - 8.48\epsilon_p^2 + 8.16\epsilon_p^3} & \text{if } \epsilon_p < 0.4 \\ \frac{10\epsilon_p}{\epsilon_f^3} & \text{if } \epsilon_p \geq 0.4 \end{cases} \quad (2.9)$$

$$F_3(\epsilon_p) = 0.0673 + 0.212\epsilon_p + \frac{0.0232}{\epsilon_f^5} \quad (2.10)$$

## Contact model

The contact forces are caused by collisions with other particles ( $\bar{F}_i^{pp}$ ) or confining walls ( $\bar{F}_i^{pw}$ ). Two contact models are available to calculate contact forces: a hard-sphere model and soft-sphere model. The hard-sphere model takes an event-driven approach, which treats the particle interaction as a consecutive series of instantaneous binary collisions. The soft sphere approach on the other hand, treats the particle interaction in a time step driven manner, allowing for multiple, enduring contacts. At low gas velocities and for low restitution coefficients (for example polymeric particles) the hard-sphere approach is not suitable. Therefore, in this work the soft-sphere approach is used.

In the soft-sphere approach the trajectories are determined by integrating the Newtonian equations of motion. The soft-sphere method originally developed by Cundall and Strack [1979] was the first granular dynamics simulation technique published in the open literature. Soft-sphere models use a fixed time step and consequently the particles are allowed to overlap slightly. The contact forces are subsequently calculated from the deformation history of the contact using a contact force scheme. The soft-sphere models allow for multiple particle overlap although the net contact force is obtained from the addition of all pair-wise interactions. The soft-sphere models are essentially time step driven, where the time step should be selected carefully for proper calculation of the contact forces.

In the soft-sphere model, the normal ( $\bar{n}_{ab}$ ) and tangential unit vectors ( $\bar{t}_{ab}$ ) are respectively defined as:

$$\bar{n}_{ab} = \frac{\bar{r}_a - \bar{r}_b}{|\bar{r}_b - \bar{r}_a|} \quad \text{and} \quad \bar{t}_{ab} = \frac{\bar{v}_{ab,0} - \bar{n}_{ab} \cdot \bar{v}_{ab,0}}{|\bar{v}_{ab,0} - \bar{n}_{ab} \cdot \bar{v}_{ab,0}|} \quad (2.11)$$

Three collision parameters are needed, which are defined as follows. The normal restitution coefficient  $e_n$ :

$$\bar{v}_{ab} \cdot \bar{n}_{ab} = -e_n(\bar{v}_{ab,0} \cdot \bar{n}_{ab}) \quad (2.12)$$

The tangential restitution coefficient  $e_t$

$$\bar{n}_{ab} \times \bar{v}_{ab} = -e_t(\bar{n}_{ab,0} \times \bar{v}_{ab}) \quad (2.13)$$

The friction coefficient  $\mu$ :

$$|\bar{n}_{ab} \times \bar{J}| = \mu |\bar{n}_{ab} \cdot \bar{J}| \quad (2.14)$$

and the reduced mass  $m_{ab}$ :

$$m_{ab} = \left( \frac{1}{m_a} + \frac{1}{m_b} \right)^{-1} \quad (2.15)$$

where the impulse vector  $\bar{J}$  corresponds with  $m_a(\bar{v}_a - \bar{v}_{a,b})$ . The contact force on particle  $a$  is calculated as the sum of the contact forces of all particles in the contact list of particle  $a$ , i.e. all particles  $b$ , including walls, which are in contact with particle  $a$ :

$$\bar{F}_i^{pp} + \bar{F}_i^{pw} = \sum_{\forall b \in \text{contactlist}} (\bar{F}_{ab,n} + \bar{F}_{ab,t}), \quad (2.16)$$

where  $\bar{F}_{ab,n}$  and  $\bar{F}_{ab,t}$  represent, respectively, the normal and tangential component of the contact force between particle  $a$  and  $b$ .

The torque only depends on the tangential contact force and is defined as follows:

$$\bar{T}_a = \sum_{\forall b \in \text{contactlist}} (R_a \bar{n}_{ab} \times \bar{F}_{ab,t}), \quad (2.17)$$

The calculation of the contact force between two particles is actually quite involved. The simplest one is originally proposed by Cundall and Strack [1979], where a linear-spring and dashpot model is employed to calculate the contact forces. In the latter model, the normal component of the contact force between two particles  $a$  and  $b$  can be calculated with:

$$\bar{F}_{ab,n} = -k_n \delta_n \bar{n}_{ab} - \eta_n \bar{v}_{ab,n}, \quad (2.18)$$

where  $k_n$  is the normal spring stiffness,  $\bar{n}_{ab}$  the normal unit vector,  $\eta_n$  the normal damping coefficient, and  $\bar{v}_{ab,n}$  the normal relative velocity. The overlap  $\delta_n$  is given by:

$$\delta_n = R_a + R_b - |\bar{r}_b - \bar{r}_a|. \quad (2.19)$$

Using equation 2.11 for the relative velocity between particle  $a$  and  $b$ , the normal relative velocity is obtained as follows:

$$\bar{v}_{ab,n} = (\bar{v}_{ab} \cdot \bar{n}_{ab})\bar{n}_{ab}. \quad (2.20)$$

The normal damping coefficient is given by:

$$\eta_n = \frac{-2 \ln e_n \sqrt{m_{ab} k_n}}{\sqrt{\pi^2 + \ln^2 e_n}} \quad (2.21)$$

where in case of particle-wall collisions the mass of collision partner  $b$  (i.e. the wall) is set infinitely large, resulting in  $m_{ab} = m_a$ . For the tangential component of the contact force a Coulomb-type friction law is used:

$$\bar{F}_{ab,t} = \begin{cases} -k_t \delta_t - \eta_t \bar{v}_{ab,t} & \text{if } |\bar{F}_{ab,t}| \leq \mu |\bar{F}_{ab,n}| \\ -\mu |\bar{F}_{ab,n}| \bar{t}_{ab} & \text{if } |\bar{F}_{ab,t}| > \mu |\bar{F}_{ab,n}| \end{cases} \quad (2.22)$$

where  $k_t$ ,  $\delta_t$ ,  $\eta_t$ , and  $\mu$  are the tangential spring stiffness, tangential displacement, tangential damping coefficient, and friction coefficient, respectively. The tangential relative velocity  $\bar{v}_{ab,t}$  is defined as:

$$\bar{v}_{ab,t} = \bar{v}_{ab} - \bar{v}_{ab,n}. \quad (2.23)$$

The tangential damping coefficient is defined as:

$$\eta_t = \frac{-2 \ln e_t \sqrt{\frac{2}{7} m_{ab} k_t}}{\sqrt{\pi^2 + \ln^2 e_t}} \quad (2.24)$$

The tangential displacement is given by:

$$\delta_t = \begin{cases} \delta_{t,0} \bar{H} + \int_{t_0}^t v_{ab,t} dt & \text{if } |\bar{F}_{ab,t}| \leq \mu |\bar{F}_{ab,n}| \\ \frac{\mu}{k_t} |\bar{F}_{ab,n}| \bar{t}_{ab} & \text{if } |\bar{F}_{ab,t}| > \mu |\bar{F}_{ab,n}| \end{cases} \quad (2.25)$$

with:

$$\bar{H} = \begin{bmatrix} qh_x^2 + c & qh_x h_y - sh_z & qh_x h_z + sh_y \\ qh_x h_y + sh_z & qh_y^2 + c & qh_y h_z + sh_x \\ qh_x h_x + sh_y & qh_y h_z + sh_x & qh_z^2 + c \end{bmatrix} \quad (2.26)$$

Table 2.2: Basic DPM algorithm

- Initialise variables
- for every  $dt_{flow}$ 
  - Calculate new flow properties
  - Map flow properties to particle positions
  - Calculate new particle properties
  - for every  $dt_{coll}$ 
    - \* Calculate new forces
    - \* Move particles
  - Map particle properties to flow positions

where  $\bar{h}$ ,  $c$ ,  $s$  and  $q$  are defined as:  $\bar{h} = \frac{\bar{n}_{ab} \times \bar{n}_{ab,0}}{|\bar{n}_{ab} \times \bar{n}_{ab,0}|}$ ,  $c = \cos \phi$ ,  $s = \sin \phi$ ,  $q = 1 - c$  and  $\phi = \arcsin(|\bar{n}_{ab} \times \bar{n}_{ab,0}|)$ .

For a more detailed discussion of this model we refer to Van der Hoef et al. [2006].

### 2.2.2 Numerical implementation

The main steps in the numerical implementation of the DPM are displayed in Table 2.2. After initialising the variables the main loop starts. In the main loop the transport equations of both phases are solved and coupling is accounted for. The overall time step ( $dt_{flow}$ ) is about  $10^{-4}s$ . To limit the particle-particle overlap to about 1% of the particle diameter it is required to use much smaller timesteps for the evaluation of the particle-particle contact, i.e.  $dt_{coll} = 10^{-6}s$ .

#### Gas phase equations

In the DPM the gas phase hydrodynamics are computed from the volume-averaged Navier-Stokes equations, employing a staggered grid to improve numerical stability. The equations are numerically solved following the SIMPLE algorithm. The convective fluxes in the conservation equations are calculated using the second order accurate Barton scheme [Centrella and Wilson, 1984, Goldschmidt et al., 2001] to reduce numerical diffusion and a standard central difference scheme is used for the diffusive terms.



### Particle equations

The motion of particles in the DPM are resolved in full 3D by integrating Newton's second law of motion, using a first order (Euler) time integration [Hoomans et al., 1996]:

$$\begin{aligned}
 \bar{v}^{n+1} &= \bar{v}^n + dt_{coll} \frac{\sum \bar{F}^n}{m_p} \\
 \bar{x}^{n+1} &= \bar{x}^n + dt_{coll} \cdot \bar{v}^{n+1} \\
 \bar{\omega}^{n+1} &= \bar{\omega}^n + dt_{coll} \frac{\sum \bar{T}^n}{I}
 \end{aligned}
 \tag{2.27}$$

### 2.2.3 Mapping

In this thesis the interfacial coupling between the gas phase and the particles is done using appropriate mapping windows, which is based on the work of Link et al. [2005] and Link [2006]. Contrary to other mapping methods where only the cell in which the particle is located is taken into account, the current mapping methods map over a cubic volume with an edge of 5 particle diameters irrespective of the applied numerical grid. Link et al. [2005] distribute the influence of the particles over each cell within the cube homogeneously (Figure 2.2). In this work we decrease the influence of the particle linearly, so cells further away from the particles are less influenced by the coupling.

$$D(x - x_i) = \frac{n - |x - x_i|}{n^2}
 \tag{2.28}$$

$$D(\bar{r} - \bar{r}_i) = D(x - x_i)D(y - y_i)D(z - z_i)
 \tag{2.29}$$

where  $n$  is the semi-width of the window,  $x_i$  is the position of particle  $i$  and  $x$  is the position of a cell. More complex relations such as polynomial function proposed by Deen et al. [2004] can be used, but are computationally more expensive. As seen in Figure 2.2 the polynomial function of Deen et al. [2004] and the triangular description used in this work differ only slightly.

If particles are close to a wall, a part of the mapping window might fall outside the computational domain. To prevent this from happening, that part of the window is mirrored back into the domain as suggested by Link (see Figure 2.3).

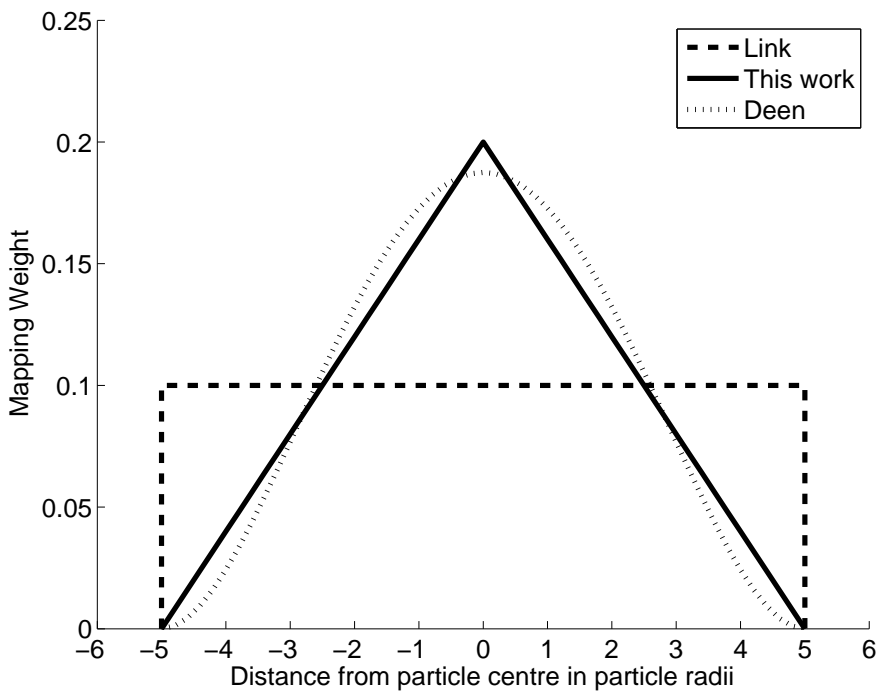


Figure 2.2: Mapping weight of Link [2006], this work and Deen et al. [2004] as function of position

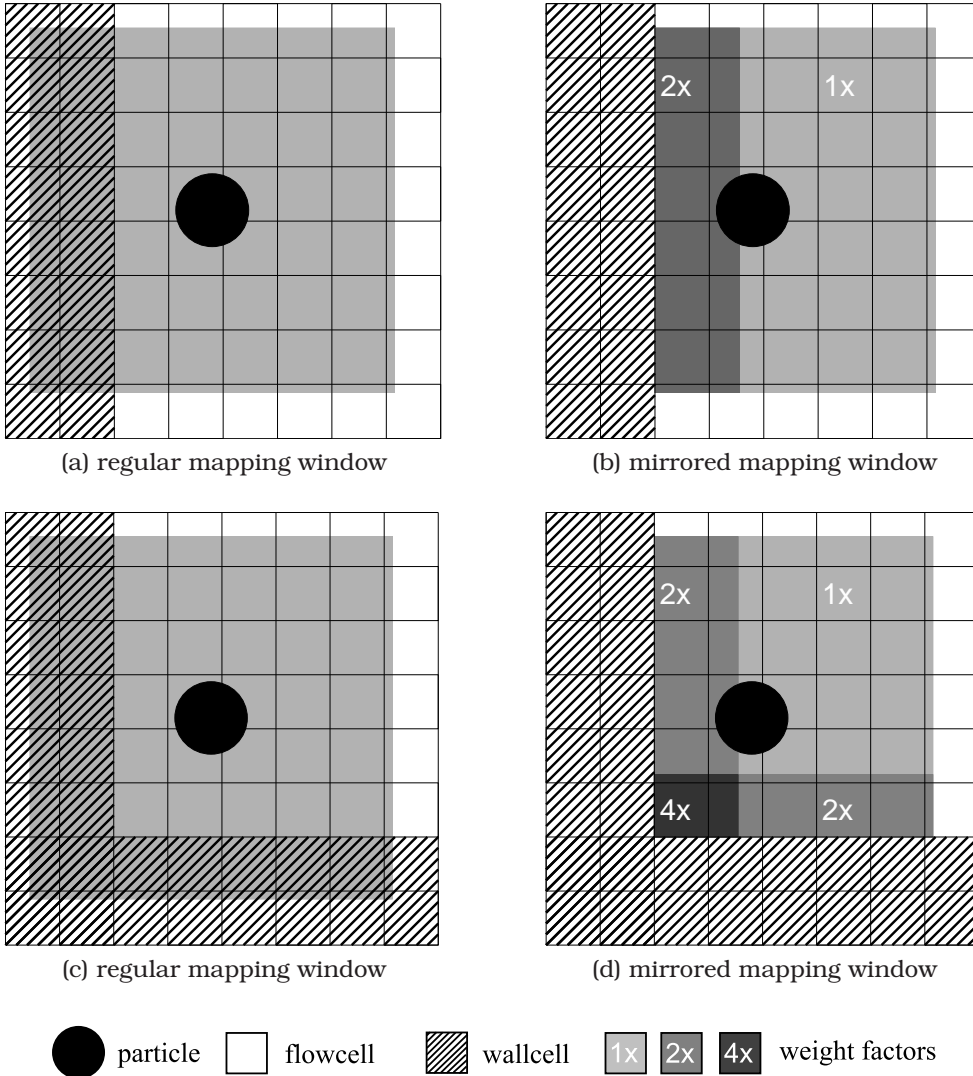


Figure 2.3: Illustration of mirroring of mapping windows around walls and in corners.

### 2.2.4 Initial and boundary conditions

A prescribed inflow boundary condition was chosen at the bottom and a prescribed pressure boundary was chosen at the top of the bed. At the confining walls the no-slip condition was applied. In case of pseudo 2D simulations the boundary conditions for the front wall and back wall were set to free-slip, thus mimicking a slice out of a larger 3D bed. Initially the particles are packed cubically, with very little space between the particles. If no additional measures would be taken the bed would initially expand enormously. It takes several seconds to exclude start-up effects. The associated computation would require several days of calculation time for large simulations. Therefore, the initial particle configuration was altered. Two half bubbles were initialised near both walls (see Figure 2.4). After start of the simulation the bed immediately starts to fluidize and within half a second no start-up effects are discernible. Other initial particle positions did not work, such as: horizontal layers without particles, vertical layers without particles and a more porous initial packing. For all simulations an aspect ratio of 2 is chosen, i.e. the packed bed height is twice the bed width. The domain is chosen twice the packed bed height for low pressures. At high pressures or for more vigorous fluidization higher columns were used.

In general the size of computational cells was set to be about 3 times the particle diameter. As a result bubbles are captured by typically 10 computational cells. Detailed flow around individual particles is not solved in the DPM. Since we use mapping windows of 5 times the particle diameter, smaller cells would not give more detailed information.

### 2.2.5 Parallel code

There are two main reasons one can make a CFD code parallel. In most cases the user would like to improve the calculation speed of a simulation, but in some cases it is necessary to improve memory efficiency. In the latter case, the memory of all nodes is used for one single simulation, but it is not optimized for calculation speed. Since DPM simulations are time consuming, the DPM is made parallel in order to reduce the computational time.

As a rule of thumb one can say that solving the equations of motion for a computational flow cell and for a single particle consume the

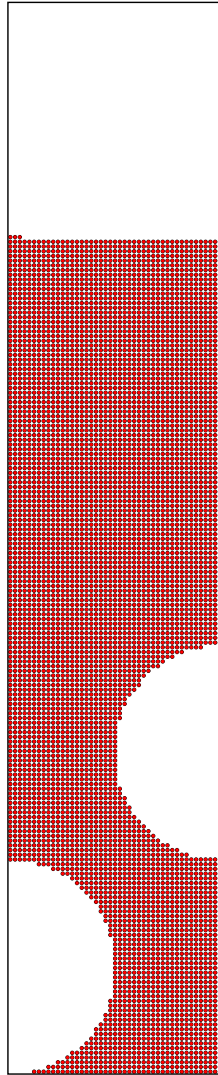


Figure 2.4: Initial configuration of particles in the DPM with two half bubbles.

same CPU time. In the case of DPM simulations the number of particles is much larger than the number of computational cells. Therefore, parallelizing the particle calculations is essential to increase the speed of the simulations.

The computational load of the particles can be distributed over the nodes in several ways. Domain decomposition is commonly used for Navier-Stokes and other flow solvers. This method divides the domain into subdomains, and each node takes care of the fluid or particles in one of the subdomains. Communication between the nodes is necessary to exchange information at the boundaries between neighbouring subdomains. For particles this method becomes rather complicated. Particles influence each other within a region known as the neighbour area. The size of this area is chosen such that all neighbouring particles that are within reach during one computational time step are contained in it. The radius of this area is known as the neighbour radius. Each node treats the particles within its own subdomain plus a zone around it with the size of the neighbour radius. An additional problem is that particles will move through the bed and continuously move from one subdomain to another. Since domain decomposition is not efficient for small systems, another more efficient parallelization method, i.e. particle number decomposition is used in this work. In particle number decomposition all particles are distributed over the nodes and will not change node over time. Particles from all nodes are fully mixed and therefore particles assigned to certain nodes are always in the vicinity of particles assigned to other nodes. Therefore all information of all particles must be known on all nodes.

Particles are distributed over the nodes according to the round robin method as used by Darmana et al. [2006]. Since collisions are calculated by the processor taking care of the lower numbered particle, partitioning based on memory location would only result in poor parallel performance as the the processor with a higher index will calculate particles with a higher index with less associated possible particle neighbours, while processors with a lower index will calculate particles with a lower index with more particles associated neighbours. The round robin method assigns single particles subsequently from the first node to the last node and again until all particles are assigned to a node according to equation 2.30.

$$P = i \bmod n \quad (2.30)$$

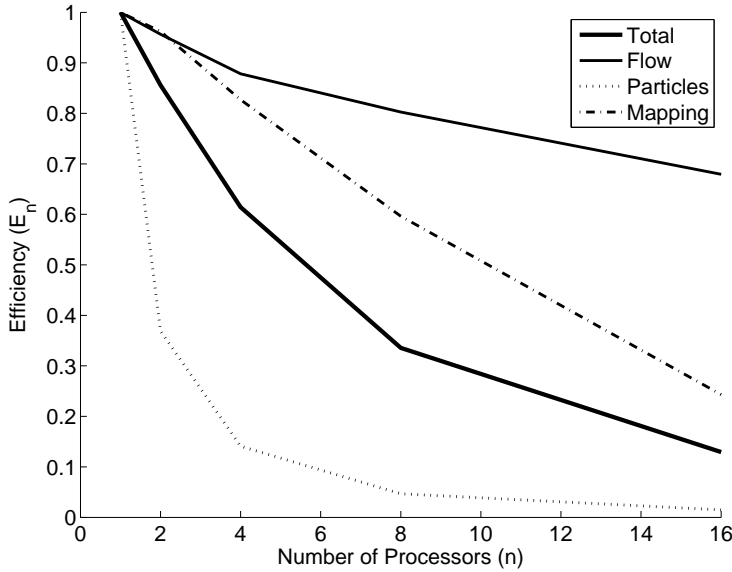


Figure 2.5: Efficiency of the parallelization for different number of processors for developed fluidized bed in a DPM simulation.

where  $P$  is the index of the node,  $i$  is the index of the particle and  $n$  is the number of nodes.

Similar to Darmana et al. [2006] we characterize the performance of the parallelization by the speed-up and the efficiency respectively defined by:

$$S_n = \frac{T_s}{T_n} \quad (2.31)$$

$$E_n = \frac{T_s}{nT_n} \quad (2.32)$$

where  $T_s$  is the computational time for a single processor simulation,  $T_n$  is the computational time of the parallelized code using  $n$  processors. The speed-up and efficiency for different parts of the code are shown in Figure 2.5 and 2.6. The major fraction of calculation time used in the flow solver concerns matrix operations. These can be parallelized very efficiently as illustrated in Figure 2.5 and 2.6. Particles and collisions are much harder to parallelize due to the considerable data communication that is required. As a result the simulations on 8 processors are hardly any faster compared to simulations on 4 pro-

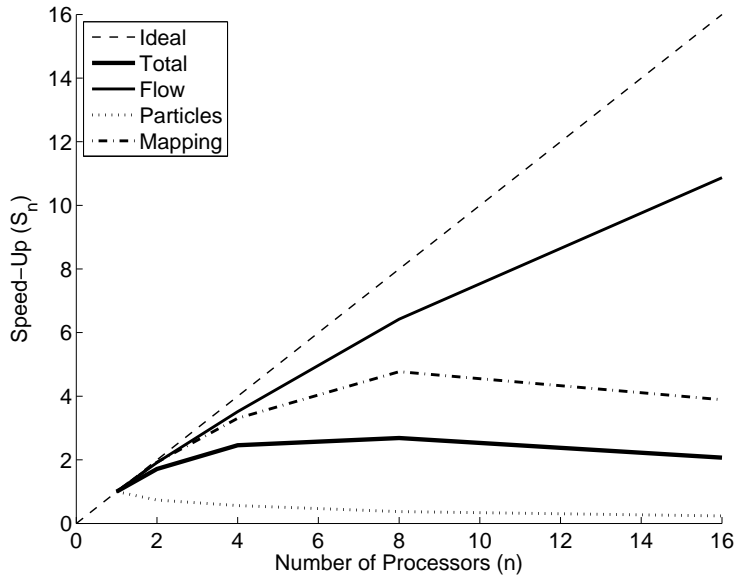


Figure 2.6: Speedup for the same simulation as in Figure 2.5.

processors. Mapping used for the two-way coupling can be parallelized quite efficiently, but still requires communication, for example for the calculation of the local porosity. Further improvement of the parallelization of the code, especially of the particles, is needed to improve the efficiency.

## 2.3 Two-fluid model

In the two-fluid model (TFM) both the gas phase and the particulate phase are modeled as continua. Contrary to the DPM individual particles are not tracked. Both phases are treated as interpenetrating fluids. With the TFM, much larger systems can be simulated compared to the DPM.

### 2.3.1 Governing equations

Similar to the DPM the Navier-Stokes equations are solved for the gas phase:



$$\frac{\partial}{\partial t}(\epsilon_f \rho_f) + \nabla \cdot (\epsilon_f \rho_f \bar{u}_f) = 0 \quad (2.33)$$

$$\begin{aligned} \frac{\partial}{\partial t}(\epsilon_f \rho_f \bar{u}_f) + \nabla \cdot (\epsilon_f \rho_f \bar{u}_f \bar{u}_f) = \\ -\epsilon_f \nabla p_f - \nabla \cdot (\epsilon_f \bar{\tau}_f) - \beta(\bar{u}_f - \bar{u}_s) + \epsilon_f \rho_f \bar{g} \end{aligned} \quad (2.34)$$

As an equation of state the ideal gas law is used:

$$\rho_f = \frac{M_f}{RT_f} p_f \quad (2.35)$$

Since the particulate phase is also considered as a fluid similar equations apply:

$$\frac{\partial}{\partial t}(\epsilon_s \rho_s) + \nabla \cdot (\epsilon_s \rho_s \bar{u}_s) = 0 \quad (2.36)$$

$$\begin{aligned} \frac{\partial}{\partial t}(\epsilon_s \rho_s \bar{u}_s) + \nabla \cdot (\epsilon_s \rho_s \bar{u}_s \bar{u}_s) = \\ -\epsilon_s \nabla p_f - \nabla p_s - \nabla \cdot (\epsilon_s \bar{\tau}_s) + \beta(\bar{u}_f - \bar{u}_s) + \epsilon_s \rho_s \bar{g} \end{aligned} \quad (2.37)$$

where  $\beta$  is the inter phase momentum transfer coefficient. For DPM and TFM we use the same drag relation according to Koch and Hill [2001] as described in equation 2.7. To describe the particle-particle interaction, the kinetic theory of granular flow (KTGF) is used. This theory was initially developed by Gidaspow [1994]. In addition to the continuum equation and the Navier-Stokes equations a partial differential equation for the granular temperature is solved. The overall granular temperature is defined as  $\frac{1}{3}$  of the mean of the velocity fluctuation component squared:

$$\Theta = \frac{1}{3} \langle \bar{C}_p \cdot \bar{C}_p \rangle \quad (2.38)$$

where:

$$\bar{c}_p = \bar{u}_s + \bar{C}_p \quad (2.39)$$

The particle velocity ( $\bar{c}_p$ ) is decomposed in the local mean velocity ( $\bar{u}_s$ ) and the fluctuation velocity component ( $\bar{C}_p$ ). The granular temperature equation is given by:

$$\frac{3}{2} \left[ \frac{\partial}{\partial t} (\epsilon_s \rho_s \Theta + \epsilon_s \rho_s \Theta \bar{u}_s) \right] = \quad (2.40)$$

$$-(P_s \bar{I} + \epsilon_s \bar{T}_s) : \nabla \bar{u}_s - \nabla \cdot (\epsilon_s q_s) - 3\beta\Theta - \gamma$$

The consecutive equations were derived by Nieuwland et al. [1996] and are presented in Table 2.3.

For a detailed description of all the used KTGF equations we refer to the work of Goldschmidt et al. [2001].

### 2.3.2 Numerical implementation

In the TFM a similar solution strategy as in the DPM has been applied to solve the equations. The main difference is that in the TFM an extra step is implemented to solve the particle volume fraction taking the compressibility of the particulate phase into account. A brief description of the solution is given below. For more details the reader is referred to Goldschmidt et al. [2001].

In Table 2.4 the overall algorithm is shown. Computational cycles consist of the calculation of explicit terms and the calculation of implicit terms. If the defect convergence criterion is met, the next time step is computed.

In the TFM the hydrodynamics are computed from the volume-averaged Navier-Stokes equations, employing a staggered grid to improve numerical stability. The equations are numerically solved following the SIMPLE algorithm. The convective fluxes in the conservation equations are calculated using the second order accurate Barton scheme [Centrella and Wilson, 1984, Goldschmidt et al., 2001] to reduce numerical diffusion and a standard central difference scheme is used for the diffusive terms.

The Navier-Stokes equations for the gas phase are solved minimizing the defect in the mass balance by adjusting the pressure. For the particle phase the volume fraction ( $\epsilon_s$ ) is adjusted minimizing the defect in the solids phase mass balance. For both pressure and volume fraction corrections, (sparse) matrix equations are solved using the ICCG method. This method is called the *pressure -  $\epsilon_s$*  algorithm (i.e. pressure correction scheme).

Table 2.3: Two-fluid model, closure equations

---

Particle pressure:

$$p_s = [1 + 2(1 + e_n)\epsilon_s g_0]\epsilon_s \rho_s \theta$$

Newtonian stress-tensor:

$$\bar{\bar{\tau}}_s = -[(\lambda_s - \frac{2}{3}\mu_s)(\nabla \cdot \bar{u}_s)\bar{\bar{I}} + \mu_s((\nabla \bar{u}_s) + (\nabla \bar{u}_s)^T)]$$

Bulk viscosity:

$$\lambda_s = \frac{4}{3}\epsilon_s \rho_s d_p g_0 (1 + e_n) \sqrt{\frac{\theta}{\pi}}$$

Shear viscosity:

$$\mu_s = 1.01600 \frac{5}{96} \pi \rho_s d_p \sqrt{\frac{\theta}{\pi}} \frac{(1 + \frac{8}{5} \frac{(1+e_n)}{2} \epsilon_s g_0)(1 + \frac{8}{5} \epsilon_s g_0)}{\epsilon_s g_0} + \frac{4}{5} \epsilon_s \rho_s d_p g_0 (1 + e_n) \sqrt{\frac{\theta}{\pi}}$$

Pseudo-Fourier fluctuating kinetic energy flux:

$$\bar{q}_s = -\kappa_s \nabla \theta$$

Pseudo-thermal conductivity:

$$\kappa_s = 1.02513 \frac{75}{384} \pi \rho_s d_p \sqrt{\frac{\theta}{\pi}} \frac{(1 + \frac{12}{5} \frac{(1+e_n)}{2} \epsilon_s g_0)(1 + \frac{12}{5} \epsilon_s g_0)}{\epsilon_s g_0} + 2\epsilon_s \rho_s d_p g_0 (1 + e_n) \sqrt{\frac{\theta}{\pi}}$$

Dissipation of granular energy due to inelastic particle-particle collisions:

$$\gamma = 3(1 - e_n^2)\epsilon_s^2 \rho_s g_0 \theta [\frac{4}{d_p} \sqrt{\frac{\theta}{\pi}} - (\nabla \cdot \bar{u})_s]$$

Radial distribution function:

$$g_0 = \frac{1 + \epsilon_s (\epsilon_s (4.5904 + 4.515436 \epsilon_s))}{(\frac{1 - \epsilon_s^3}{\epsilon_s^3, max})^{0.678202}}$$


---

Table 2.4: TFM algorithm

```

Initialise variables
for every  $dt_{flow}$ 
    Calculation of explicit terms: diffusion, force, flux and velocities
    Computational cycles until defects are small
        Solve Navier-Stokes gas phase using a pressure correction
        Solve Navier-Stokes particle phase using a solids fraction correction
        Update phase fractions
    Solve granular temperature equation

```

### Initial and boundary conditions

A prescribed inflow boundary condition was chosen at the bottom and a prescribed pressure boundary was chosen at the top of the bed. At the confining walls the no-slip condition was applied. In case of pseudo 2D simulations the boundary conditions for the front wall and back wall were set to free-slip, thus mimicking a slice out of a larger 3D bed. All boundary conditions are similar to the DPM, except for the particle phase, for which the bottom and the top of the bed were described by a no-slip condition. Initially two half bubbles with no particle phase were set similar to the DPM to reduce start-up effects (Figure 2.4). The particle fraction ( $\epsilon_s$ ) is set to 0.6 according to a random packing. For all simulations an aspect ratio of 2 is chosen: the packed bed height is twice the bed width.

Computational flow grid size and particles diameter should be carefully chosen to prevent instability. In this work we use a 5 mm grid and 1 mm particle diameter. The maximum packing is set to 0.644 and the minimum granular temperature is  $10^{-12} \frac{m^2}{s^2}$ . The computational time step is set to  $5 \cdot 10^{-5} s$ , since larger time steps were found to cause instability.

## 2.4 Computing hardware

The simulations described in this thesis typically take up to one month of computational time. Therefore we use dedicated computer clusters. In the FCRE group we have two special designed computer clusters. The Citra (Cluster InfrasTructure for paRAllel research) con-

sists of twelve 19" AMD Opteron DP 270 2.0 GHz quad core nodes all interconnected with infiniband network interface. Citra is very suitable for parallel code. Processes with up to four threads are treated very efficiently. For processes with more than four threads the infiniband cards are used, which makes the processes slightly less efficient. The Donald cluster consists of 48 standard dual-core PC's ranging from 2.6 to 3.0 GHz personal computers. This cluster is suitable for serial jobs or double threaded codes. We also did simulations on the ASTER cluster at SARA in Amsterdam. The ASTER cluster is a SGI Altix 3700 system, consisting of 416 CPU's (Intel Itanium 2, 1.3 GHz, 3 MByte cache each).

# 3

## Electrical capacitance tomography

### 3.1 Introduction

Many multiphase flow systems are not optically accessible. For experimental investigation of these systems optical techniques can only be used in a few special cases. More often however one needs to resort to non-optical techniques, in which 2D slices are obtained of phase fraction distribution in a multiphase system.

Most tomography techniques originate from the medical field such as Computer Aided Tomography (CAT-scan also known as X-ray tomography), Positron emission tomography (PET) and Magnetic resonance imaging (MRI). All of these techniques are based on a specific material property. CAT is based on the permeability of X-rays through a human body: bones permeate poorly, while flesh permeates better. For PET scans, a weak radioactive material emitting positrons is introduced in the body and can be traced using the PET-scanner. MRI is based on the magnetic spin of hydrogen atoms, which is used for measuring water content. Other tomography techniques that do not originate from the medical field are: Ocean acoustic tomography (Sonar) from marine research and electrical capacitance tomography (ECT) and electrical resistance tomography (ERT), which were designed for industrial purposes. Sonar is based on reflections of sound waves, ECT is based on varying electrical permittivity and ERT is based on

varying resistance.

In this work we use ECT because it is a relatively cheap technique as it requires a simple static sensor made out of standard circuit board and a dedicated data acquisition module (DAM). Furthermore, ECT is a safe technique where no radiation is present or dedicated technicians are required unlike CAT and MRI. ECT is a fast technique that is able to measure up to 300Hz for 6 electrodes and up to 100Hz for 12 electrodes. There are three main drawbacks of ECT: contrary to the high temporal resolution, ECT has a low spatial resolution. As a rule of thumb the resolution is about one tenth of the diameter and one twelfth of the circumference for a twelve electrode sensor. ECT requires a sophisticated reconstruction technique to obtain the spatial distribution from individual capacitance measurements. Reconstruction techniques are discussed in detail in section 3.4. Thirdly, ECT is not able to handle conducting material, such as metals and water.

ECT was originally developed at the UMIST in Manchester by Huang et al. [1988]. They were the first to use capacitance measurements of an array of electrodes to obtain an image. In general, ECT can be used to monitor any process where the fluid to be observed has low electrical conductivity and a varying permittivity. Nowadays, the technique is commercially available at a few suppliers, but still mostly for research purposes. Although ECT initially was used for gas-oil levels in pipelines, later ECT was applied for gas-solid systems, for example by Dyakowski et al. [1997]. A lot is known on the reconstruction techniques, i.e. many new algorithms and improved versions of known algorithms were reported by among others Isaksen [1996], Y. and Yang [2008] and Yang and Peng [2003]. Advanced developments in ECT measuring techniques were reported by Reinecke and Mewes [1996], who propose to temporally group electrodes into new virtual electrodes to increase the number of independent measurements. Three dimensional ECT was developed by Warsito and Fan [2003], who measured inter electrode capacitances between electrodes from different planes. This leads to real 3D images, instead of multiple stacked 2D plane images. Though the latter technique is promising, it should be mentioned that the resolution of 3D-ECT is still poor. ECT can be used in industry since it can provide not only porosity and bubble information, but also fluctuations in porosity. Makkawi and Wright [2002a,b, 2004] developed simple statistical methods to characterize fluidization regimes and bed behaviour from

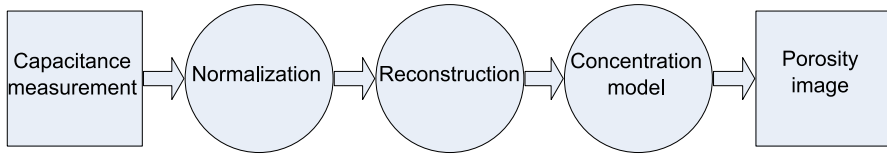


Figure 3.1: Steps from 66 capacitance measurements to a  $32 \times 32$  pixel porosity image.

ECT measurements of fluidized beds.

In this work we present ECT for the measurement of porosity distributions, bubble sizes and bubble velocities at different operating pressures. In chapter 6 the analysis tools and results will be discussed. In this chapter the measuring technique ECT is discussed. First the basic principle of measuring capacitances and the electrode design is discussed. Furthermore all three steps from measurement to image are discussed: calibration and normalization, reconstruction and the use of concentration models are discussed (see Figure 3.1). Finally the chosen methods are summarized in terms of an overall conclusion.

## 3.2 Basic principle

ECT is used to obtain information about the spatial distribution of a mixture of dielectric materials inside a vessel, by measuring the electrical capacitances between sets of electrodes placed around its periphery and converting these measurements into an image showing the distribution of permittivity as a pixel-based plot or image. The images produced by ECT systems are approximate and of relatively low resolution, but they can be generated at relatively high speeds. Although it is possible to image vessels of any cross section, most of the work to-date has been carried out on circular vessels up to 0.3 meter diameter.

ECT can be used with any arbitrary mixture of different non-conducting dielectric materials such as polymers, hydrocarbons, sand or glass. However, an important application of ECT is viewing and measuring the spatial distribution of a mixture of two different dielectric materials (a two-phase mixture), as in this case, the concentration distribution of the two components over the cross section



Table 3.1: Relative electric constants for varying materials. (source: Verkerk et al. [1986])

<b>material</b>	$\epsilon_r$	<b>comment</b>
Vacuum	1	(by definition)
Air (1 bar)	1.00056	
Water (vapor)	1.00060	
Air (20 bar)	1.0112	$20(\epsilon_{r,air,1bar} - 1) + 1$
Polypropylene	2.25	
Polyethylene	2.25	
Polystyrene	2.55	
Mineral oil	2.5	
PVC	4.5	
Glass	6.0	
Distilled water (liquid)	80	

of the vessel can be obtained from the the permittivity distribution.

The achievable permittivity image resolution depends on the number of independent capacitance measurements, but is generally low. However, images can be generated at high frame rates, typically at 100 Hz. A typical ECT permittivity image format uses a square grid of  $32 \times 32$  pixels to display the distribution of the normalised composite permittivity of each pixel. For a circular sensor, 812 of the available 1024 pixels are used to approximate the circular cross-section of the sensor. The values of each pixel represent the normalised value of the effective permittivity of that pixel. In the case of a mixture of two dielectric materials, these permittivity values are related to the fraction of the higher permittivity material present (the volume ratio) at that pixel location.

In this work we will be referring to the relative permittivity  $\epsilon_r$  (or dielectric constant) of materials. The relative permittivity of a material is its absolute permittivity ( $\epsilon$ ) divided by the permittivity of vacuum ( $\epsilon_0 = 8.85 \cdot 10^{-12} F/m$ ):

$$\epsilon_r = \frac{\epsilon}{\epsilon_0} \quad (3.1)$$

Hence, the relative permittivity of air is about 1 and typical values for other solids and liquids are polystyrene (2.5), glass (6.0) and mineral oil (2.3) (see Table 3.1).

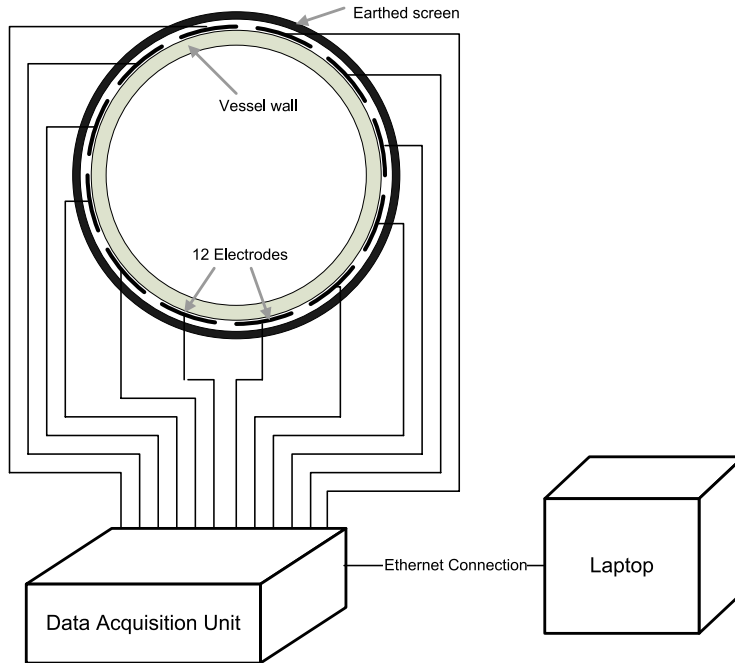


Figure 3.2: Basic ECT System.

### 3.2.1 ECT system configuration

An ECT system consists of a capacitance sensor, measurement circuitry and a control computer. Screened cables connect the sensor to the measurement circuitry, which must be able to measure very small inter-electrode capacitances, of the order of  $10^{-15}\text{F}$  (1 fF), in the presence of much larger capacitances to earth of the order of  $2 \cdot 10^5$  fF. A schematic illustration of a basic ECT system of this type is shown in Figure 3.2.

The number of sensor electrodes that can be used, depends on the range of values of inter-electrode capacitances and the upper and lower measurement limits of the capacitance measurement circuit. The capacitance values when the sensor contains air, are referred to as standing capacitances and their relative values are shown in Figure 3.3 for a 12-electrode circular sensor with internal electrodes.

Sequential electrodes are referred to as adjacent electrodes, and have the largest standing capacitances, while opposite electrodes have the smallest capacitances. As the number of electrodes in-

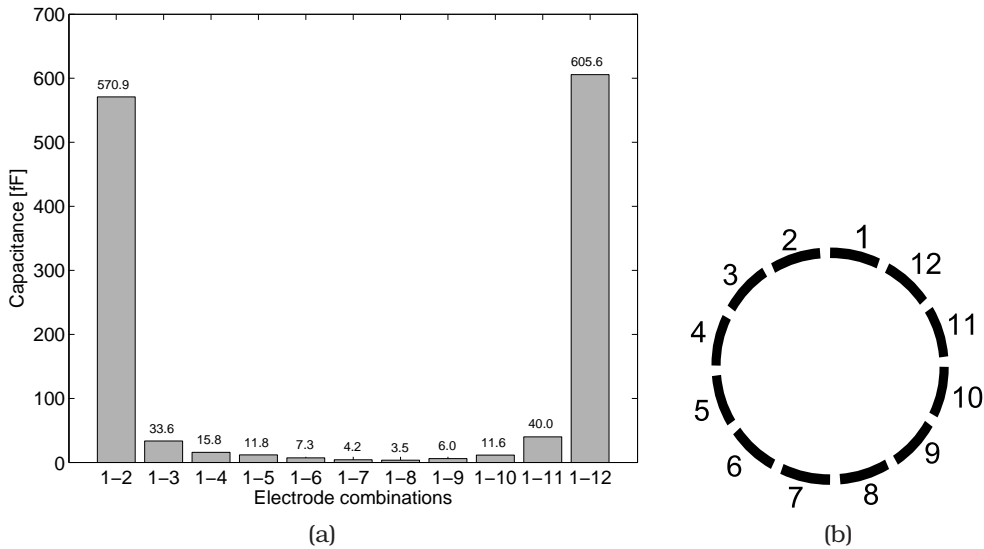


Figure 3.3: Inter-electrode capacitances (a) and electrode configuration (b).

creases, the electrode surface area per unit axial length decreases and the inter-electrode capacitances also decrease. When the smallest of these capacitances (for opposite electrodes), reaches the lowest value that can be measured reliably by the capacitance circuitry, the number of electrodes, and hence the image resolution, can only be increased further by increasing the axial lengths of the electrodes. However, these lengths cannot be increased indefinitely because the standing capacitances between pairs of adjacent electrodes will also increase and the measurement circuitry will saturate or overload once the highest capacitance measurement threshold is exceeded.

The measurement sequence involves applying an alternating voltage from a low-impedance supply to one (source) electrode. The remaining (detector) electrodes are all held at zero (virtual ground) potential and the currents which flow into these detector electrodes (and which are proportional to the inter-electrode capacitances) are measured. A second electrode is then selected as the source electrode and the sequence is repeated until all possible electrode pair capacitances have been measured. This generates  $M$  independent inter-electrode capacitance measurements, where:

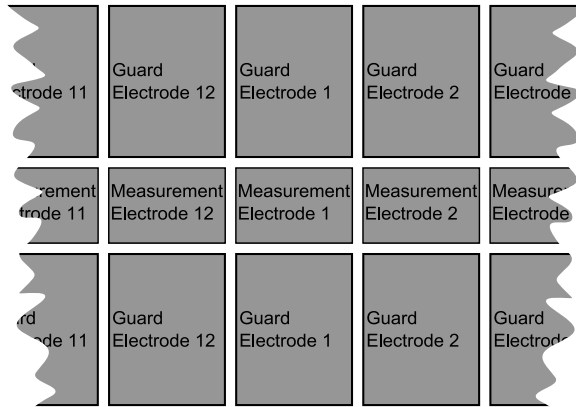


Figure 3.4: Part of an example printed circuit board (PCB) of the ECT electrodes with one plane of measurement electrodes and on both sides guard electrodes.

$$M = \frac{E(E-1)}{2} \quad (3.2)$$

and  $E$  is the number of electrodes located around the circumference. For example for  $E = 12$ ,  $M = 66$ . As the measurements for a single frame of data are made sequentially, the capacitance data within the frame will be collected at different times and there will be some time skewing of the data. Interpolation techniques can be used to de-skew this data if this effect is likely to produce significant errors. De-skewing is not used in this work.

Axial resolution and overall measurement sensitivity can be improved by the use of driven axial guard electrodes, located either side of the measurement electrodes, as shown in the flexible laminate design of Figure 3.4.

The driven axial guard electrodes are excited at the same electrical potentials as the associated measurement electrode and prevent the electric field from being diverted to earth at the ends of the measurement electrodes. For large diameter vessels, axial guard electrodes are normally an essential requirement to ensure that the capacitances between opposing electrodes are measurable.

With the current state of capacitance measurement technology, it is possible to measure capacitance changes between 2 unearthed

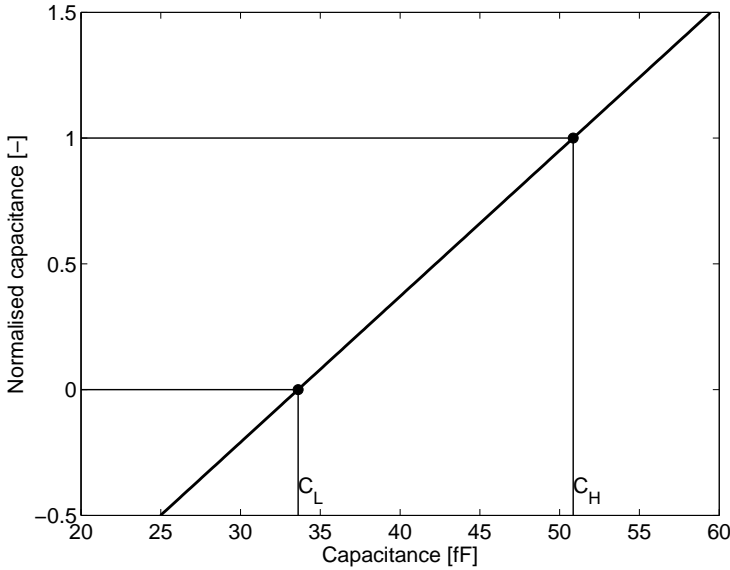


Figure 3.5: Normalization of electrode combination 1-3, where  $C_L$  is the capacitance for an empty bed and  $C_H$  is the capacitance for a bed filled with particles.

electrodes of 0.1 fF in the presence of stray capacitance to earth of 200 pF at a rate of 2000 measurements per second. This sets a practical lower design limit on the capacitance between any pair of electrodes of around 5 fF, which equates to measurement electrodes of minimum axial length of 5 cm for a 12 electrode sensor. These dimensions assume that effective driven axial guards are used.

### 3.3 Calibration

ECT capacitance measurements are normalised since large differences occur between capacitance values between neighbouring electrode pairs and opposite pair as seen in Figure 3.3.

Calibration of the ECT sensor is rather straightforward. The absolute capacitances are measured for an empty column and for a column filled with particles. The normalised capacitance can be easily calculated with equation 3.3:

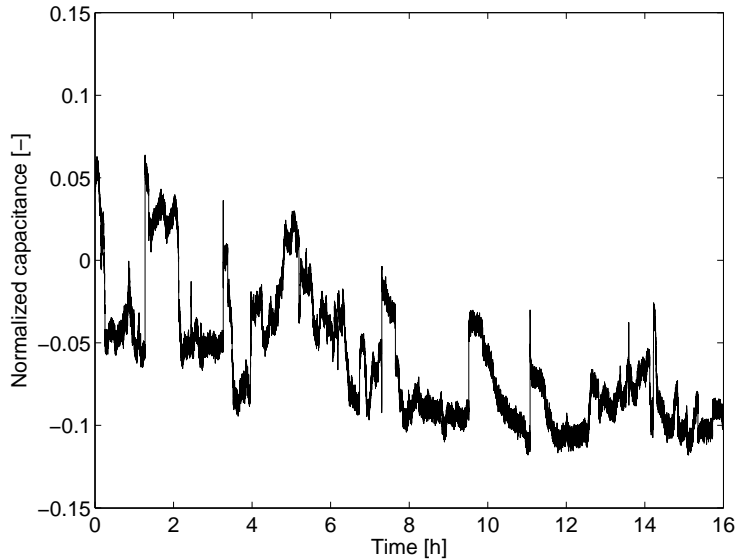


Figure 3.6: Plane averaged normalized capacitance for an empty column for a measurement overnight.

$$C_n = \frac{C - C_L}{C_H - C_L} \quad (3.3)$$

where  $C$  is the measured capacitance,  $C_L$  is the capacitance of an empty bed,  $C_H$  is the capacitance of a bed filled with particles and  $C_n$  is the normalised capacitance.

Unfortunately the straightforward approach of calibrating, measuring a full and empty vessel, is not suitable for the pressurized setup, which will be discussed in chapter 6. Three properties of the setup cause the necessity of an alternative calibration method: occurrence of signal jumps, signal drift and difficulty to open the vessel, each of which will be explained below.

Figure 3.6 shows normalized capacitance values for an empty column calibrated for LLDPE particles which were measured over night at 1 Hz. During this measurement, no experiments were performed and no work was done to the column. After calibration ideally, the electrodes should have measured a constant normalized capacitance of zero. However, the signal shows sudden jumps in the signal. After a few minutes the calibrations deteriorate. Moreover, the signals slowly drift away from the initial values. Sidorenko and Rhodes [2004] re-

ported signal drifts as well, but the cause for these drifts is not known. Tests show that the technique is sensitive to external influences such as: moved wires, presence of humans. Although these events did not occur overnight we assume that the drifts and jumps are due to external influences. Frequent calibration should overcome the calibration problems. Unfortunately it is not possible to open the vessel and remove the particles quickly. Opening the pressure vessel takes about 4 hours. Therefore, frequent calibration of the empty vessel is impossible. Frequently measuring a filled column is possible though.

It is anticipated that the absolute capacitance difference between the empty and full column is constant, since it only depends on material properties. Drifts and jumps are assumed to be caused by external factors, and have equal influence for filled and empty vessels. Hence, the denominator of equation 3.3 is assumed to be constant:

$$C_{H,1} - C_{L,1} = C_{H,0} - C_{L,0} \quad (3.4)$$

where subscript 0 corresponds with the initial calibration and subscript 1 corresponds with calibration after jumps and drift. Note that the lower calibration after drifts ( $C_{L,1}$ ) is not known, but can be obtained after simple rearranging:

$$C_{L,1} = C_{H,1} - (C_{H,0} - C_{L,0}) \quad (3.5)$$

Normalization equation 3.3 for the situation after drifts (subscript 1) is:

$$C_n = \frac{C - C_{L,1}}{C_{H,1} - C_{L,1}} \quad (3.6)$$

where the denominator can be replaced by  $C_{H,0} - C_{L,0}$  according to equation 3.4 and  $C_{L,1}$  in the nominator can be replaced by  $C_{H,1} - (C_{H,0} - C_{L,0})$  according to equation 3.5, slightly rearranged leading to:

$$C_n = \frac{C - C_{L,0} + (C_{H,1} - C_{H,0})}{C_{H,0} - C_{L,0}} \quad (3.7)$$

Only known terms are used in equation 3.7. Compared with equation 3.3 only the drift ( $C_{H,1} - C_{H,0}$ ) is added.

## 3.4 Reconstruction

From 66 independent normalized capacitance measurements a  $32 \times 32$  pixel image needs to be reconstructed. In this section four different reconstruction methods are discussed: Linear Back Projection (LBP), Iterative LBP, Tikhonov reconstruction and Landweber reconstruction. Each of these methods require a sensitivity matrix which is discussed first.

### Sensitivity matrix

The sensitivity matrix describes how the measured capacitance between any combination of electrodes changes when a change is made to the dielectric constant of a single pixel inside the sensor. This can be better understood by considering the case where one electrode is connected to a positive potential and all of the other electrodes are connected to earth.

The electric field lines for this situation are shown in Figure 3.7 and are relatively uneven; the field being strongest near to the excited electrode and weakening with increasing distance from this electrode.

The effect of this uneven field distribution is that the change in capacitance measured between any two electrodes caused by an object with a given permittivity will vary depending on the location of the object. The ECT system is most sensitive when an object is placed near the walls of the vessel and is least sensitive at the centre of the vessel. This effect is accounted for using knowledge of the variation of sensitivity with position for each pixel. This information is stored in a sensitivity map. When the ECT system constructs images, it reads the sensitivity map and compensates the image pixels accordingly. In the next section the sensitivity map is used to reconstruct the porosity distribution. Four different reconstruction techniques are discussed.

### Linear back projection

The linear back projection (LBP) reconstruction technique is based on the solution of a set of forward and reverse linear transformations.

The forward transform is a matrix equation which relates the set of inter-electrode capacitance measurements  $C$  to the set of pixel permittivity values  $K$ . This transform assumes that the measured inter-electrode capacitances resulting from any arbitrary permittivity



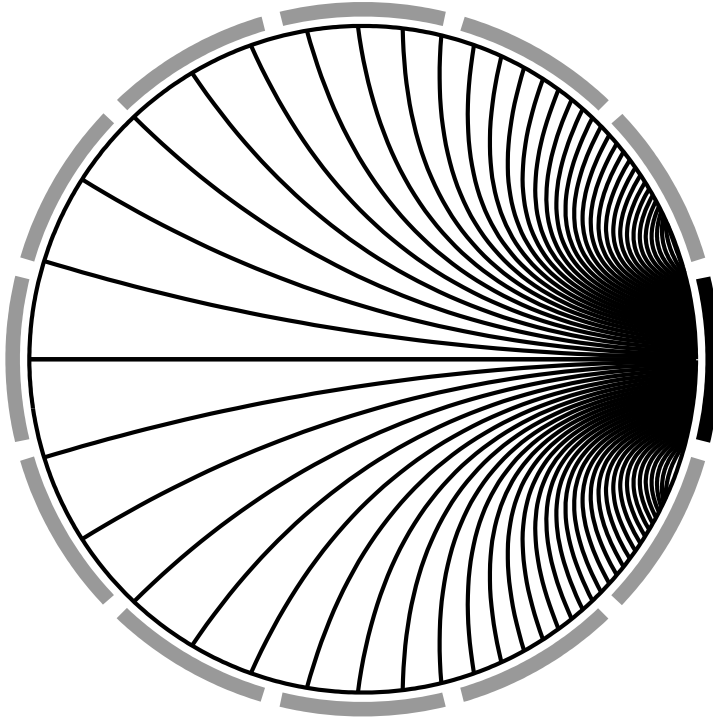


Figure 3.7: Electric flux lines showing the electric field distribution when the electrode on the right (black) is exerted.

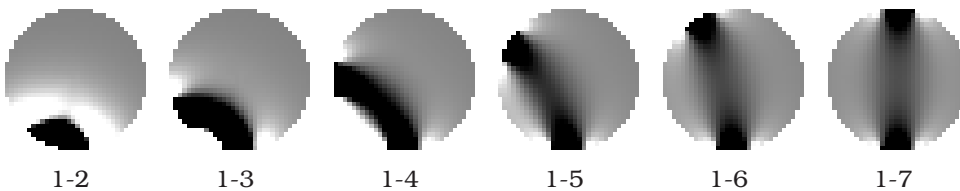


Figure 3.8: Six primary Sensitivity maps, where *black* pixels are influencing the inter electrode capacitance, *grey* pixels have no influence and *white* pixels have negative influence.

distribution  $K$  inside the sensor will be identical to those obtained by summing the component capacitance increases which occur when each pixel has its defined permittivity, with all other pixels values set to zero.

$$C = S \cdot K \quad (3.8)$$

where  $C$  is an array containing 66 measured inter-electrode pair capacitances,  $K$  is an array containing 1024 pixels which describe the permittivity distribution inside the sensor and  $S$  is the sensitivity matrix.  $S$  had the dimensions  $66 \times 1024$ , where the coefficients represent the relative change in capacitance of each capacitance pair when an identical change is made to the permittivity of each of the pixels. Examples of the sensitivity maps are shown in Figure 3.8.

In principle, once the set of inter-electrode capacitances  $C$  have been measured, the permittivity distribution  $K$  can be obtained from:

$$K = S^{-1} \cdot C \quad (3.9)$$

Unfortunately, the inverse of a non-square matrix is not known. In other words, this is confirmation that it is not possible to obtain the individual values of a large number of pixels (1024) from a smaller number of capacitance measurements (66). As an exact inverse does not exist, an approximate matrix must be used. The LBP algorithm uses the transpose of the sensitivity matrix  $S$ , which has suitable dimensions.

$$K = S^T \cdot C \quad (3.10)$$

The LBP reconstruction technique produces approximate, but very blurred permittivity images (see Figure 3.10). To improve the accuracy, an iterative LBP can be used, which is discussed in the next section.

### Iterative LBP

The idea of the iterative LBP is to use two equations alternating to correct the sets of capacitance and pixel values in turn and hence produce a more accurate image from the capacitance measurements.

First, 66 inter-electrode capacitances are measured and the sensitivity map is calculated. Then the permittivity image for the first iteration  $K_1$  is calculated using:

$$K_1 = S^T \cdot C_1 \quad (3.11)$$

Since individual pixel values ( $k$ ) from  $K_1$  can be negative or exceed 1, they are truncated to lie within the range of  $0 < k < 1$ . The new values of  $K_1$  are used to obtain a new set of inter-electrode capacitances for the next iteration ( $C_{i+1}$ ) using:

$$C_{i+1} = S \cdot K_i \quad (3.12)$$

where  $i$  is the iteration number. The capacitance error is obtained via:

$$\Delta C = (C_{i+1} - C_i) \quad (3.13)$$

To improve stability the capacitance errors ( $\Delta C$ ) are limited in the range from -0.05 or 0.05. A new permittivity image is obtained using:

$$\Delta K = S^T \cdot \Delta C \quad (3.14)$$

$$K_{i+1} = (K_i - \Delta K) \quad (3.15)$$

Again, individual pixel values are truncated within the range of  $0 < k < 1$ . Starting from equation 3.12, these steps can be repeated until an accurate image is obtained (see Figure 3.9).

### Tikhonov regularization

It is possible to calculate enhanced transformation matrices which give better quality images than those produced by LBP. A number of different transformation matrices can be used, but two methods which give useful improvements over back-projection are based on methods originally described by Tikhonov and Landweber. In principle, the Landweber method should give similar results to the iterative algorithm when pixel truncation is disabled. Both the Landweber [1951] and Tikhonov and Arsenin [1977] transformation matrices can be obtained from the sensitivity matrix for the sensor.

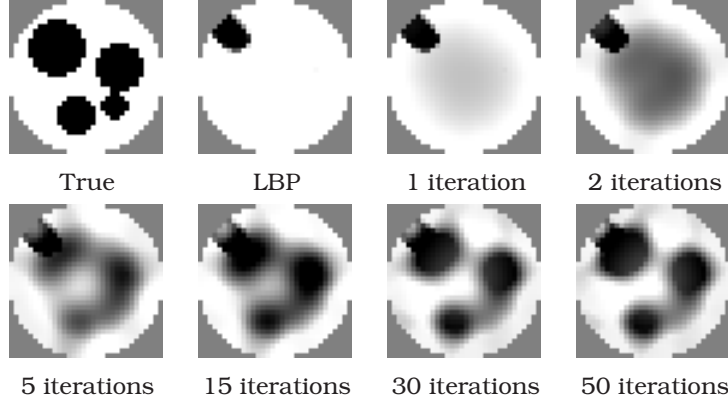


Figure 3.9:  $32 \times 32$  pixel normalized permittivity results for the iterative LBP reconstruction technique. All results are truncated between 0 (*black*) and 1 (*white*). More iterations show an improved result.

The LBP reconstruction technique uses the transpose sensitivity matrix ( $S^T$ ) as transformation matrix (see equation 3.10 and equations 3.16). It is known that the obtained back projected permittivity ( $K_{BP}$ ) is erroneous.

$$K_{BP} = S^T \cdot C \quad (3.16)$$

Replacing the capacitance measurements ( $C$ ) using equation 3.8 results in:

$$K_{BP} = S^T \cdot S \cdot K \quad (3.17)$$

where  $K$  is the true permittivity. Rewriting gives:

$$K = (S^T \cdot S)^{-1} \cdot K_{BP} \quad (3.18)$$

Substituting the back projected permittivity ( $K_{BP}$ ) using equations 3.16 gives:

$$K = (S^T \cdot S)^{-1} \cdot S^T \cdot C \quad (3.19)$$

Instead of using the transpose sensitivity matrix ( $S^T$ ) as in the LBP,  $\frac{S^T}{S^T \cdot S}$  is used. Unfortunately the matrix  $S^T \cdot S$  can have very small numbers at the diagonal or even zero, which would lead to singularity in the permittivity results. Therefore an additional term is introduced:

$$K = (S^T \cdot S + t \cdot I)^{-1} \cdot S^T \cdot C \quad (3.20)$$

where  $I$  is the identity matrix and scalar  $t$  is the Tikhonov constant. High values of the Tikhonov constant give similar results as the LBP, while low values gives noisy results. Typical values of  $t$  are in the range 0.1 to 100.

### Landweber iteration method

The Landweber iteration method is based on singular value decomposition (SVD) of the sensitivity matrix  $S$ .

$$S = U \cdot D \cdot V \quad (3.21)$$

where  $U$  and  $V$  are unitary matrices and  $D$  is a diagonal matrix. This operation can be performed by Matlab. A detailed description of singular value decomposition can be found in several matrix mathematics books or websites. The matrices  $U$  and  $V$  are used to obtain a Landweber sensitivity map ( $S_L$ ).

$$S_L = V \cdot F \cdot U^T \quad (3.22)$$

where elements of the filter matrix  $F$  are defined as:

$$f = \frac{(1 - L \cdot d)^N}{d} \quad (3.23)$$

where  $d$  is an element of the diagonal matrix  $D$ ,  $L$  is the relaxation parameter or the Landweber transformation parameter and  $N$  is the number of iterations. Typical values of  $L$  are in the range of  $10^{-2}$  to  $10^{-4}$ . Low numbers of  $L$  give similar results to the LBP algorithm. The number of iterations  $N$  is typical in the range 10 to 100.

Finally the Landweber sensitivity matrix can be used to obtain the  $32 \times 32$  pixel permittivity plot:

$$K = S_L \cdot C \quad (3.24)$$

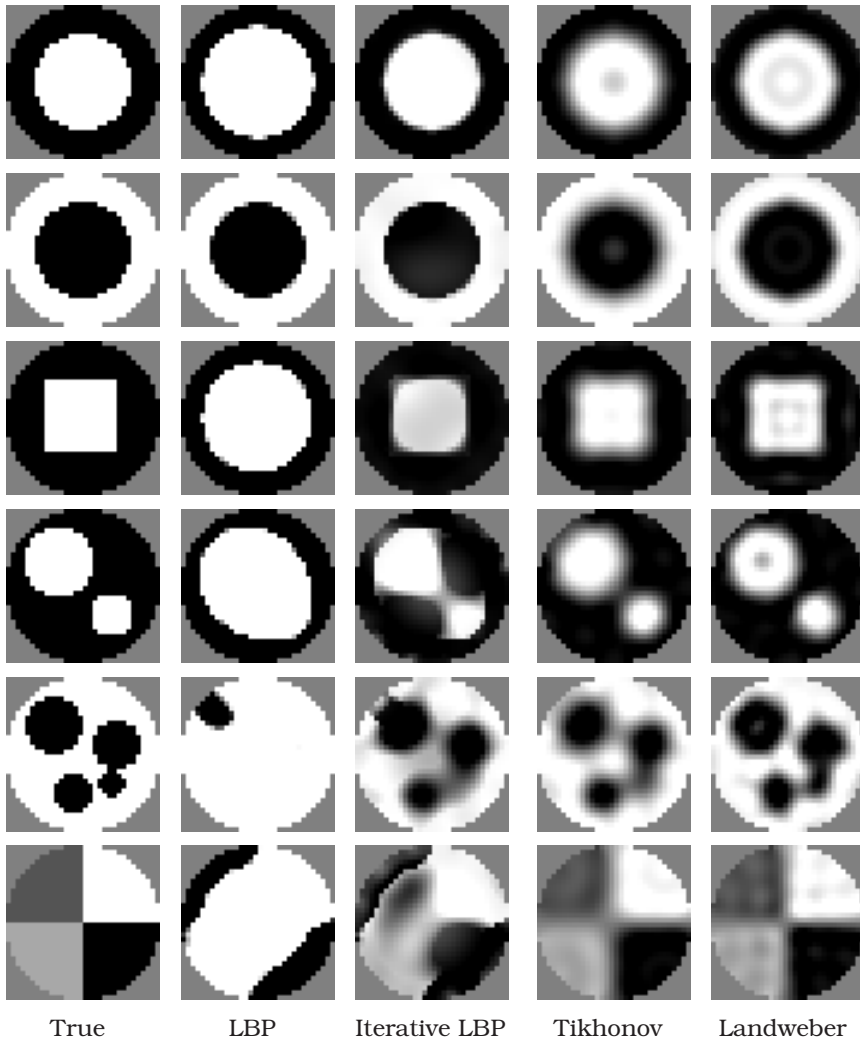


Figure 3.10:  $32 \times 32$  pixel normalized permittivity results of four reconstruction techniques of five generated permittivity distributions with. All results are truncated between 0 (*black*) and 1 (*white*). 50 iterations were used for the iterative LBP, the Tikhonov constant was set to 0.1 and the Landweber constant set to  $10^{-4}$  with 50 iterations.

## Comparison

For all four reconstruction techniques example results are shown in Figure 3.10. Using equation 3.8 a fictitious permittivity distribution ( $K$ ) is used to calculate fictive capacitance data ( $C$ ). The LBP algorithm gives a very smooth result and gives normalised permittivity values over 1 and below 0 (not visible in Figure 3.10). The iterative LBP gives improved results, but has trouble to retrieve the right shape and number of objects. The Tikhonov and Landweber technique gives similar results, if the constants are chosen well.

## 3.5 Concentration models

As mentioned in the previous section permittivity is measured with ECT. The volumetric phase fraction of both components is not linearly correlated to the permittivity. For the correlations typically three different models can be used, depending on the spatial distribution of the material: the parallel, series and Maxwell models. The correlation between the measured permittivity and the actual volume fraction for all three models is shown in Figure 3.12.

Each of the methods requires the relative permittivity of a bed filled with packed particles ( $K_H$ ) and of an empty bed ( $K_L$ ). The relative permittivity of the empty bed filled with air is 1.0 (see Table 3.1). The relative permittivity of a bed filled with packed particles depends on the packing fraction:

$$K_H = \epsilon_{packed} = \epsilon_{glass} \cdot \alpha + \epsilon_{air} \cdot (1 - \alpha) \quad (3.25)$$

where  $\alpha$  is the solids fraction of a randomly packed bed which is around 0.6.

For example glass has a relative permittivity of 6.0, the permittivity of a packed bed with glass particles is just 4.0 as shown in equation 3.25.

### Parallel model

The parallel concentration model is based on parallel oriented sub resolution structure of the high and low permittivity material as shown in Figure 3.11. The derivation of the model is rather straightforward:

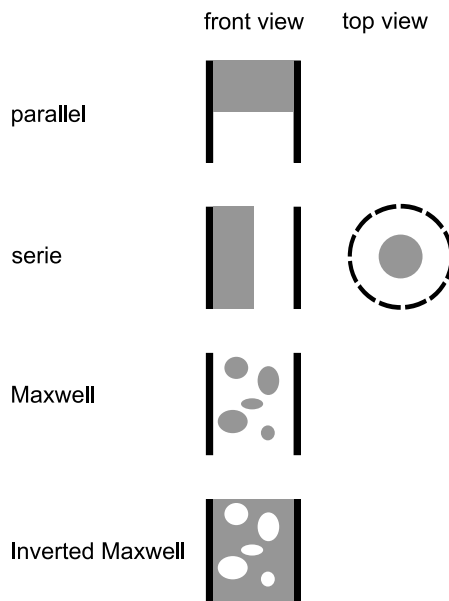


Figure 3.11: Schematic illustration of four concentration models, where *black* are electrodes, *grey* is high permittivity material (particles) and *white* is air. Next to the series model a circular orientation of 12 electrodes is shown.



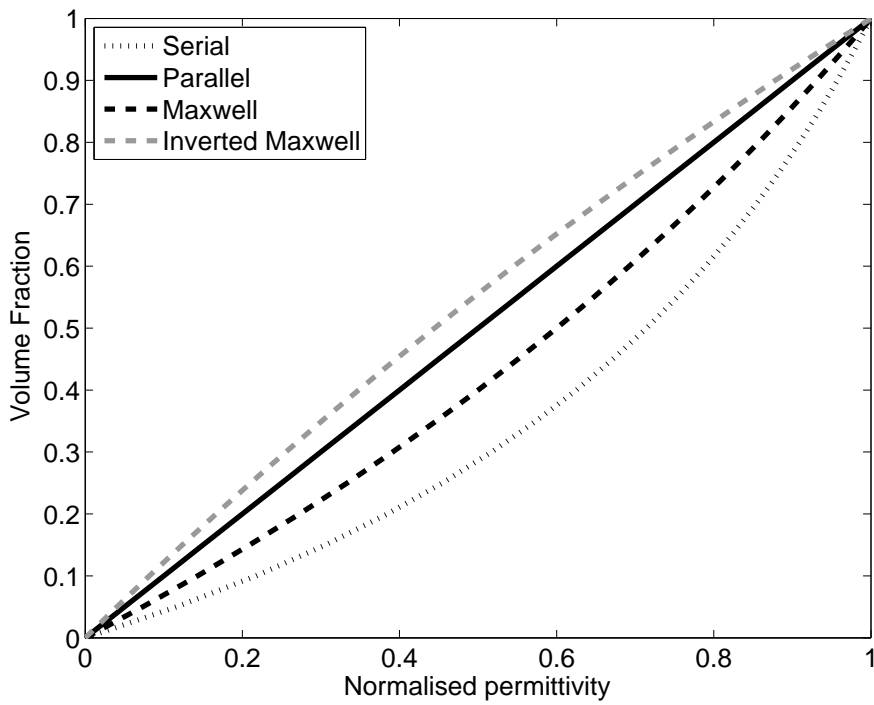


Figure 3.12: Correlation between the measured permittivity and the actual volume fraction for all four concentration models.

$$K_E = K_H \cdot X + K_L \cdot (1 - X) \quad (3.26)$$

where  $K_E$  is the measured permittivity of the mixture.  $X$  is the fraction of the volume filled with the higher permittivity material.  $K_H$  is the absolute permittivity of the higher permittivity material.  $K_L$  is the absolute permittivity of the lower permittivity material.

Normalising equation 3.26 gives:

$$K_{EN} = \frac{K_H \cdot X + K_L \cdot (1 - X) - K_L}{K_H - K_L} \quad (3.27)$$

where  $K_{EN}$  is the normalised measured permittivity of the mixture. Note that this simplifies to:

$$K_{EN} = \frac{K_H \cdot X + K_L - K_L \cdot X - K_L}{K_H - K_L} = X \quad (3.28)$$

In case of the parallel model the normalised capacitance is linearly proportional to the volume fraction or porosity of the bed.

### Series model

The series model assumes layers of material between the electrodes, or in case of an circular sensor it assumes one large object or hole in the bed (see Figure 3.11).

$$\frac{1}{K_E} = \frac{X}{K_H} + \frac{1 - X}{K_L} \quad (3.29)$$

Inverting and normalising equation 3.29 gives:

$$K_{EN} = \frac{\frac{K_L K_H}{K_H} + X(K_L - K_H) - K_L}{K_H - K_L} \quad (3.30)$$

Rewriting equation 3.30 gives:

$$X = \frac{K_H K_{EN}}{K_L + K_{EN}(K_H - K_L)} \quad (3.31)$$

Using the permittivity ratio  $K = \frac{K_H}{K_L}$  this can be further simplified to:

$$X = \frac{K K_{EN}}{1 + K_{EN}(K - 1)} \quad (3.32)$$

### Maxwell model

Based on the work of Maxwell in the 19th century, Yang and Byars [1999] developed a model assuming spheres of the higher permittivity material in the lower permittivity material. The results of this model are shown in equation 3.33 and 3.34

$$K_{EN} = \frac{3X}{2 + K + X(1 - K)} \quad (3.33)$$

$$X = \frac{K_{EN}(2 + K)}{3 + K_{EN}(K - 1)} \quad (3.34)$$

### Inverted Maxwell model

In the case of a fluidized bed bubbles of air (low permittivity) are moving through a polymeric emulsion phase (high permittivity). The Maxwell model described in the previous section is derived for the opposite situation, but can be applied by inverting the permittivity ratio  $K$ . This model we will refer to as the inverted Maxwell model.

$$X = \frac{2K_{EN}K + K_{EN}}{3K + K_{EN} - K_{EN}K} \quad (3.35)$$

In this work we use the inverted Maxwell model since this model represents the bubble emulsion structure best.

## 3.6 Conclusion

In this work we use an advanced calibration technique based on the assumption that the capacitance difference between an empty vessel and a filled vessel remains constant, while both values change over time due to external disturbances.

For the reconstruction we used the Landweber reconstruction technique with the Landweber constant set to  $10^{-4}$  with 50 iterations. This technique and constants were chosen based on two criteria: little permittivity values were found over one and below zero and the technique is able to correctly reconstruct bubble shapes. LBP and iterative LBP give poor results compared to Landweber. Tikhonov regularization gives similar results and could be used as well.

To obtain the concentration from the permittivity data the inverted Maxwell concentration model was used, since it represents the bubble-emulsion structure best, i.e. we have low permittivity bubbles inside a continuous high permittivity emulsion phase.



# 4

## Particle and bubble behaviour in fluidized beds at elevated pressure

### 4.1 Introduction

The discrete particle model is widely used for fluidized beds, but for detailed simulation of gas-pressurized fluidized bed it has rarely been applied. Li and Kuipers [2005] performed several DPM simulations at different operating pressure with particular focus on the effect of the particle-particle collision parameters on the flow structure. Operating pressure plays an important role in the drag force through the gas phase density. Collisional dissipation (particle-particle interaction) causes particles to cluster and results in the formation of bubbles, whereas strong particle-gas interaction reduces this effect. Both these effects were investigated by Li and Kuipers [2005]. They reported the existence of more pronounced homogeneous fluidization at elevated pressure. With the Discrete Particle Model (DPM) one is able represent in detail particle-particle interaction as well as particle-fluid interaction. Therefore this model is very suited to investigate the effect of pressure on fluidization behaviour. In this chapter the DPM is used to investigate the effect of the operating pressure on fluidization behaviour. To make the simulations comparable, a constant excess velocity was applied, contrary to Li and Kuipers [2005] who chose a gas velocity equal to three times the minimum fluidization veloc-

ity. The data produced by the DPM can be analysed in several ways. This chapter consists of three parts: the description of the model, presentation of the simulations settings and analysis results. Results obtained from several analysis methods are discussed: porosity distributions, bubble behaviour, spectral analysis of pressure fluctuations and the granular temperature. Finally the conclusions are presented.

## 4.2 Governing equations

In this section the governing equations of the DPM are briefly discussed. For more details the reader is referred to chapter 2. The discrete particle model (DPM) or Euler-Lagrange model was originally developed by Hoomans et al. [1996]. In the DPM every particle is individually tracked, accounting for particle-particle and particle-wall collisions. The dynamics of the gas phase are described by the volume-averaged Navier Stokes equations:

$$\frac{\partial}{\partial t} (\epsilon_g \rho_g) + \nabla \cdot (\epsilon_g \rho_g \bar{u}_g) = 0 \quad (4.1)$$

$$\frac{\partial}{\partial t} (\epsilon_g \rho_g \bar{u}_g) + \nabla \cdot (\epsilon_g \rho_g \bar{u}_g \bar{u}_g) = -\epsilon_g \nabla p - \nabla \cdot (\epsilon_g \bar{\tau}_g) - \bar{S}_p + \epsilon_g \rho_g \bar{g} \quad (4.2)$$

where  $\bar{u}_g$  is the gas velocity and  $\bar{\tau}_g$  represents the gas phase stress tensor. The sink term  $\bar{S}_p$ , represents the drag force exerted on the particles:

$$\bar{S}_p = \frac{1}{V_{cell}} \int_{V_{cell}} \sum_{i=0}^{N_{part}} \frac{V_i \beta}{1 - \epsilon_g} (\bar{u}_g - \bar{v}_i) D(\bar{r} - \bar{r}_i) dV \quad (4.3)$$

where  $\bar{v}_i$  is the velocity of particle  $i$ .

The distribution function  $D(\bar{r} - \bar{r}_i)$  is a discrete representation of a Dirac delta function that distributes the reaction force acting on the gas phase to the Eulerian grid via a volume-weighting technique. The inter-phase momentum transfer coefficient,  $\beta$  describes the drag of the gas-phase acting on the particles.

The Ergun [1952] and Wen and Yu [1966] equations are commonly used to obtain expressions for  $\beta$ . However, we use the closure relation

derived by Koch and Hill [2001] based on lattice Boltzmann simulations, since this drag closure does not exhibit discontinuities at high Reynolds numbers and yields good results as reported by Bokkers et al. [2004] and Link et al. [2005]. The particle motion is described by Newton's second law:

$$m_i \frac{d\bar{v}_i}{dt} = -V_i \nabla p + \frac{V_i \beta}{\epsilon_s} (\bar{u} - \bar{v}_i) + m_i \bar{g} + F_i^{pp} + F_i^{pw} \quad (4.4)$$

where the forces on the right hand side are, respectively due to pressure, drag, gravity, particle-particle interaction and particle-wall interaction.

The angular velocity the angular momentum equation is given by:

$$\bar{I}_i \frac{d\bar{\omega}_i}{dt} = \bar{T}_i \quad (4.5)$$

The contact forces are caused by collisions with other particles or confining walls. These collisions are described with a soft-sphere approach. In our approach a linear spring/dash-pot model has been adopted, wherein the velocities, positions and collision forces of the particles are calculated using a fixed time step and first order time integration [Hoomans et al., 1996]. The collision model takes into account restitution and friction effects. The associated collision coefficients were obtained experimentally via the method of Kharaz et al. [1999]. They developed a sophisticated experimental method to obtain collision parameters for different impact angles. For a more detailed discussion of this model we refer to chapter 2 and the review paper by Van der Hoef et al. [2006].

### 4.3 Simulation settings

To investigate the pressure effect on the fluidization behaviour seven full three dimensional DPM simulations at 1, 2, 4, 8, 16, 32 and 64 bar were performed. The system properties and operating conditions are specified in Tables 4.1 and 4.2 respectively.

The coefficients of restitution and the friction coefficients used in the simulations were measured according to the method described by Kharaz et al. [1999]. No-slip boundary conditions were used at the confining walls.



Table 4.1: Settings for all seven simulations.

Property	Symbol	Value	Unit	
System width	$X$	0.025	$m$	(20 cells)
System depth	$Y$	0.025	$m$	(20 cells)
System height	$Z$	0.1	$m$	(80 cells)
Time step	$dt$	$1.0 \cdot 10^{-4}$	$s$	
Total time	$t$	10	$s$	
Number of particles	$N_{part}$	$2.86 \cdot 10^5$	–	
Particle diameter	$d_p$	0.5	$mm$	
Particle density	$\rho$	925	$kg/m^3$	
Normal spring stiffness	$k_n$	200	$N/m$	
Coefficient of normal restitution	$e_n$	0.8	–	
Coefficient of tangential restitution	$e_t$	0.6	–	
Friction coefficient	$\mu$	0.1	–	

Table 4.2: Superficial gas velocities for all seven simulations

<b>P(bar)</b>	$u_{mf}(m/s)$	$u_{sup}(m/s)$
1	0.088	0.265
2	0.084	0.261
4	0.077	0.253
8	0.067	0.244
16	0.056	0.233
32	0.044	0.221
64	0.033	0.210

In order to enable a fair comparison between the simulations, a constant excess velocity (i.e. superficial gas velocity minus minimum fluidization velocity) of  $0.177 m/s$  was applied (see Table 4.2).

## 4.4 Results

From the DPM simulation data several results can be obtained. In this section porosity distributions, bubble behaviour, spectral analysis of pressure fluctuations and granular temperature are presented.

### 4.4.1 Porosity distribution

The applied operating pressure has a profound influence on the bubble behaviour as can be seen in Figure 4.1. From these snapshots it can be observed that bubbles become smaller with increasing pressure. Moreover, at higher pressures it becomes harder to distinguish

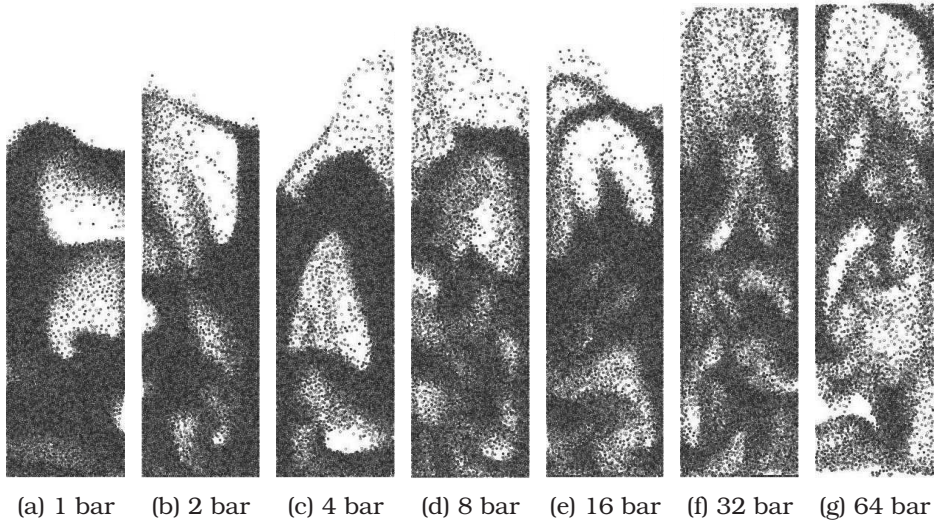


Figure 4.1: Snapshots of particle positions in a slice in the centre of the bed with a depth of one computational cell at different operating pressures. At 32 and 64 bar the top of the bed is not shown.

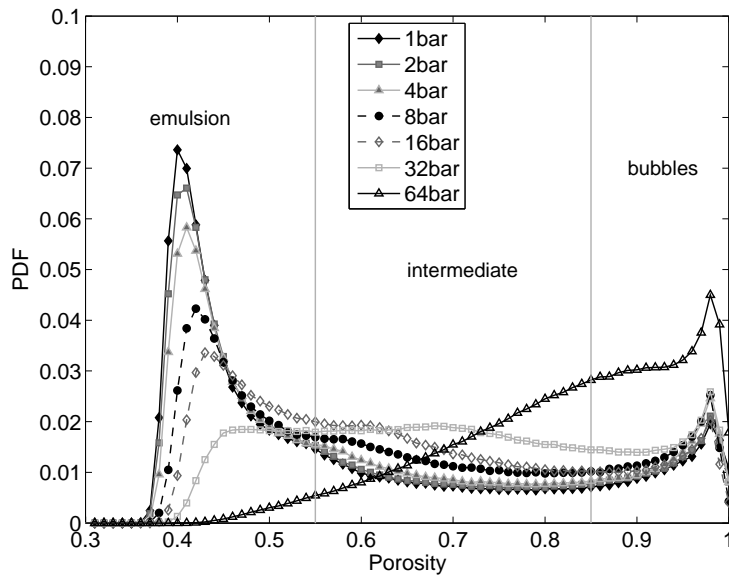


Figure 4.2: PDF of time-averaged porosity distribution at different operating pressures.

bubbles from the emulsion phase. From animations, it was observed that bubbles move more chaotically. To quantify the effect of the operating pressure on the bubble behaviour, a probability density function (PDF) of the local porosity was obtained from 8 s of simulation data, using the porosity from each cell and every time step. In Figure 4.2 a normalised PDF of the porosity distribution is shown. Pressure influences the PDF significantly. For pressures of 16 bar and lower, we see a clear peak around a porosity of 0.40 - 0.45, representing the emulsion phase. Notice that (dense) packed spheres possess a porosity of 0.26 and randomly packed particles have a porosity of about 0.4. For porosities above 0.95 we see a small peak caused by bubbles. An intermediate area with porosities between 0.45 and 0.90 is formed in areas located around bubbles or in developing or collapsing bubbles. With increasing pressure the emulsion phase becomes less dense, while the bubbles contain more particles. The simulation of 32 bar does not show any peak for the emulsion phase. Hence, in that case there is no clear distinction anymore between the emulsion, intermediate and bubble phases. At 64 bar the hydrodynamics change even more so that a new peak is formed around 0.83.

#### 4.4.2 Bubble behaviour

The results from the previous section indicate that the formation and dynamics of bubbles play an important role for the overall bed dynamics. The effect of bubbles on fluidized bed hydrodynamics and performance has been studied extensively in literature. Since the bubbles are responsible for the mixing in a fluidized bed, many important bubble properties, such as rise velocity, size, shape and wake size have been determined experimentally. The formation of heterogeneous structures such as bubbles is a direct outcome of the discrete particle simulation. In order to detect these structures, enabling subsequent analysis and direct comparison with experimental data, a bubble detection algorithm is required. In this study we report an algorithm that can distinguish bubbles from the emulsion phase. The algorithm essentially consists of three steps: calculation of the porosity field, determination of a threshold value for the porosity and correlation of detected bubbles. First we calculate the porosity for each computational cell, by subtracting the volume of the particle phase from the volume associated with that cell (Figure 4.3b). Small clus-

ters of particles disturb the detection, causing small 'holes' in the bubbles and difficulties in detecting the bubble edge. Therefore we smooth the porosity plot by applying a moving average filter with a size of  $3 \times 3 \times 3$  cells (Figure 4.3c). In the second step a threshold value for the porosity is determined. In order to identify bubbles of varying porosity a variable threshold value was used. Areas with a porosity above the threshold value are attributed to the bubbles, whereas the remainder of the cells are attributed to the emulsion phase. We use a local threshold value to be able to distinguish between very porous bubbles surrounded by a porous emulsion phase and small, less porous bubbles surrounded by a dense emulsion phase. To prevent the threshold to become too large or too small the threshold value is limited as follows.

$$\epsilon_{th} = \max(\epsilon_{min}, \epsilon_{loc}) \quad (4.6)$$

where  $\epsilon_{loc}$  is the local porosity of the emulsion phase, which is calculated as:

$$\epsilon_{loc} = \max_{x \in \Omega}(\epsilon_x) + (\epsilon_{max} - 1.0) \quad (4.7)$$

where  $\epsilon_{min} = 0.6$  and  $\epsilon_{max} = 0.8$  are the minimum and maximum threshold values and the domain ( $\Omega$ ) is a  $9 \times 9 \times 9$  cells grid around the local grid cell (Figure 4.3d). From equation 4.7 it can be obtained that for a domain containing a cell without particles the threshold value is 0.8. The numerical values used for determining the threshold were found to give the best accordance between visual detection and the detection results. To prevent grid size dependency, after  $\epsilon_{loc}$  has been obtained for each grid cell a moving average filter of  $9 \times 9 \times 9$  cells is applied (Figure 4.3e).

After all cells have been identified all bubble cells which are connected to each other are attributed to the same bubble (Figure 4.3f). The bubble position, i.e. the centre of mass and equivalent bubble radius can be easily calculated from the average cell position and number of cells pertaining to the bubble, respectively (Figure 4.3g).

In the third and final step of the bubble detection algorithm two subsequent detection results are correlated in order to calculate the bubble rise velocity. Bubbles in two subsequent bubble maps that are less than one bubble radius apart, are considered to constitute

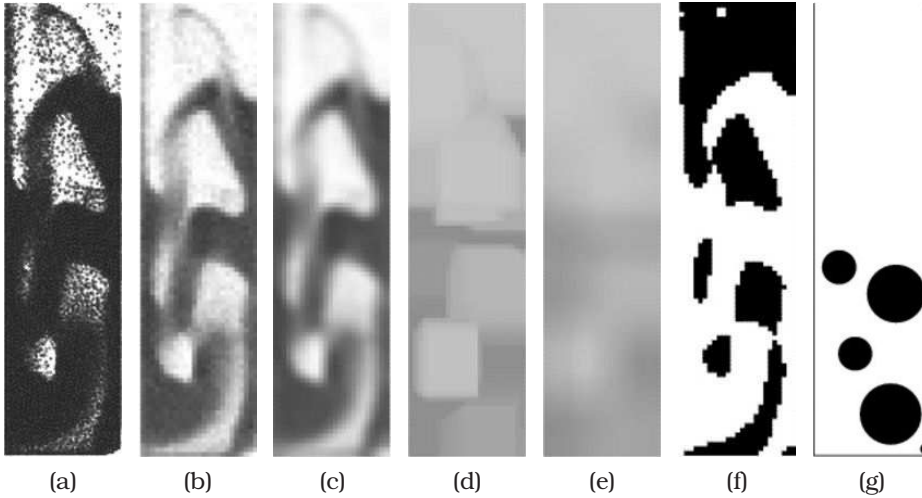


Figure 4.3: Snapshots showing intermediate results of the bubble detection algorithm: a) the particle positions; b) porosity of the bed; c) smoothed porosity; d) threshold value ( $\epsilon_{th}$ ); e) smoothed threshold value; f) bubble detection results; g) equivalent bubble diameter.

the same bubble. From the bubble displacement between two subsequent detection results the bubble velocity can be calculated. If coalescence or break-up occurs, the involved bubbles will move more than one bubble radius, and the bubble positions are discarded in the velocity calculation. For practical purposes the relative bubble velocity, i.e. the slip velocity is much more relevant than the absolute bubble velocity. To this end we also require the emulsion velocity, which is calculated by averaging the velocity of all the particles in a one grid cell thick layer surrounding the bubble. The slip velocity is subsequently calculated as:

$$v_{\infty} = v_b - v_e \quad (4.8)$$

where  $v_b$  and  $v_e$  are the velocities of the bubble and the surrounding emulsion phase, respectively.

In Figure 4.4 the average bubble size versus the bed height is shown. At low pressure we see a continuously increasing bubble size caused by bubble growth and coalescence. At higher pressures however a more flat profile of the average bubble size is observed. At 32 bar the average bubble size at the top of the bed is smaller than in

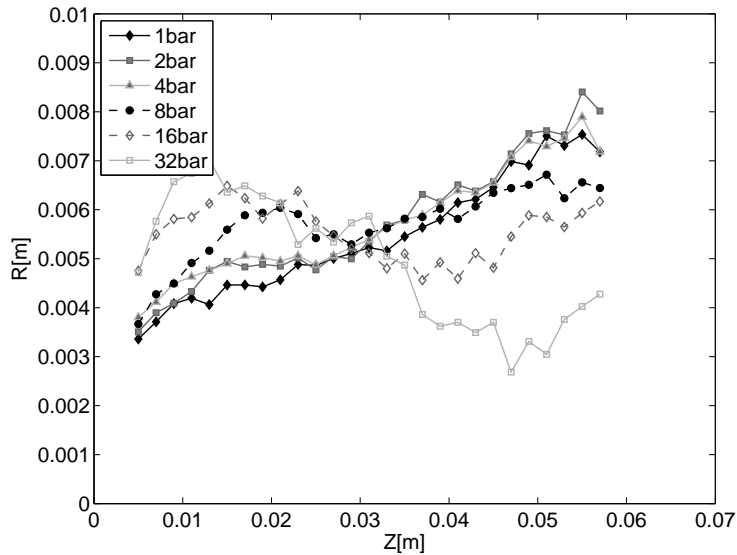


Figure 4.4: Equivalent bubble radius, calculated by bubble detection algorithm, as a function of bed height.

the bottom of the bed. Probably this effect is caused by more vigorous fluidization and the inability of the algorithm to detect individual bubbles. At 64 bar the bubble detection algorithm fails and cannot detect bubbles anymore.

In Figure 4.5 snapshots of the particle positions at different operating pressures are shown. A distinctly different bubble behaviour can be discerned from this figure. At elevated pressures the bubbles tend to be smaller. Furthermore the porosity distribution becomes more homogeneous, as was observed before.

The bubble size distribution calculated on basis of the bubble detection results is shown in Figure 4.6. Bubbles, smaller than 1 mm, are not detectable and are therefore not taken into account. In all cases the mean bubble radius is about 3 mm. At increasing pressure more bubbles larger than 7 mm are observed. Bubbles exceeding a size of 12 mm are hardly seen, since the bed width is 25 mm. From visual inspection of porosity maps of the bed it was found that in general the bubble size decreases with increasing pressure. However this trend is not seen in Figure 4.6 which has two reasons. Small bubbles cannot be detected since they have similar sizes compared to the computational cells. For this reason, a decrease in bubble size

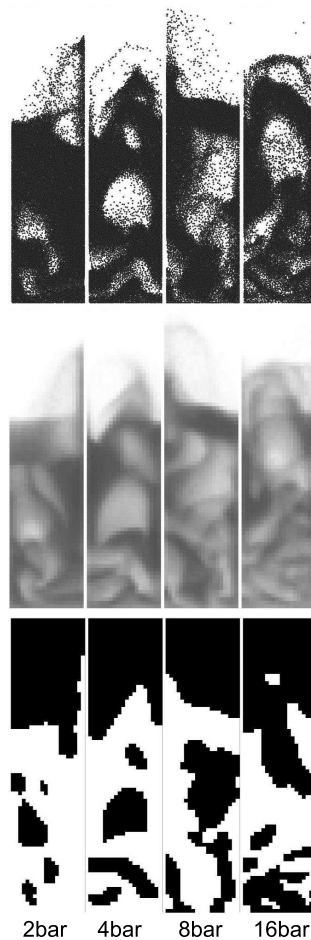


Figure 4.5: Bubble detection results. **Top row:** Snapshots of the instantaneous particle positions at different pressures. **Middle row:** Porosity plots from the snapshots of the DPM results at 2, 4, 8 and 16 bar. Only a slice of one cell deep in the middle of the bed is shown. **Bottom row:** Bubble detection results of the snapshots shown in the middle row. The black cells are attributed to bubbles.

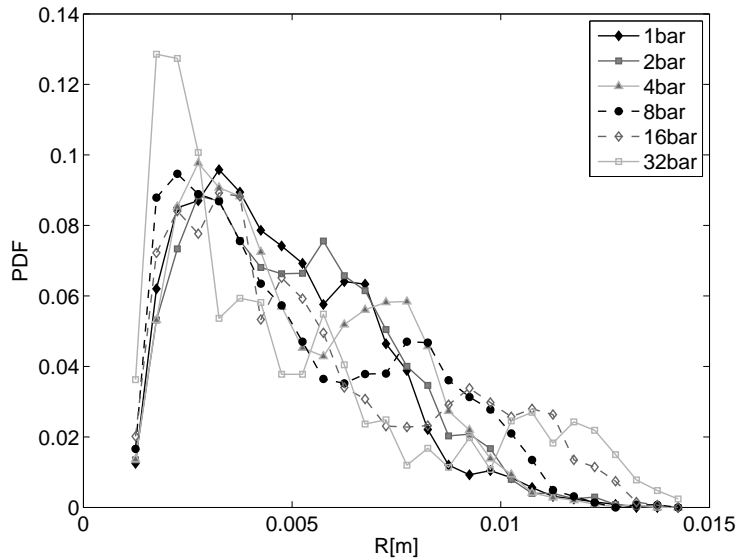


Figure 4.6: The PDF of the bubble radius distribution of six simulations.

is difficult to detect. In addition it is difficult to detect bubbles at pressures exceeding 16 bar, because the bubble-emulsion structure is less distinct in this case.

Based on experiments Davidson and Harrison [1963] derived the following expression for the bubble rise velocity:

$$v_b = 0.711\sqrt{d_b g} \quad (4.9)$$

Chan et al. [1987], Olowson and Almstedt [1990, 1991, 1992], Wiman and Almstedt [1998] reported similar equations for the bubble rise velocity with a slightly modified leading constant.

In Figure 4.7 the simulation results are shown along with the Davidson and Harrison [1963] relation. In general, the shape of the curves and the magnitude of the bubble velocity are in reasonable accordance with the Davidson and Harrison expression. At low operating pressures, the bubble rise velocities exceed the Davidson and Harrison relation. Davidson and Harrison [1963] studied the steady rise velocity of isolated bubbles in an otherwise undisturbed fluidized medium at atmospheric conditions. The difference is probably caused by the upward flow of the emulsion phase surrounding the bubbles. The effect of the emulsion movement can be eliminated by subtract-



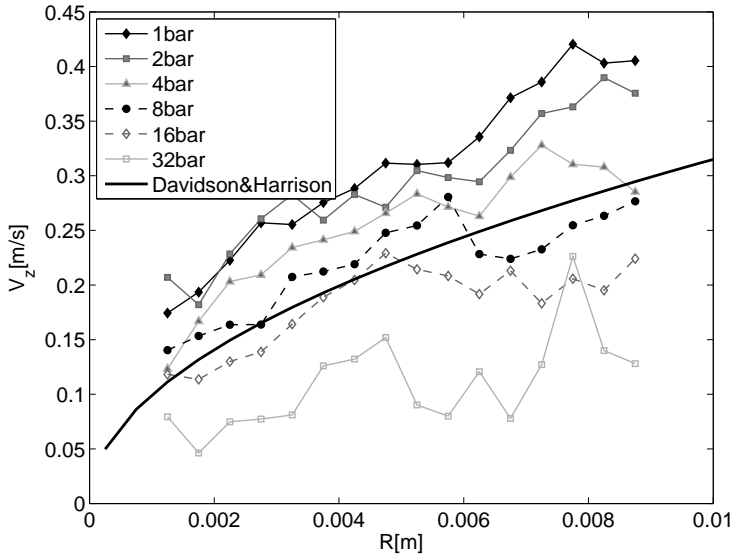


Figure 4.7: The bubble velocity versus the bubble radius. For reference purposes the Davidson and Harrison relation is included.

ing the emulsion velocity, as described earlier, yielding a better correspondence with the Davidson and Harrison relation, as shown in Figure 4.8. Especially the results for low operating pressures are very well in accordance.

The results presented in the previous section are subject to some analysis difficulties, leading to some uncertainties in the obtained results. In this section we will discuss some of the aspects related to the choices made in the bubble detection algorithm, the applied bed dimensions and the interpretation of bubble sizes near the wall and at elevated pressures. In this work, the dimensions of the simulated fluidized bed are rather limited, i.e.  $0.025 \times 0.025 \times 0.1 \text{ m}^3$ . The reason that a relatively small bed was used is of a practical nature; due to the high number of particles in the system (i.e.  $2.86 \cdot 10^5$ ) the computation time for one discrete particle simulation for a system of this size is in the order of one month, which is just acceptable. As a result of the computational and hence dimensional limitations, the predicted bubble sizes are restricted by the size of the bed. Furthermore, wall effects such as a strong particle down flow near the wall will influence the bubble behaviour. Bubbles near the wall tend

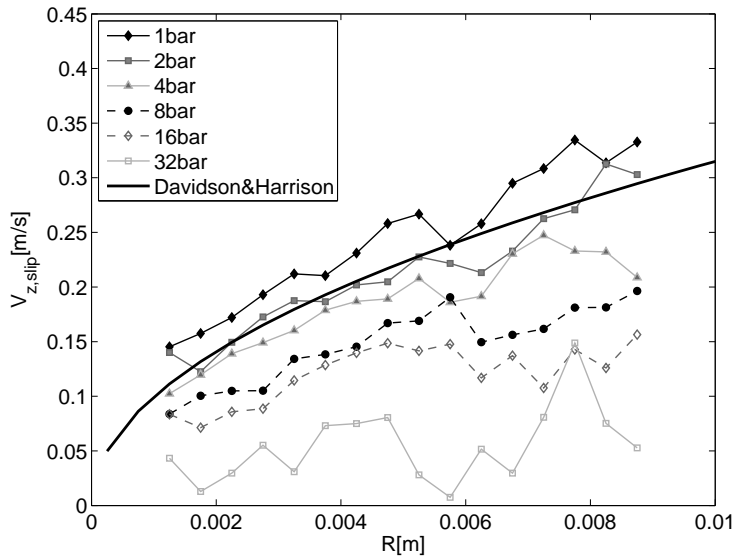


Figure 4.8: The bubble slip velocity versus the bubble radius. The simulation results are compared with the Davidson and Harrison relation.

to slow down and become strongly asymmetrical as is shown in Figure 4.9. In large-scale industrial scale fluidized beds the walls are less important, because these beds are typically metres wide. We partly eliminate wall effects on the bubble rise velocity by subtracting the emulsion phase velocity, yielding the bubble slip velocity, which can directly be compared to the rise velocity of bubbles in an undisturbed bed (in this case the emulsion phase velocity is zero). Furthermore, bubble sizes are bound by the bed dimensions. As indicated before, the bubble-emulsion structure becomes less distinct with increasing pressure (see Figure 4.5). One should bear in mind that the ability to distinguish individual bubbles diminishes with increasing pressure.

#### 4.4.3 Spectral analysis of pressure fluctuations

Gas flow more easily through the bubbles compared to the emulsion; leading to a lower pressure inside the bubbles. Due to the continuous passage of bubbles through the fluidized bed, the pressure drop measured over the bed height is continuously fluctuating. Link et al. [2005] proposed a method to apply spectral analysis to DPM results. By recording the pressure drop over the bed as a function of time and



Figure 4.9: Snapshot of the bed porosity in the case where two bubbles are present. The lower bubble slows down near the wall and is much more asymmetric than the bubble in the core of the bed.

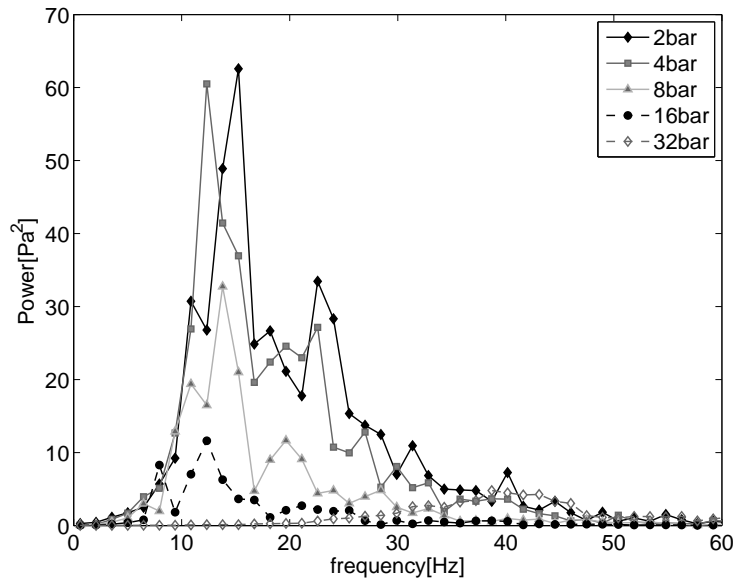


Figure 4.10: Power spectra of the pressure drop fluctuations of five simulations at operating pressures of 2, 4, 8, 16 and 32 bar.

applying a Fourier transformation to the pressure signal, they were able to obtain the pressure fluctuation frequency spectrum. A similar analysis was made to the current DPM simulation data. To this end, the pressure is averaged over the top and the bottom planes of the bed every 4 ms. Subsequently a Fourier transformation over 2048 data points was performed. Spectral analysis was applied to the bed pressure drop signal, the results of which are shown in Figure 4.10. We see that the power of the spectrum decreases with increasing pressure. This implies that the pressure drop fluctuations decrease with increasing pressure, which is a result of the smaller bubble size and reduced heterogeneity of the system. At 32 bar the peak disappears due to vigorous chaotic fluidization. Furthermore, it is observed that the main peaks tend to shift to lower frequencies as the pressure is increased. This suggests that the frequency of bubbles passing through the bed is lower. In order to check this hypothesis, the mean frequency resulting from the spectral analysis is compared with the bubble passage frequency obtained from the bubble detection method (see Table 4.3). In the bubble detection algorithm the bubble passage frequency was determined by counting the number of bubbles pass-

Table 4.3: Comparison of the bubble passage frequency calculated from the bubble detection algorithm results and the average frequency of the spectral analysis.

Operating pressure	Bubble passage frequency	
	Bubble detection algorithm	Spectral analysis
2 bar	22.9 Hz	21.1 Hz
4 bar	20.0 Hz	19.3 Hz
8 bar	14.3 Hz	18.1 Hz
16 bar	12.3 Hz	16.8 Hz
32 bar	4.1 Hz	32.7 Hz

ing a virtual plane at a height of 0.03 m. This height was chosen since it is in the middle of the bed. No new bubbles are formed at this height and hardly any bubbles collapse.

While the shape of the spectrum is not changing that much, the bubble passage frequency measured with the bubble detection algorithm gradually decreases with pressure. This decrease is especially important between 4 and 8 bar.

The trend seen in the bubble detection algorithm is similar to the average frequency peak from the bubble passage spectrum, but the values differ, especially for the case with operating pressure of 8 and 16 bar. Results for simulations at 32 bar should be ignored since many bubbles passages are not detected. The spectral analysis did not shown a clear peak for the simulation at 32 bar for the same reason.

#### 4.4.4 Granular Temperature

The DPM simulation data allows us to calculate the granular temperature which is related to the particle velocity fluctuation due to particle-particle interaction. The granular temperature is a very important quantity in the kinetic theory of granular flow (KTGF) which forms the basis of the two-fluid model (TFM). In the TFM, the particulate phase is described as a continuous phase. Hence, an alternative description of the particle-particle interaction is required. The DPM can be used to verify the basic assumptions underlying the KTGF. Only very few groups calculated the granular temperature from more detailed models such as the discrete particle model (DPM). Gera [2003] compared DPM results with TFM results, and concluded that anisotropy plays a significant role in the bubble characteristics. Gold-

schmidt et al. [2001] developed a method to obtain the granular temperature from the DPM results and investigated the effect of collision parameters. In this work we use the DPM to gain insight into the effect of operating pressure on the granular temperature. To the best of our knowledge these effects have not been investigated before. We used a similar method as Goldschmidt et al. [2001] for calculating the granular temperature. Contrary to their work, we base our analysis on full 3D simulations rather than pseudo 2D simulations. Therefore, particles have one extra degree of freedom, which might influence the results.

Goldschmidt et al. [2002] developed a sampling method to obtain the granular temperature from DPM data. In this section we will use a similar method for obtaining the granular temperature and subsequent analysis. For the determination of the granular temperature the bed is divided into small sub-volumes or 'cells'. The grid size is chosen in such a way that a sufficient number of particles is present in each cell, while ensuring that the particles in the sampling cell have a correlated mean velocity. The grid size is chosen as  $15 \times 15 \times 60$  cells ( $W \times D \times H$ ), so that each cell contains on average around 20 particles. Note that the results are somewhat grid-dependent by nature. That is, when the grid size is reduced, the particle dynamics will become more homogeneous, leading to a lower granular temperature. On the other hand, when the grid size is increased, more spatial variations of the particle dynamics will come into play, leading to a higher granular temperature. The applied grid size is of the same order of that used for continuum models, enabling a direct comparison. In the kinetic theory of granular flow the actual particle velocity  $\bar{v}$  is decomposed into a local ensemble mean solids velocity  $\bar{u}_s$  and a random fluctuation  $\bar{C}$  according to:

$$\bar{v} = \bar{u}_s + \bar{C} \quad (4.10)$$

The  $x$  component of the granular temperature of the ensemble in each cell  $k$  is calculated according to:

$$\theta_{k,x} = \frac{1}{N_{part,k}} \sum_i^{N_{part,k}} C_{i,x}^2 = \frac{1}{N_{part,k}} \sum_i^{N_{part,k}} (v_{i,x} - u_{s,i,x})^2 \quad (4.11)$$

where:

$$u_{s,i,x} = \frac{1}{N_{part,k}} \sum_i^{N_{part,k}} v_{i,x} \quad (4.12)$$

Granular temperatures for the  $y$  and  $z$  directions are calculated in a similar way. The overall granular temperature is obtained from equation 4.12 with contributions from all spatial directions.

$$\theta_k = \frac{1}{3} \frac{1}{N_{part,k}} \sum_i^{N_{part,k}} \bar{C}_i^2 = \frac{1}{3} \frac{1}{N_{part,k}} \sum_i^{N_{part,k}} (\bar{v}_i - \bar{u}_{s,k})^2 \equiv \frac{1}{3} (\theta_{k,x} + \theta_{k,y} + \theta_{k,z}) \quad (4.13)$$

where:

$$\bar{u}_{s,k} = \frac{1}{N_{part,k}} \sum_i^{N_{part,k}} \bar{v}_i \quad (4.14)$$

Cells that do not contain particles or just one particle are not taken into account, because in those cases no granular temperature can be determined.

The velocity distribution functions are determined with the aid of a sampling procedure using  $16 \times 25$  discrete classes, as shown in Figure 4.11. The granular temperatures that are obtained, range from  $1 \cdot 10^{-5}$  up to  $1 \cdot 10^{-1} \frac{m^2}{s^2}$ . This range is split into 16 classes of size  $\Delta \log_{10} \theta = 0.25$ . So the first class ranges from  $\theta = 1.0 \cdot 10^{-5} \frac{m^2}{s^2}$  to  $1.78 \cdot 10^{-5} \frac{m^2}{s^2}$ , and the second class from  $1.78 \cdot 10^{-5} \frac{m^2}{s^2}$  to  $3.16 \cdot 10^{-5} \frac{m^2}{s^2}$ , etc. The velocity distribution within each granular temperature class is also split into 25 discrete classes. For the  $x$ ,  $y$  and  $z$  direction these classes have a width of  $0.25\sqrt{\theta}$ . The first class contains all values  $c < -2.875\sqrt{\theta}$  and the last class contains all values  $c > 2.875\sqrt{\theta}$ . For the absolute velocity the classes are chosen differently, since the absolute velocity is positive by definition. For the latter, the first class starts at 0 and the last class contains values above  $6.0\sqrt{\theta}$ . We simulated 10 seconds, but for the analysis we ignored the first 2 seconds, to prevent start-up effects influencing the results. From the remaining 8 seconds, we sample the data every 0.04 s, corresponding to snapshots. This method ensures that for all velocity distributions at least  $5.7 \cdot 10^7$  individual particle velocities are used.

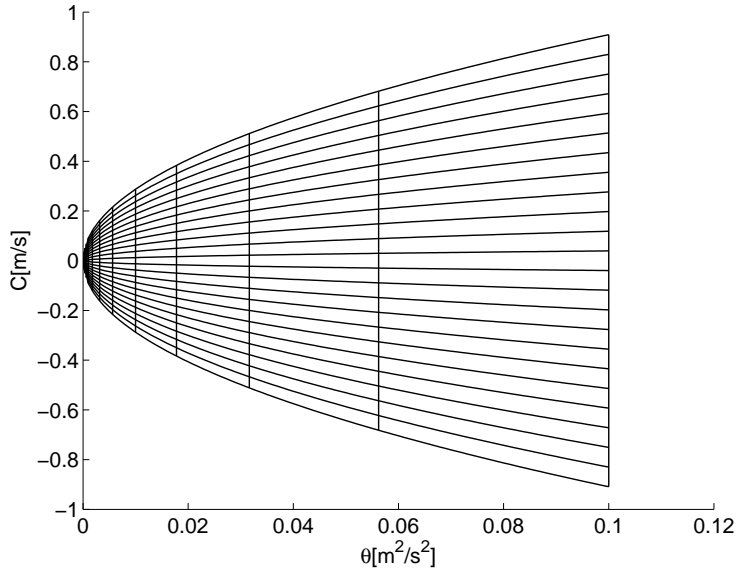


Figure 4.11: Classes used for the distribution of the granular temperature. The ranges of the granular temperature ( $\theta$ ) and velocity fluctuation ( $C$ ) are split into 16 and 25 classes, respectively.

As shown in Figure 4.12 we obtain a Gaussian distribution for the velocity components in  $x$ ,  $y$  and  $z$  direction and a Maxwellian distribution for the velocity vector, similar to the results of Goldschmidt et al. [2002], who performed pseudo 2D simulations with  $25 \cdot 10^3$  particles. In our work the simulations are fully three-dimensional and ten times more particles are used. Compared to pseudo 2D simulation, the particles in 3D simulations have an extra degree of freedom, influencing the granular temperature. The distributions for all pressures are similar, therefore only the distributions for 16 bar are shown in Figure 4.12.

The granular temperature is significantly influenced by the operating pressure as is shown in Figure 4.13. The average value increases from  $3.0 \cdot 10^{-3}$  to  $4.2 \cdot 10^{-3} \frac{m^2}{s^2}$  with operating pressure, while the distribution of  $\theta$  remains unchanged.

The increase of granular temperature with increasing pressure is anisotropic, as can be observed from Figure 4.14. In the  $x$  and  $y$  direction the granular temperature increases very little with increasing pressure, while for the  $z$  direction the granular temperature in-



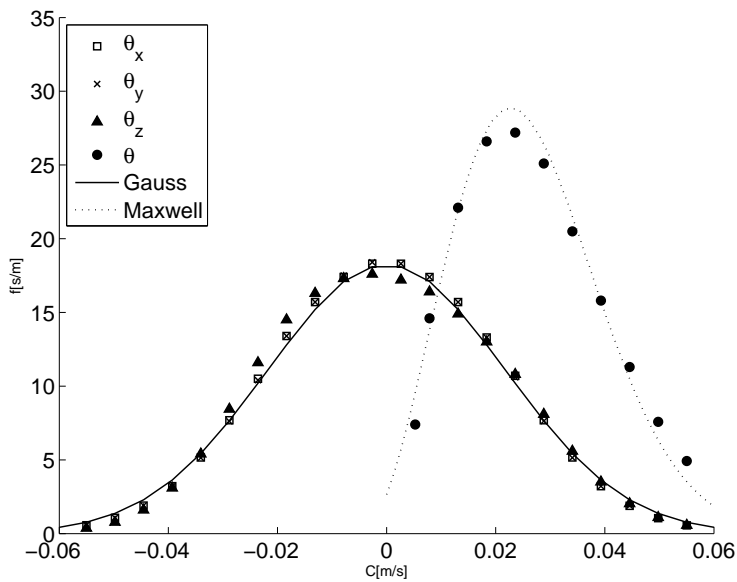


Figure 4.12: Normalised velocity distribution for  $x$ ,  $y$ ,  $z$  and absolute velocity for simulation at an operating pressure of 16 bar, sampled in the range of  $3.16 \cdot 10^{-3} \frac{m^2}{s^2} < \theta < 5.62 \cdot 10^{-3} \frac{m^2}{s^2}$ . Note that the distributions in  $x$  and  $y$  direction are completely overlapping.

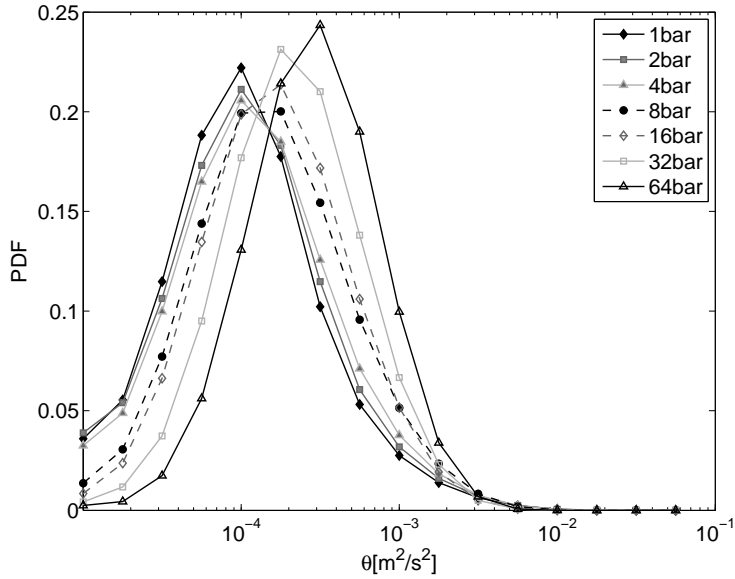


Figure 4.13: Granular temperature distribution at different operating pressures.

Table 4.4: Anisotropy of the granular temperature for simulations at different operating pressures.

	<b>1bar</b>	<b>2bar</b>	<b>4bar</b>	<b>8bar</b>	<b>16bar</b>	<b>32bar</b>	<b>64bar</b>
$\theta_x/\theta$	0.77	0.77	0.74	0.72	0.70	0.66	0.55
$\theta_y/\theta$	0.77	0.75	0.75	0.70	0.70	0.65	0.56
$\theta_z/\theta$	1.45	1.48	1.51	1.58	1.60	1.70	1.89

creases significantly. At elevated pressure, the density of the gas phase increases, leading to a higher form drag. Due to the fact that the fluidizing gas predominantly flows in the vertical direction, the particles will experience more drag in that direction than in the horizontal direction, explaining the increased anisotropy in the granular temperature.

The increase of the granular temperature with increasing pressure is closely linked to the changes in the porosity distributions. At elevated pressures and therefore high bed porosities, particles have more space to move randomly, while in dense zones, all particles are forced to have approximately the same velocity. If we eliminate the porosity effects and merely consider the granular temperature at different

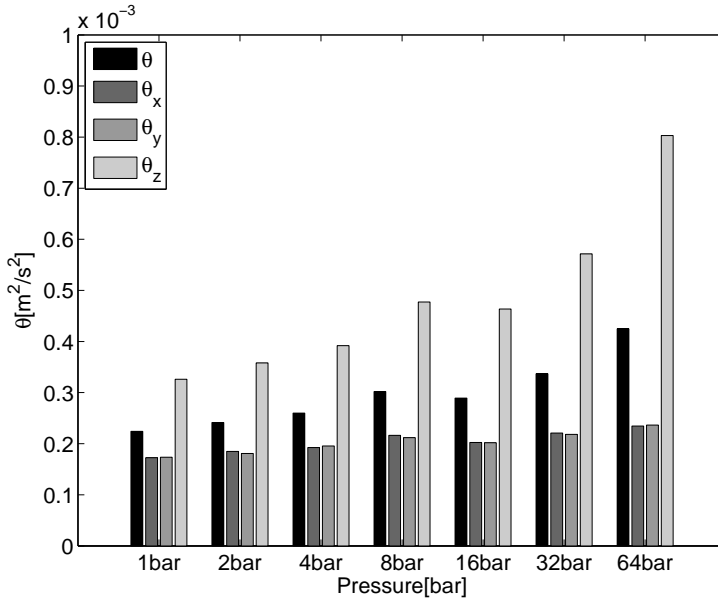


Figure 4.14: Granular temperature at different operating pressures in  $x$ ,  $y$  and  $z$  direction and for the total velocity.

pressure for the same porosities, we find that the pressure hardly affects the granular temperature, which will now be illustrated. We sorted all sampling data into porosity classes of  $\Delta\epsilon = 0.1$ , i.e. from 0.3 - 0.4, 0.4 - 0.5 etc. In Figure 4.15 the average granular temperature for each of the classes is shown. Up to porosities of 0.7 the effect of pressure on the granular temperature is very small. Above 0.7 some deviations appear. This implies that the operating pressure does not directly influence the granular temperature, but rather via the porosity, while for the bubble phase the granular temperature decreases with pressure. Note that at high porosities the sampling cells contain only few particles, which increases the uncertainties in the granular temperature calculation.

## 4.5 Conclusions

From seven full 3D DPM simulations at pressures ranging from 1 to 64 bar, using the same excess velocity, we found that the operating pressure influences the bed hydrodynamics significantly. The emul-

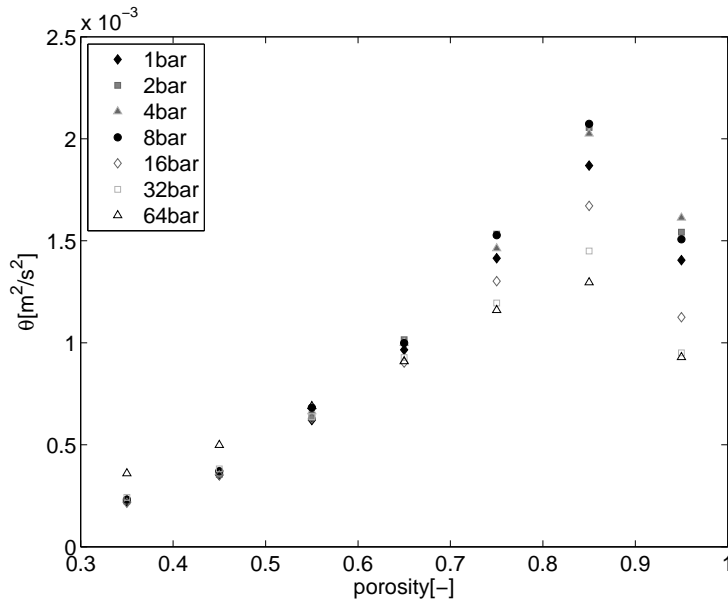


Figure 4.15: Porosity dependency of the granular temperature as a function of the operating pressure.

sion phase becomes less dense, and the distinction between bubbles and emulsion phase disappears. The applicability of the often used K-L model [Kunii and Levenspiel, 1991], which assumes separate bubble and emulsion phases, becomes less apparent at elevated pressures. Furthermore, it was found that the bubbles tend to become smaller as the pressure is increased. Finally, at an operating pressure of 2 bar the bubble rise velocity was found to be in very good agreement with the relation of Davidson and Harrison [1963]. At elevated pressures, the correspondence is less good. It was observed that the bubble passage frequency is increasing with increasing pressure, indicating that the bubbles are smaller as pressure is increased. This observation is confirmed by the results of a spectral analysis of the pressure drop fluctuations over the bed. From the DPM simulations we also obtained the granular temperature. The granular temperature increases with increasing operating pressure, which can be explained by the increased bed porosity. That is, at elevated pressures the bed is more porous and particles have more space to move randomly. The increase of granular temperature is mainly caused by the increased

porosity. If this effect is corrected for, we observed no pressure effect of operating pressure on the emulsion phase and a decreased granular temperature with increasing pressure for the bubble phase.

# 5

## Solids mixing in fluidized beds at elevated pressure

### 5.1 Introduction

Gas fluidized beds are widely used in industry in various large-scale processes involving physical and/or chemical operations. The large specific surface area of the solids in fluidized beds is beneficial for various operations, such as gas-solid reactions, cooling and drying. In many cases it is important that all particles are well mixed so that all particles cool, react or dry in a similar manner, to prevent hot spot formation or agglomeration. Solids mixing of granular materials is researched widely. Since solids mixing is difficult to characterize experimentally, have been employed discrete element models (DEM) or discrete particle models (DPM) to investigate solids mixing behaviour. McCarthy et al. [2000] succeeded to validate their simulations with experiments, which indicate that modeling is a promising approach to describe solids mixing in detail. In this work we investigate the capabilities of four different methods, previously proposed by Godlieb et al. [2007a,b], that can be used to calculate a mixing index from two-fluid model (TFM) simulations of fluidized beds. A mixing index ( $M$ ) is used to quantify the state of mixedness of the system and is zero or one for respectively fully demixed and fully mixed conditions. The mixing index is also known as entropy of mixing [Schutyser et al.,

2001], whereas Lu and Hsiau [2005] call it mixing degree, and Finnie et al. [2005], Asmar et al. [2002], Van Puyvelde [2006] call it mixing index. While most authors try to determine the mixing index from DEM simulations, they use different methods: Schutyser et al. [2001] calculated entropy based on entropy equations from molecular dynamics, whereas Mostoufi and Chaouki [2001] used the "colour" of a marked region (a spot) in the middle of the bed and measured the radius of the spot as a function of time. They were not able to calculate a mixing index. Lu and Hsiau [2005] and Rhodes et al. [2001] use the Lacey index as mixing index, which will be described later. Two-fluid models or Euler-Euler models usually employ the kinetic theory of granular flow (KTGF) to close the equations for the particulate phase. Gidaspow [1994] performed ground breaking work to derive the KTGF theory, which is the basis of this work. TFM models can be used to determine mixing by employing stating two particulate phases, as shown by Darelius et al. [2008]. In this work we use tracer particles that move with the interpolated velocity of the particulate phase. By using tracer particles, the same methods used for analyzing DPM results as done by Godlieb et al. [2007a,b] can be used to analyze mixing from TFM simulation data. This has the great advantage that the mixing is decoupled from the number of particle phases that are solved in the TFM. We test two new methods to quantify mixing: one based on the colouring of the twelve nearest neighbours and a method based on the increasing distance of initially neighboring particles. In this work we use the average height method and Lacey's method, as well as the two newly proposed methods to investigate solids mixing in a fluidized bed containing mono-disperse polymeric particles at different operating pressures. In the first part of this chapter the governing equations of the DPM and the TFM are presented, followed by the various methods to characterize solids mixing. Subsequently the results of the different methods applied to the simulation data are discussed and conclusions are presented.

## 5.2 Governing equations

The governing equations of the discrete particle model (DPM) and the two-fluid model (TFM) haven been presented in chapter 2. In this section an overview of the governing equations is presented.

### 5.2.1 Discrete particle model

The discrete particle model (DPM) belongs to the class of Euler-Lagrange models and was originally developed by Hoomans et al. [1996]. In the DPM every particle is individually tracked accounting for particle-particle and particle-wall collisions. The fluid phase is described by the volume-averaged conservation for mass and momentum respectively given by:

$$\frac{\partial}{\partial t} (\epsilon_f \rho_f) + \nabla \cdot (\epsilon_f \rho_f \bar{u}_f) = 0 \quad (5.1)$$

$$\frac{\partial}{\partial t} (\epsilon_f \rho_f \bar{u}_f) + \nabla \cdot (\epsilon_f \rho_f \bar{u}_f \bar{u}_f) = -\epsilon_f \nabla p - \nabla \cdot (\epsilon_f \bar{\tau}_f) - \bar{S}_p + \epsilon_f \rho_f \bar{g} \quad (5.2)$$

where  $\bar{u}_f$  represents the fluid velocity and  $\bar{\tau}_f$  the fluid phase stress tensor. The sink term  $\bar{S}_p$ , represents the drag force exerted on the particles:

$$\bar{S}_p = \frac{1}{V_{cell}} \int_{V_{cell}} \sum_{i=0}^{N_{part}} \frac{V_i \beta}{1 - \epsilon_f} (\bar{u}_f - \bar{v}_i) D(\bar{r} - \bar{r}_i) dV \quad (5.3)$$

The distribution function  $D(\bar{r} - \bar{r}_i)$  is a discrete representation of a Dirac delta function that distributes the reaction force acting on the gas to the Eulerian grid via a volume-weighting technique. The inter-phase momentum transfer coefficient,  $\beta$  describes the drag of the gas-phase acting on the particles.

The Ergun [1952] and Wen and Yu [1966] equations are commonly used to obtain expressions for  $\beta$ . However, we use the closure relation proposed by Koch and Hill [2001] obtained from on lattice Boltzmann simulations, since it has no discontinuities at high Reynolds numbers and gives good results as reported by Bokkers et al. [2004] and Link et al. [2005].

The particle dynamics are described by Newton's second law:

$$m_i \frac{d\bar{v}_i}{dt} = -V_i \nabla p + \frac{V_i \beta}{\epsilon_s} (\bar{u} - \bar{v}_i) + m_i \bar{g} + F_i^{pp} + F_i^{pw} \quad (5.4)$$

where the forces on the right hand side are, respectively due to pressure, drag, gravity, particle-particle interaction and particle-wall interaction. For the rotational motion the angular momentum equation is used:



$$\bar{I}_i \frac{d\bar{\omega}_i}{dt} = \bar{T}_i \quad (5.5)$$

where the moment of inertia is defined as:

$$I_i = \frac{2}{5} m_i r_i^2 \quad (5.6)$$

The contact forces are caused by collisions with other particles or confining walls. These collisions are described with a soft-sphere approach. This approach uses a linear spring/dash-pot model, wherein the velocities, positions and collision forces of the particles are calculated at every fixed time step via a first order time integration [Hoomans et al., 1996]. The collision model takes restitution and friction effects into account. The associated collision coefficients were obtained experimentally via the method of Kharaz et al. [1999]. They developed a sophisticated experimental method to obtain collision parameters for different impact angles. For a more detailed discussion of this model we refer to Van der Hoef et al. [2006].

## 5.2.2 Two-fluid model

In the two-fluid model (TFM) both the fluid and solids phase are described as continuous inter-penetrating fluids. The mass and momentum equations for the fluid are given by:

$$\frac{\partial}{\partial t}(\epsilon_f \rho_f) + \nabla \cdot (\epsilon_f \rho_f \bar{u}_f) = 0 \quad (5.7)$$

$$\frac{\partial}{\partial t}(\epsilon_f \rho_f \bar{u}_f) + \nabla \cdot (\epsilon_f \rho_f \bar{u}_f \bar{u}_f) = -\epsilon_f \nabla p_f - \nabla \cdot (\epsilon_f \bar{\tau}_f) - \beta(\bar{u}_f - \bar{u}_s) + \epsilon_f \rho_f \bar{g} \quad (5.8)$$

whereas the corresponding equations for the solids phase are given by:

$$\frac{\partial}{\partial t}(\epsilon_s \rho_s) + \nabla \cdot (\epsilon_s \rho_s \bar{u}_s) = 0 \quad (5.9)$$

$$\frac{\partial}{\partial t}(\epsilon_s \rho_s \bar{u}_s) + \nabla \cdot (\epsilon_s \rho_s \bar{u}_s \bar{u}_s) = -\epsilon_s \nabla p_f - \nabla p_s - \nabla \cdot (\epsilon_s \bar{\tau}_s) + \beta(\bar{u}_f - \bar{u}_s) + \epsilon_s \rho_s \bar{g} \quad (5.10)$$

The inter-phase momentum transfer is modeled by:

$$\bar{S}_p = \beta(\bar{u}_f - \bar{u}_s) \quad (5.11)$$

where the  $\beta$  represent inter-phase momentum transfer coefficient, which is modeled with the relation proposed by Van der Hoef et al. [2005]:

$$\beta = 18 \frac{\mu_f}{d^2} \left( 10 \frac{\epsilon_s^2}{\epsilon_f} + \epsilon_f^3 \epsilon_s (1 + 1.5\sqrt{\epsilon_s}) \right) \quad (5.12)$$

For the description of the solids phase the kinetic theory of granular flow (KTGF) is used. This theory was initially developed by Gidaspow (1994) for multiphase systems involving particles. In addition to the continuity and the Navier-Stokes equations the granular temperature equation is solved for the particulate phase. The overall granular temperature is defined as:

$$\Theta = \frac{1}{3} \langle \bar{C}_p \cdot \bar{C}_p \rangle \quad (5.13)$$

where:

$$\bar{c}_p = \bar{u}_s + \bar{C}_p \quad (5.14)$$

Note that the particle velocity ( $\bar{c}_p$ ) is decomposed in the local mean velocity ( $\bar{v}$ ) and the fluctuation velocity component ( $\bar{C}_p$ ).

The granular temperature is governed by the following equation:

$$\frac{3}{2} \left[ \frac{\partial}{\partial t} (\epsilon_s \rho_s \Theta + \epsilon_s \rho_s \Theta \bar{u}_s) \right] = -(P_s \bar{I} + \epsilon_s \bar{I}_s) : \nabla \bar{u}_s - \nabla \cdot (\epsilon_s q_s) - 3\beta\Theta - \gamma \quad (5.15)$$

The KTGF closure equations that were used in this work can be found in chapter 2. For details on the numerical implementation we refer to the work of Goldschmidt et al. [2001].

### 5.2.3 Tracer particles in TFM

To investigate mixing in the TFM one could define multiple solids phases with the same properties, but with different colours. Drawbacks of this approach are grid dependency, initial colouring dependency and the inability to investigate sub grid mixing. An attractive

alternative to the use of multiple solids phases is the use of tracer particles. As the motion of the solids phase is visualized by tracer particles, the same methods for characterizing mixing as used in discrete particle models can be applied. By definition tracer particles have no mass and follow the solids motion exactly. The velocity of the tracer particles is interpolated from the solids phase velocity as follows:

$$\bar{v}_p = D(\bar{x} - \bar{x}_p)\bar{v}_s \quad (5.16)$$

In this work we use volume-weighting (i.e. tri-linear interpolation) for the interpolation:

$$D(\bar{x} - \bar{x}_p) = \prod_i D(\bar{x}_i - \bar{x}_{p,i}) \quad (5.17)$$

where

$$D(\bar{x}_i - \bar{x}_{p,i}) \begin{cases} 1 - \delta_i & \text{if } \delta_i \leq 1 \\ 0 & \text{if } \delta_i > 1 \end{cases} \quad (5.18)$$

and

$$\delta_i = \frac{|x_i - x_{p,i}|}{\Delta x_i} \quad (5.19)$$

where  $\delta_i$  is the dimensionless distance between the Eulerian position  $x_i$  and the Lagrangian position of the tracer particle  $x_{p,i}$  in the  $x_i$  direction.

## 5.3 Methods for characterizing mixing

In this work we use five different methods to obtain mixing indices from simulation data for systems with mono disperse particles. In this section each of these methods will be discussed in detail. These methods were initially designed for DPM results, but are applicable to TFM tracer particles as well.

### 5.3.1 Average height method

The average height method is the simplest of the investigated methods and is based on the average height of a group of coloured particles.

It is widely used for measuring segregation, for example by Hoomans et al. [2000]. In the case of mono disperse systems, half of the particles are given a colour while all physical properties remain unchanged and constant throughout the set of particles. In this method the average position of all particles is monitored. While the mixing behaviour can in principle be investigated in all three directions, here we will only focus on mixing in the vertical direction. In the first step of the algorithm the vertical positions of all particles are sorted to determine the median height. Subsequently the lower half of the particles is coloured white, while the upper half is coloured black. For each time step the average height of the white particles can be calculated and normalised with the average height of all particles:

$$\bar{z}_{white} = \frac{\frac{1}{N_{white}} \sum_{i \in white} z_i}{\frac{1}{N_{all}} \sum_{i \in all} z_i} \quad (5.20)$$

where  $\bar{z}_{white}$  is the normalised average vertical position of the white particles. Notice that initially  $\bar{z}_{white}$  is 0.5 and when the system fully mixed it becomes 1.0. We now define the mixing index as follows:

$$M = 2(\bar{z}_{white} - 0.5) \quad (5.21)$$

which means that for  $M = 0$  the system is fully demixed and for  $M = 1$  the bed is fully mixed. This method can also be used in the  $x$  and  $y$  direction. In those cases the left and right or bottom and top parts, are respectively coloured white and black.

### 5.3.2 Lacey's method

The Lacey index is based on statistical analysis and was developed by Lacey [1954]. The variance  $S^2$  for the concentration of the black particles in each cell is defined as follows:

$$S^2 = \frac{1}{N-1} \sum_{i=1}^N (\phi_i - \phi_m)^2 \quad (5.22)$$

where  $N$  is the number of cells in the bed containing particles and  $\phi_i$  the concentration of black particles in cell  $i$  and  $\phi_m$  the average concentration of black particles in the bed.  $S_0^2$  and  $S_R^2$  are defined as:

$$S_0^2 = \phi_m(1 - \phi_m) \quad (5.23)$$

$$S_R^2 = \frac{\phi_m(1 - \phi_m)}{n} \quad (5.24)$$

and respectively represent the variance of the unmixed bed and fully mixed bed. Where  $n$  is the average number of particles per cell. The mixing index can be calculated as follows:

$$M = \frac{S^2 - S_0^2}{S_R^2 - S_0^2} \quad (5.25)$$

Due to the use of grid cells the Lacey index is grid dependent. A coarse grid gives higher mixing indices, since in that case the micro mixing effects are neglected. A fine grid gives lower mixing indices, if only few particles are present per cell. If only one particle is present per cell it is always fully unmixed.

### 5.3.3 Nearest neighbours method

Contrary to the average height method in which the overall average height of the particles is monitored, in the nearest neighbours method we evaluate the mixing in the vicinity of individual particles. Opposite to the Lacey index, it is grid independent. Initially we colour half of the particles black, similar to what is done in the average height method. For each particle we determine the twelve nearest neighbouring particles. If these particles have the same colour as the particle under investigation it is unmixed, while if half of the nearest neighbours is coloured differently, it is fully mixed. This is expressed as follows:

$$M = \frac{1}{N_{part}} \sum_{N_{part}} \frac{2n_{diff}}{n_{nb}} \quad (5.26)$$

where  $n_{diff}$  is the number of nearest neighbours coloured differently. In Figure 5.1 shows an example for one individual particle, for which four neighbouring particles have a different colour (white). The mixing index for that specific particle is  $\frac{2 \cdot 4}{12} = 0.67$ . The overall mixing index is the average over all particles.

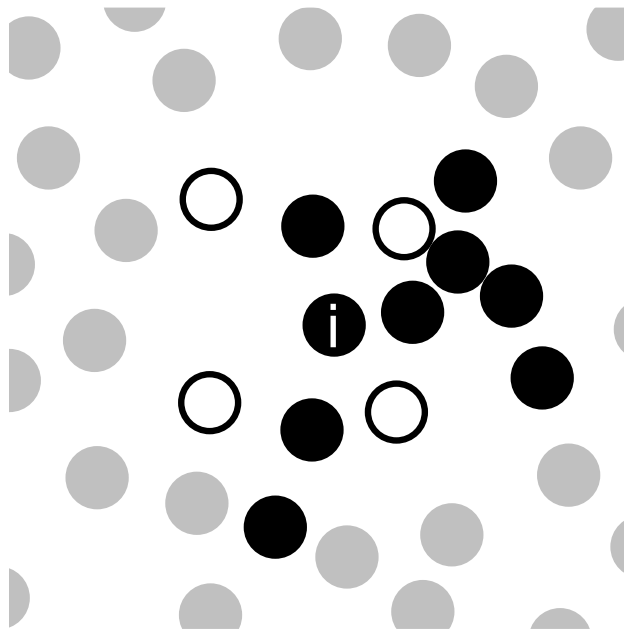


Figure 5.1: Illustration of the nearest neighbours method. For the highlighted particle (i) the twelve nearest neighbours are shown. Four of them are white and eight are coloured black. Particles that are located further away are coloured grey and are not taken into account for this particle.

### 5.3.4 Neighbour distance method

The fourth method used in this work is based on the distance between initial neighbours. At a given time for each particle its nearest neighbour is located. Each particle and its nearest neighbour form a pair, and its centre to centre distance is monitored as time progresses. Initially the distance is the order of one particle diameter and if the bed is fully mixed it can increase up to the bed dimensions. Figure 5.2 shows the average distance between initial neighbours normalised with the particle diameter. Initially it is just above one particle diameter and after 1 second it is increased up to 60. It is not a smooth curve, because bubbles let the bed expand and collapse, causing the distance between particles to increase and decrease with time. This effect introduces noise on the mixing measurement. Therefore the distance is normalised with the distance of randomly selected particle pairs, resulting in a smooth mixing curve, unaffected by bed expansions as seen in Figure 5.3. Since initially the distance between neighbours is one particle diameter this is set to a mixing index of 0. The mixing index is expressed in the following equation:

$$M = \frac{\sum_{i=0}^N r_{ij} - d_p}{\sum_{i=0}^N r_{ik} - d_p} \quad (5.27)$$

where  $r_{ij}$  is the distance between particle  $i$  and its initially nearest neighbour  $j$  and  $r_{ik}$  is the distance between particle  $i$  and a randomly selected particle  $k$ . The method just described can also be used to calculate the mixing index for each direction. In that case, the same initial partner is used. Initially the distance between the partners in one direction can be less than a diameter, as can be seen in Figure 5.4. Some basic algebra shows that the average distance in one direction for two touching particles is  $d_0 = \frac{4d_p}{\pi^2}$ .

The mixing index in the vertical direction for the Neighbour distance method is thus defined by:

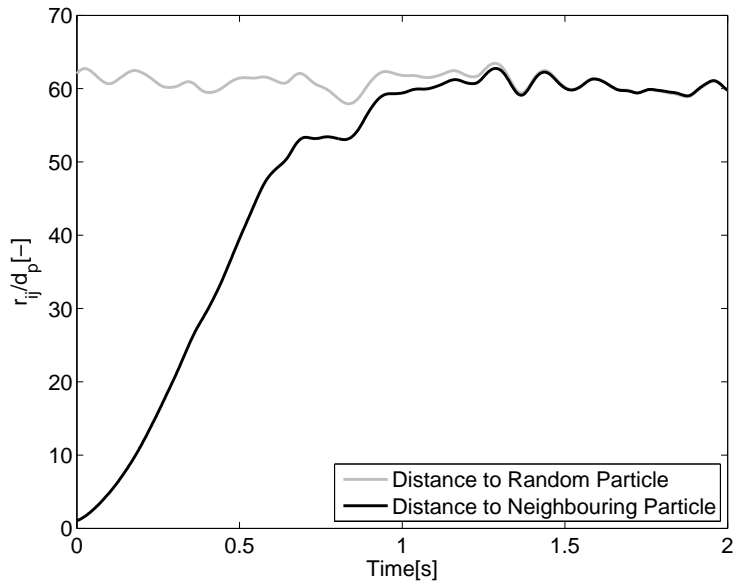


Figure 5.2: Distance between initial nearest neighbours averaged over all pairs (black line) and average distance between random particles (grey line).

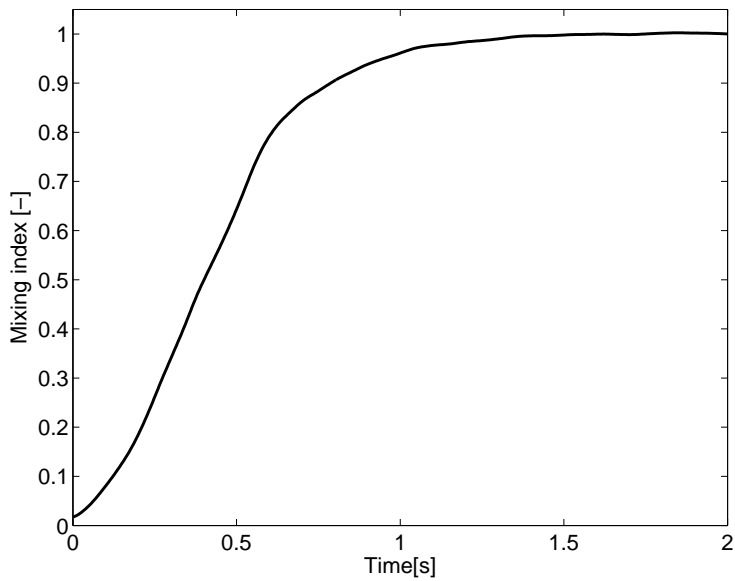


Figure 5.3: Mixing index determined with the neighbour distance method, calculated with the data from figure 5.2.



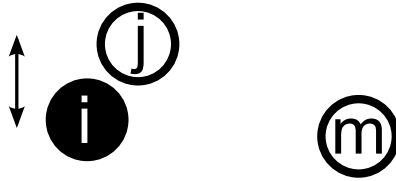


Figure 5.4: Mixing index determined with the neighbour distance method for the  $z$ -direction. Particle  $j$  is the closest partner for the highlighted particle  $i$ . Particle  $m$  has the least distance in the  $z$ -direction, but is not used as closest initial partner.

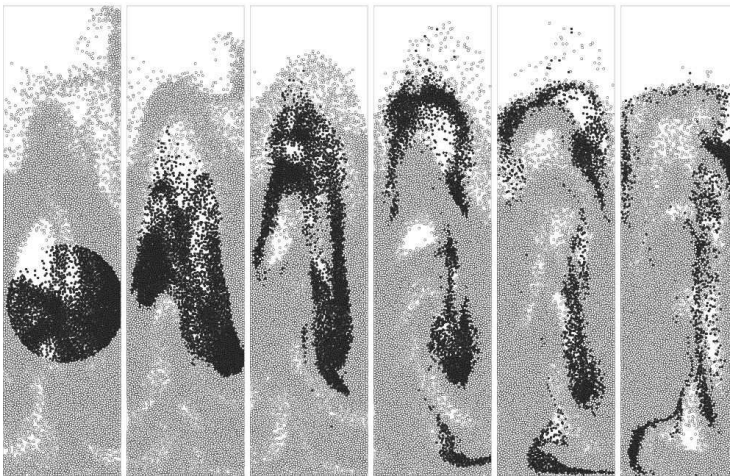


Figure 5.5: A slice in the middle of the fluidized bed is shown. Initially a sphere of particles is coloured black (left). After 0.2 seconds the sphere is spread over the bed (right)

$$M_z = \frac{\sum_{i=0}^N r_{ij,z} - d_0}{N} \quad (5.28)$$

$$\sum_{i=0}^N r_{ik,z} - d_0$$

The mixing index for the horizontal direction can be obtained by replacing subscript  $z$  by  $x$  or  $y$ .

### 5.3.5 Sphere spreading method

In their DPM simulations of a fluidized bed, Mostoufi and Chaouki [2001] coloured a box in the middle of the bed and monitored the spreading of the coloured particles. In this work we used a similar method and calculated a mixing index from the spreading of the coloured particles. Contrary to the work of Mostoufi and Chaouki [2001], we coloured a sphere, with a radius of the width of the bed, as shown in Figure 5.5.

The spreading of the black particles is characterised by:

$$R = \frac{1}{N_{black}} \sum_{i \in black} r_i \quad (5.29)$$

where  $r_i$  is the distance of particle  $i$  to the centre of mass of the set of black particles. Note that only the black particles are considered in this summation. The mixing index can be calculated using the initial distance of the black particles  $R_0$  and the average distance of all particles  $R_A$ .

$$M = \frac{R - R_0}{R_A - R_0} \quad (5.30)$$

where:

$$R_A = \frac{1}{N_{part}} \sum_{i=1}^{N_{part}} r_i \quad (5.31)$$

### 5.3.6 Calculation of the mixing time

The mixing index is a valuable tool to investigate the solids mixing process in fluidized beds. To compare different simulations in a simple way, the mixing index curve is condensed in a single value. We choose to use the 95% mixing time  $t_{95\%}$ . To prevent noise to influence the results, we fit a dampened exponential function to fit the mixing index curve as follows:

$$M_{fit} = 1 - Ae^{-\gamma t} \quad (5.32)$$

where  $A$  and  $\gamma$ , are the amplitude and the damping coefficient respectively. Each of these coefficients is obtained from the simulation data using a least squares method. The fit as shown in Figure 5.8 accurately follows the trend of the curve. From this fit we can calculate the mixing time at which the bed is 95% mixed, by solving equation 5.32 for  $t$ :

$$t_{95\%} = \frac{-1}{\gamma} \ln \left( \frac{1 - 0.95}{A} \right) \quad (5.33)$$

Unfortunately the average height method and sphere spreading method show periodic overshoots. This effect is caused by the circulation patterns of the particles in the bed, as can be seen in Figure 5.6 and Figure 5.7, which shows the mixing index obtained for the average height method. Although  $M = 1$  at 0.17 seconds the bed is not fully mixed. At 0.31 seconds the colour pattern has been more or less inverted due to the bed circulation patterns, leading to an overshoot of  $M = 1.6$ . Eventually, after about 1.8 seconds the overshoots have dampened out and the bed is almost entirely mixed.

Since the mixing index is oscillating around a value of 1, it is hard to determine a mixing time; therefore the curve is fitted with a dampened harmonic oscillator:

$$M_{fit} = 1 - Ae^{-\gamma t} \cos(\omega t) \quad (5.34)$$

where  $\omega$  is the period of the oscillation. Now we can calculate the 95% mixing time using the fit without the oscillator. By removing the periodic part from the fitted equation we obtain an expression similar to equation 5.32 from which a 95% mixing time can straightforwardly be obtained.

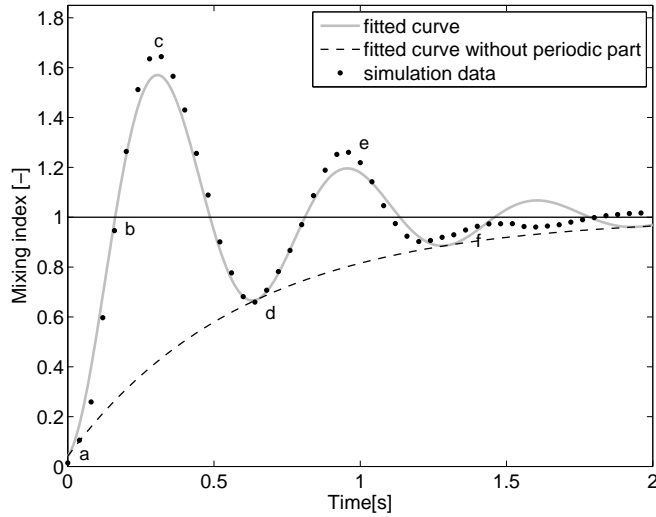


Figure 5.6: Mixing index versus time, results from simulation( $\cdot$ ), a fit of the data using equation 5.34 ( $—$ ) and equations 5.32 ( $- -$ ). Images corresponding to the letters  $a$  through  $f$  are shown in figure 5.7

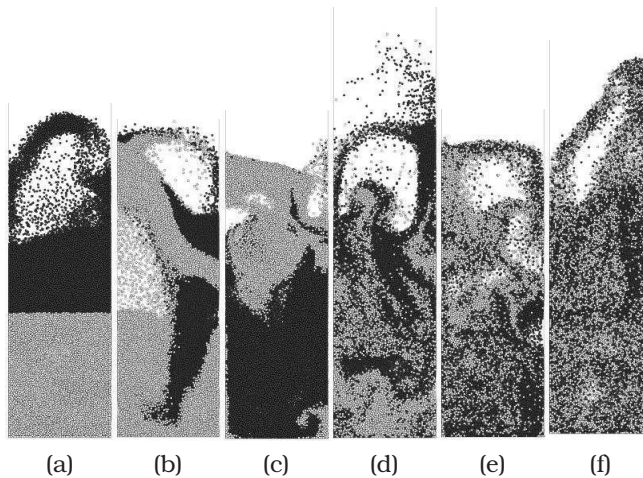


Figure 5.7: Images of a slice in the centre of the bed are shown, corresponding to the letters  $a$  through  $f$  of Figure 5.6

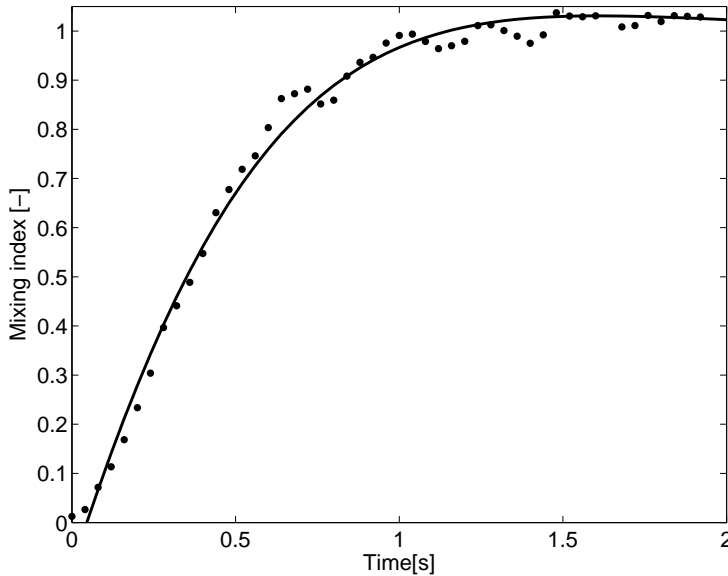


Figure 5.8: Lacey index fitted with a damped exponential function.

Especially for the neighbour distance method the exponential function does not fit very well (see Figure 5.9). A function proposed by Gompertz [1825] (equation 5.35), originally designed for modelling mortality and the prediction of tumor growth, does fit much better, since mixing is initially slow, increases further and reaches a maximum:

$$M_{fit} = ae^{be^{-ct}} \quad (5.35)$$

where  $a$  is set to 1 and  $b$  and  $c$  are two fit parameters.

From this fit we can calculate the mixing time at which the bed is 95% mixed, by solving equation 5.35 for  $t$ :

$$t_{95\%} = \frac{\ln \frac{\ln 0.95}{b}}{-c} \quad (5.36)$$

In Table 5.1 an overview of the fit functions for all five mixing characterization methods is shown.

To show the reproducibility for all methods and additionally to obtain an error margin, for each simulation the mixing indices are calculated for several parts of the simulation. For each simulation

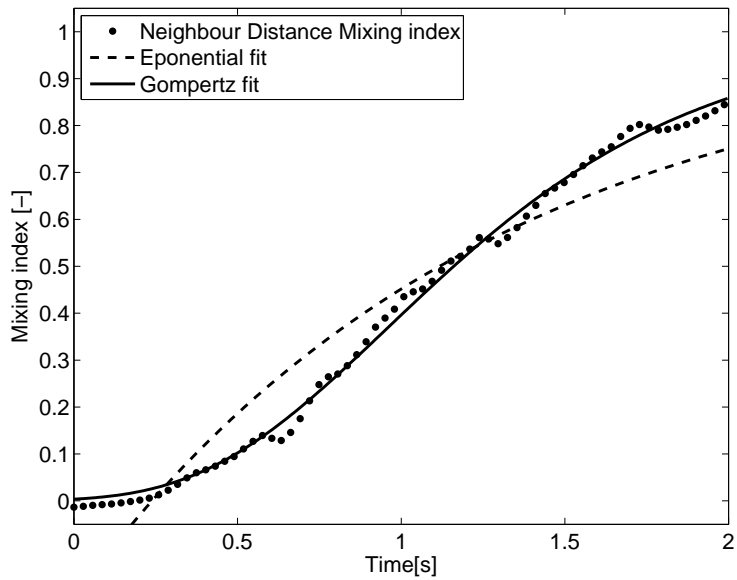


Figure 5.9: Vertical mixing index for neighbour distance method at 1 bar (TFM). The exponential fit (equation 5.32) and the Gompertz fit (equation 5.35) are shown.

Table 5.1: Used fit functions for all mixing characterizing methods

method	fit function	equation
Average Height	Dampened harmonic oscillator	$M_{fit} = 1 - (Ae^{-\gamma t} \cos(\omega t))$
Nearest Neighbours	Dampened exponential function	$M_{fit} = 1 - Ae^{-\gamma t}$
Lacey's index	Dampened exponential function	$M_{fit} = 1 - Ae^{-\gamma t}$
Neighbour Distance	Gompertz	$M_{fit} = e^{be^{-ct}}$
Sphere Spreading	Dampened exponential function	$M_{fit} = 1 - Ae^{-\gamma t}$

Table 5.2: Superficial gas velocities for all seven simulations.

P(bar)	$u_{mf}$ (m/s)	$u_{sup}$ (m/s)
1	0.088	0.265
2	0.084	0.261
4	0.077	0.253
8	0.067	0.244
16	0.056	0.233
32	0.044	0.221
64	0.033	0.210

the first second is not taken into account since startup effect are still present. The rest of the simulation is cut into 8 periods of 2 seconds starting each second: 1-3 seconds, 2-4 seconds, 3-5 seconds, etc. The error margins shown in the figures in the next section are the standard deviation of the mixing indices obtained for those periods.

## 5.4 Simulation settings

To investigate the pressure effect on the fluidization behaviour seven full 3D DPM simulations and seven 2D TFM simulations at 1, 2, 4, 8, 16, 32 and 64 bar were performed.

In order to enable a fair comparison between the simulations, a constant excess velocity (i.e. superficial gas velocity minus minimum fluidization velocity) of 0.177 m/s was applied (see Table 5.2).

### DPM Simulations

The system properties and operating conditions for the DPM simulations are specified in Table 5.3.

No-slip boundary conditions were used at the walls. For high pressures the height of the bed was extended to prevent particle carry over.

Table 5.3: Settings for all seven DPM simulations.

Property	Symbol	Value	Unit	
system width	$X$	0.025	$m$	(20 cells)
system depth	$Y$	0.025	$m$	(20 cells)
system height	$Z$	0.1	$m$	(80 cells)
time step	$dt$	$1.0 \cdot 10^{-4}$	$s$	
total time	$t$	10	$s$	
number of particles	$N_{part}$	$2.86 \cdot 10^5$	-	
particle diameter	$d_p$	0.5	$mm$	
normal spring stiffness	$k_n$	200	$N/m$	
coefficient of normal restitution	$e_n$	0.8	-	
coefficient of tangential restitution	$e_t$	0.6	-	
particle density	$\rho$	925	$kg/m^3$	
friction coefficient	$\mu$	0.1	-	

Table 5.4: Settings for all seven TFM simulations.

Property	Symbol	Value	Unit	
system width	$X$	0.025	$m$	(20 cells)
system depth	$Y$	0.003	$m$	(1 cell)
system height	$Z$	0.1	$m$	(80 cells)
time step	$dt$	$2.0 \cdot 10^{-5}$	$s$	
total time	$t$	12	$s$	
particle diameter	$d_p$	0.5	$mm$	
coefficient of restitution	$e_n$	0.8	-	
particle density	$\rho$	925	$kg/m^3$	

## TFM Simulations

In the TFM simulations, no-slip conditions are applied for the gas phase at the walls and partial slip was used for the particles. For the bottom a prescribed influx is set and at the top a prescribed pressure is imposed. For high pressures the height of the bed was extended to prevent particle carry over.  $5 \times 5$  tracer particles were initially set in each cell containing particles, which makes a total of 20,000 tracer particles.

## 5.5 DPM results

In this section we will discuss five methods used to calculate the mixing index, anisotropic behaviour and the influence of operating pressure on the mixing process.



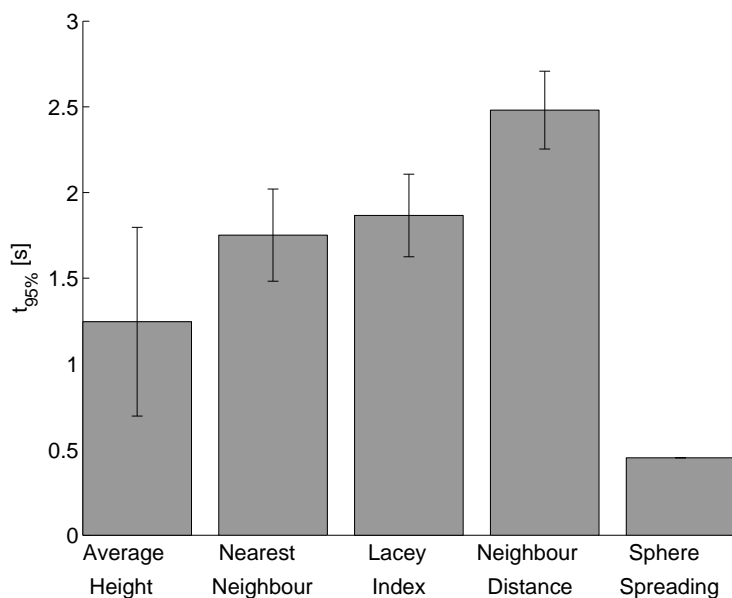


Figure 5.10: The 95% mixing time for all five methods for the simulation at 1 bar operating pressure. (Initially the top half of the particles were coloured black). The shown error margins are twice the standard deviation in the eight individual calculations of the 95% mixing time.

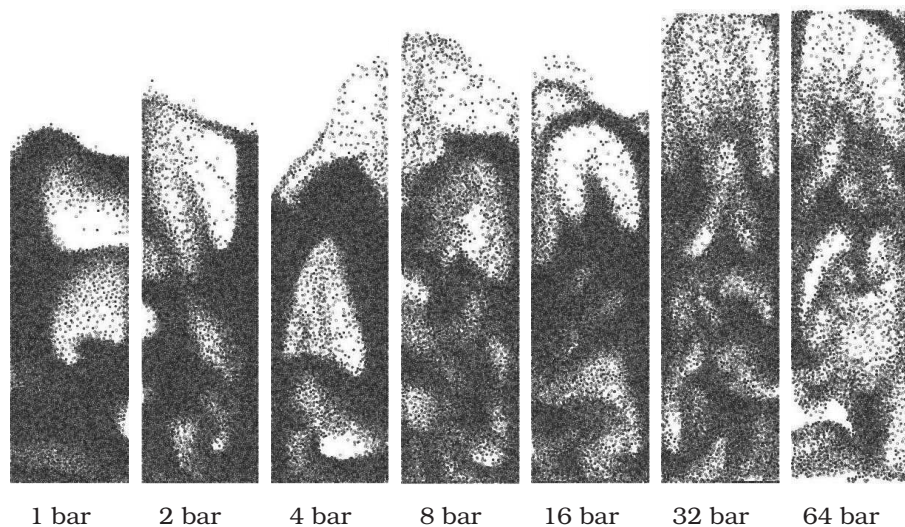


Figure 5.11: Snapshots of particle positions in a slice in the centre of the bed with a depth of one numerical grid cell at different operating pressures.

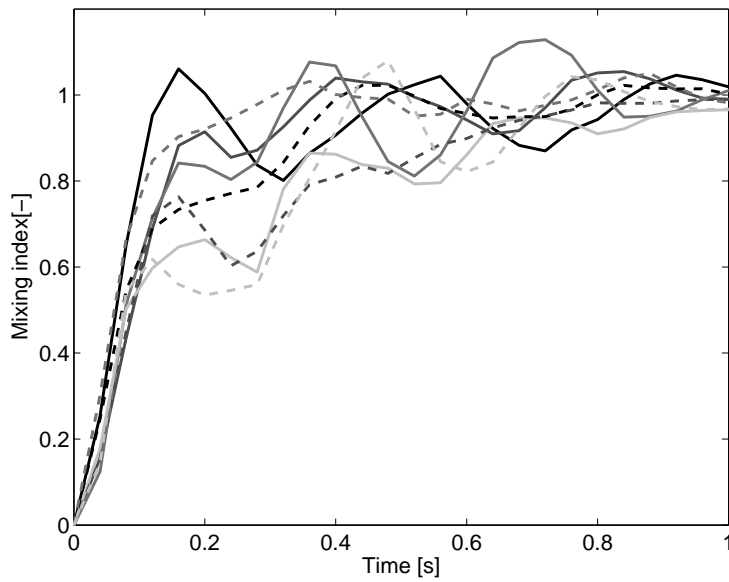


Figure 5.12: The mixing index calculated with the sphere radius method for 8 parts of the simulation at an operating pressure of 8 bar. The results are not reproducible.

The five different mixing methods give different results for the  $t_{95\%}$ , due to differences in the definitions of a mixed system. We find that the sphere spreading methods is less suited for the description of mixing in fluidized beds. The main reason is that it presumes a diffusive mixing behaviour, whereas the transport of particles in a fluidized bed is predominantly of a convective nature. As a result, the mixing index signal shows strong periodicity as the particles are circulated through the bed, as can be seen in Figure 5.12. The resulting signal cannot be described by a simple fit, which makes it impossible to determine an accurate mixing time. The average height method is simple and effective, but due to the macroscopic flow pattern the colour pattern inverts resulting in a mixing index larger than 1, as shown in Figure 5.6. This disadvantage complicates the data analysis of the method. Furthermore, the method cannot be used to analyse the micro mixing effect at the scale of individual particles, as it only takes macroscopic mixing into account. As a result the calculated 95% mixing time is lower compared to the other methods. The Lacey index and the nearest neighbours method produce similar results for all simulations. Both methods have a similar approach where the colouring of the neighbouring particles is taken into account. For the Lacey index we used  $25 \times 25 \times 100$  cells, so the average number of particles per cell was about twelve, which is similar to the number of neighbours taken into account in the nearest neighbours methods. The main advantage of the nearest neighbours method is its grid independency, although the method is dependent on the number of neighbours taken into account. The initial neighbour method gives slightly longer mixing times, but the same trend with pressure is found as for the nearest neighbours and Lacey's method, as is shown in Figure 5.13. The main advantage of this method is that no grid is used in the calculation. Moreover, the method is not dependent on initial colouring. All other methods discussed are based on initial colouring of particles, which influences the results. Twice the standard deviation of eight individual calculations is shown as error margins in Figure 5.10 and Figure 5.13. The error margins for the initial neighbour method are 12% on average which is much lower compared to the Lacey index (20%), nearest neighbours (20%) and the average height (40%) method.

Pressure influences the mixing behaviour significantly. This is confirmed by the results shown in Figure 5.13. The increased num-

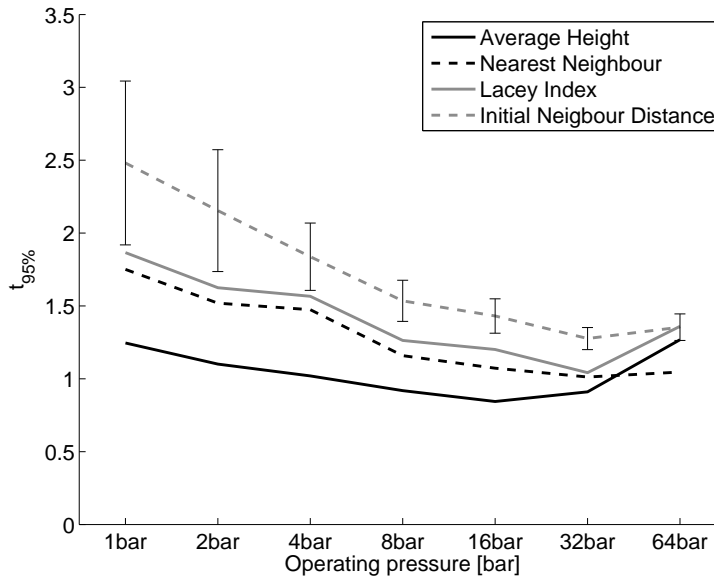


Figure 5.13: Mixing times versus operating pressure for vertical mixing from DPM simulation. For the initial neighbour distance method the error margins are shown.

ber of bubbles, with more chaotic movement at elevated pressure, improves mixing. In Figure 5.11 it can be seen that at 64 bar the regime has changed from a bubbling regime to a more homogeneous regime. In that sense the case for 64 bar deviates from the trend in the mixing time. Figure 5.14 shows the anisotropy of the mixing resulting from the four methods. The average height methods and the initial neighbour distance show a slightly larger mixing time in the vertical ( $z$ ) direction, since in these methods the size of the bed is taken into account and the height of the bed is significant larger than the width and depth. We would expect anisotropic mixing, because the bubbles and gas moves in the vertical direction. However, our system appears to be too small to exhibit pronounced anisotropic effects.

## 5.6 TFM results

The TFM can model larger systems than the DPM, so it is of importance to also investigate mixing in TFM simulations. In this work we used a rather small 2D TFM simulation, but we were still able to

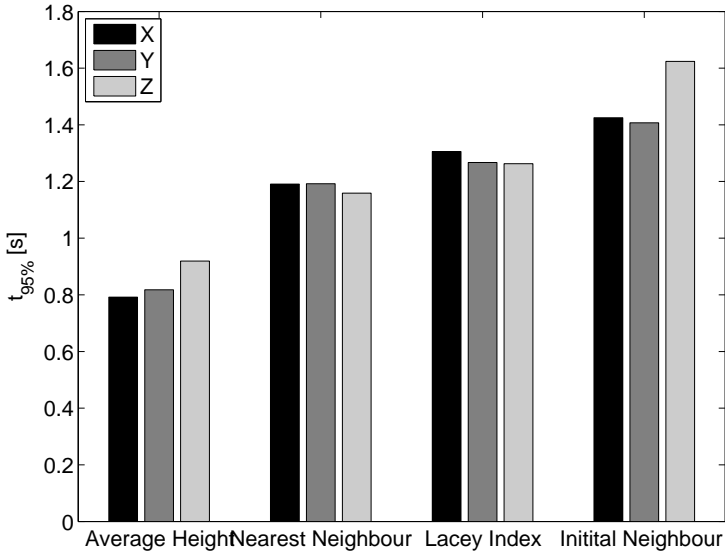


Figure 5.14: Mixing time for four mixing methods in vertical ( $z$ ) and horizontal ( $x$  and  $y$ ) directions for the simulation at 8 bar.

Table 5.5: (Dis)advantages of five methods for determining the mixing index.

	<b>Reproducibility</b>	<b>Grid independency</b>	<b>Colour independency</b>	<b>In all directions</b>
Average height	+	+	-	+
Nearest neighbours	+	+	-	+
Lacey index	+	-	-	+
Initial neighbour distance	++	+	+	+
Sphere radius	-	+	-	-

show the influence of pressure on the mixing behaviour of the system. The width and height dimensions are chosen the same as in the DPM simulations to make them mutually comparable.

The results of the vertical and horizontal mixing times are shown in Figures 5.15 and 5.16. It is found that the obtained trends show strong similarities with the DPM results discussed in the previous section (see Figure 5.13). Mixing times reduce with increasing operating pressure. This phenomenon is due to the presence of an increased number of bubbles, which yields more chaotic particle movement at elevated pressure, hence improved solids mixing. A deviation from this trend is noticed at higher pressures (especially 32 and 64 bar). This can be explained by analyzing snapshots of the particle positions (see Figures 5.17 and 5.18).

At a pressure of 64 bar, the bed tends to expand to almost twice the height at 2 bar. This has a large influence on mixing times, since the particles need to travel longer distances. The snapshots show that it takes more time for the bottom tracer particles to reach the top of the bed and hence, to fully mix. To assess the mixing irrespective of the bed expansion, we also analyzed the results for horizontal mixing. Since the horizontal pathway of the particles is bound by the confining walls, bed expansion should have little effect on horizontal mixing. The results in Figure 5.16 confirm this idea: the horizontal mixing times decrease at high pressure.

For vertical mixing, increasing pressure has the effect that i) the number of bubbles increases and chaotic movement in the bed *enhances* (micro) mixing, and ii) the bed expansion increases the particle traveling distances and hence *decreases* (macro) mixing. The first effect is dominant in the range of 1-8 bars, whereas the second effect is most important at high pressures. However, the results of the horizontal mixing do not show a smooth trend of decreasing mixing time at low pressures. After studying particle position snapshots, it is concluded that bed expansion has an important effect on horizontal mixing after all, especially at lower pressures. This can be explained as follows. The average solids motion takes the form of two counter-rotating vortices (see Figure 5.19). Horizontal motion is only dominant in the top and the bottom zones of the bed. It is in these zones that the mixing of coloured particles starts (see Figure 5.20). Because mixing mostly happens at the top and bottom of the bed, the (expanded) bed height can influence horizontal mixing as well. Extra

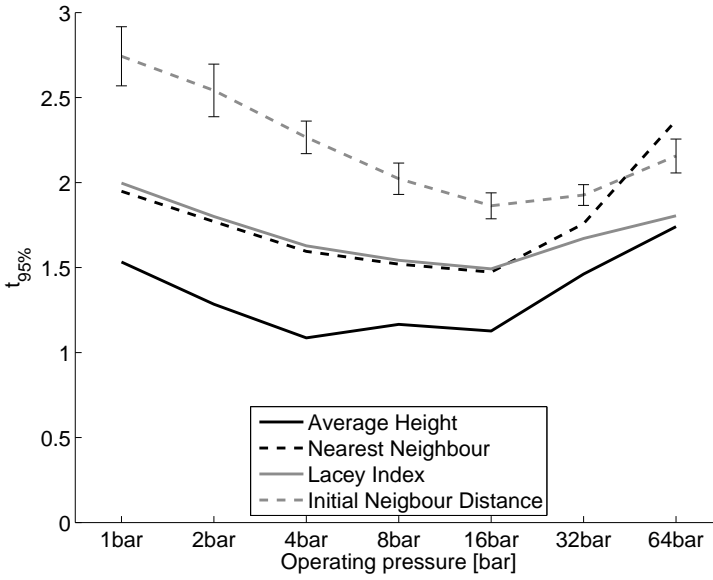


Figure 5.15: Mixing times versus operating pressure for vertical mixing from TFM simulation.

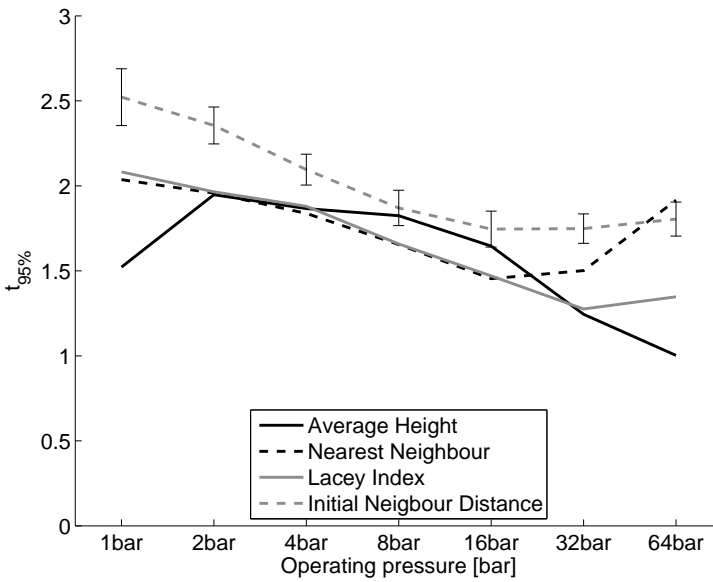


Figure 5.16: Mixing times versus operating pressure for horizontal mixing (bottom) from TFM simulation.

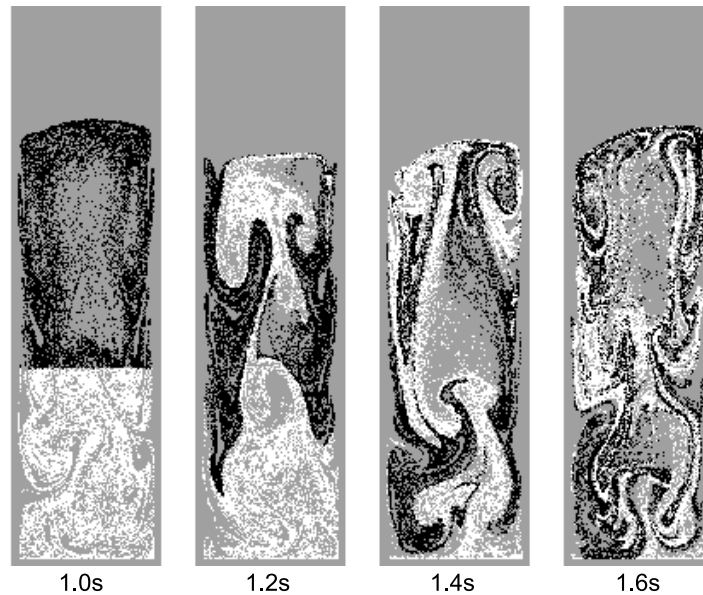


Figure 5.17: Snapshots of vertical mixing at 2 bar.

simulations were performed to test the influence of bed height on the mixing times for vertical and horizontal mixing. For 2 and 32 bar, the initial bed height was reduced by 35%. Then again, mixing times were calculated. An average mixing time was determined by averaging the four mixing indices. The results from these simulations are listed in Table 5.6 and show that reducing the bed height has similar effects for 2 and 32 bar on the vertical mixing time. Both are reduced with 11%. For horizontal mixing however, results are different, i.e. the mixing time is less influenced compared to the vertical direction (only 6% reduction) for 32 bar, but reduced significantly for 2 bar (16%). This implies that i) horizontal mixing occurs partially via rotational movement of particles in the bed decreasing the mixing when a fluidized bed expands due to increasing pressure and ii) both direct horizontal motion increases the mixing with increasing pressure, due to more chaotic movement in the bed and increased expansion of the emulsion phase. For high pressures, the second effect is dominant and therefore, horizontal mixing times are not so much affected by bed height as for lower pressures.

Pressure influences the hydrodynamics significantly as can be seen in Figure 5.21, which shows the PDF of the porosity. For pres-



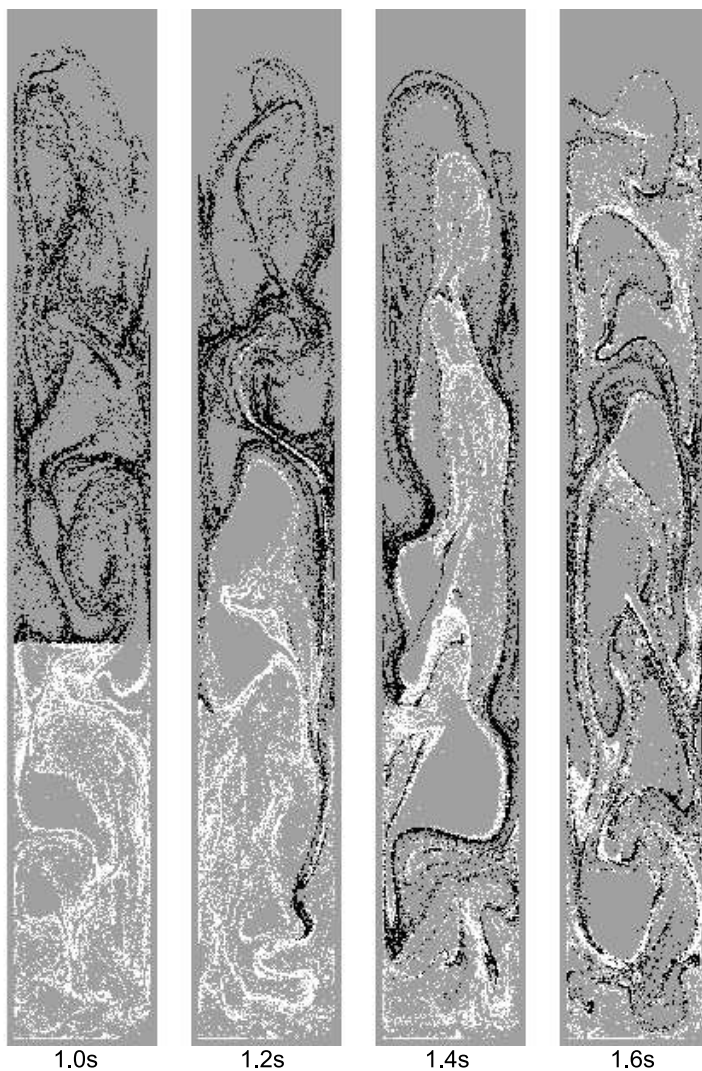


Figure 5.18: Snapshots of vertical mixing at 64 bar.

Table 5.6: Average mixing times

<b>p (bar)</b>	$H_0$ (m)	<b>Vertical <math>t_{mix}</math> (s)</b>	<b>Normalised vertical <math>t_{mix}</math> (-)</b>	<b>Horizontal <math>t_{mix}</math> (s)</b>	<b>Normalised horizontal <math>t_{mix}</math> (-)</b>
2	0.025	1.93	1.0	2.21	1.0
2	0.016	1.69	0.88	1.85	0.84
32	0.025	1.69	1.0	1.52	1.0
32	0.016	1.49	0.89	1.43	0.94

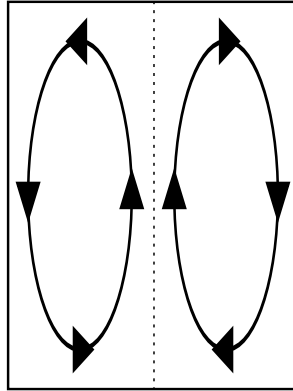


Figure 5.19: Schematic representation of time-averaged solids motion in a fluidized bed.

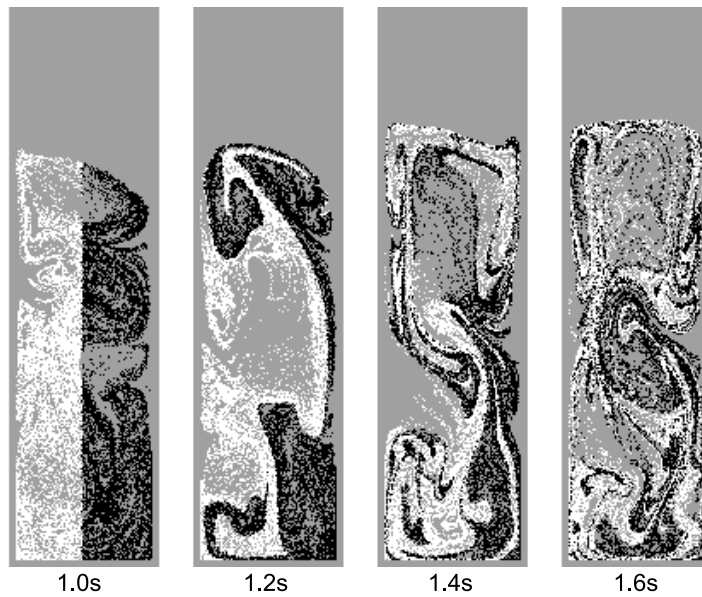


Figure 5.20: Snapshots of horizontal mixing at 1 bar.

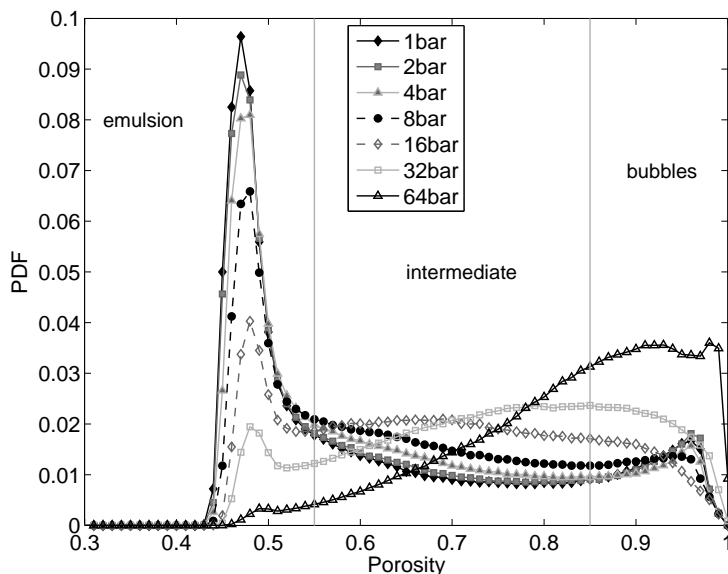


Figure 5.21: Time averaged porosity distribution functions at different operating pressures from TFM simulations.

At pressures below 32 bar, we see a clear peak around a porosity of 40-45%, representing the emulsion phase. Notice that at maximum packing the porosity is about 26%. Above 95% we see some small peaks caused by bubbles. An intermediate area with porosities between 45% and 90% is formed in areas located around bubbles or in developing or collapsing bubbles. With increasing pressure the porosity of the emulsion phase increases, while the bubbles contain more particles. The simulation of 64 bar does not show any peak for the emulsion phase. Hence, in that case there is no clear distinction between the emulsion, intermediate and bubble phases, instead a new peak is formed around 90%. These results are qualitatively in close resemblance to the DPM results, which are shown for reference in Figure 5.22.

## 5.7 Discussion and conclusions

In this chapter we investigated mixing on basis of detailed DPM and TFM simulations using five different methods to calculate mixing in-

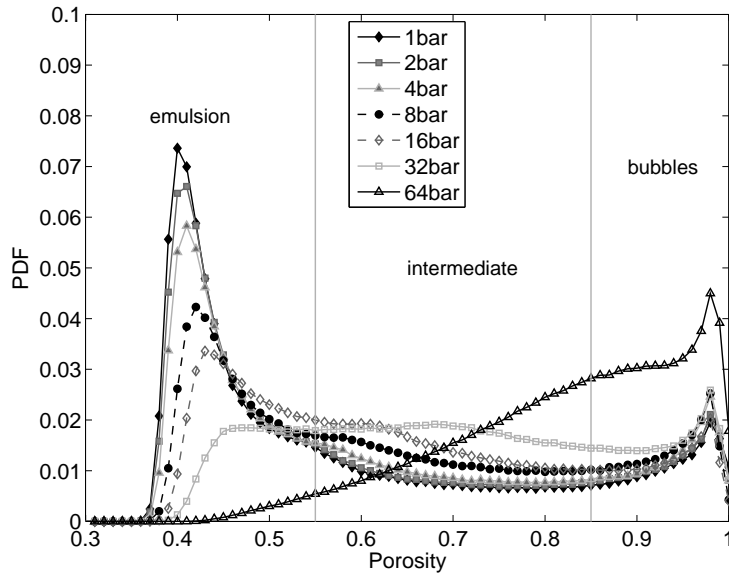


Figure 5.22: Time averaged porosity distribution functions at different operating pressures from DPM simulations.

trices. The nearest neighbours method and the initial neighbour distance method are proposed in this study. Most methods are dependent on the initial colouring of the particles or the applied computational grid. Only the method based on the distance between initial neighbours is grid and colouring independent. This method gives reproducible results with on average errors of 12%.

Besides vertical mixing, also horizontal mixing is investigated. The 95% horizontal mixing times was determined and was found to be of the same order in all directions, which is probably due to the limited size of the simulated system. In larger systems we would expect anisotropic mixing.

The TFM simulations show expected trends and great similarity with the DPM simulations. The effects of increasing pressure on mixing behaviour are determined for vertical and horizontal mixing. For vertical mixing the following observations were made: i) with increasing pressure, the number of bubbles increases, leading to more chaotic particle movement in the bed, which *enhances* vertical (micro) mixing; and ii) expansion of the bed increases particle traveling distances and *decreases* vertical (macro) mixing.

For significantly increased operating pressure, the second effect is dominant.

For horizontal mixing it was found that: i) horizontal mixing occurs partially via rotational movement of particles in the bed. Mixing *decreases* when a fluidized bed expands due to increasing pressure; and ii) direct horizontal motion and mixing of particles *increase* with increasing pressure, due to more chaotic movement in the bed and increasing space between the particles.

For increasing pressures, the latter is dominant and therefore horizontal mixing times are not so much affected by bed height as for lower pressures.

Operating pressure influences the hydrodynamics of the bed significantly: bubbles become smaller and move in a more chaotic fashion, the bubble-emulsion structures becomes less distinct. Furthermore the dense phase becomes less dense at elevated pressure. Since particles have a larger degree of freedom at higher porosities it becomes easier for the particles to mix. In chapter 4 it was discussed that the granular temperature increases with increasing pressure. At high granular temperature the particle velocity has a larger fluctuating component, which enhances mixing.

# 6

## Experimental study of large scale fluidized beds at elevated pressure

### 6.1 Introduction

Industrial fluidized beds for the production of poly-olefines are operated at pressures of typically 20 bars. Research on fluidized beds however is generally performed at atmospheric conditions. Research at elevated pressure is difficult since steel vessels make (visible) access to the flow cumbersome. Although most fluidization research is performed at atmospheric conditions the effects of pressure were investigated by several groups. Most groups use pressure fluctuation measurements to determine regime changes, such as Cai et al. [1990]. Canada and McLaughlin [1978] made a regime map including the pressure effect using pressure fluctuations in a 20 cm fluidized bed. Minimum fluidization velocity and minimum bubbling velocity at elevated pressures has been studied for example by Hoffmann and Yates [1986], Chitester et al. [1984], Sobreiro and Monteiro [1982] up to pressures of 81, 65 and 35 bar, respectively. Besides regime changes Olowson and Almstedt [1990, 1991, 1992] intensively researched bubble behavior at elevated pressure. Using pressure probes Chan et al. [1987] obtained information on properties of individual bubbles. All these researchers used pressure fluctuations as their main information source, since visual access is difficult. For an

overview of research on the effect on operating pressure of fluidization behavior the reader is referred to the review papers by Sidorenko and Rhodes [2004] and Yates [1996].

Details about the flow structure cannot be found using pressure fluctuations. Therefore CFD models were used by Li and Kuipers [2005] and Godlieb et al. [2008]. From their CFD simulations it became clear that the bubble emulsion structure becomes less distinct. In addition small chaotic moving bubbles emerged at elevated operating pressures. More recently, tomography techniques were applied on pressurized fluidized beds to study the evolution of the flow structure. One of the most useful measurement techniques in this respect is electrical capacitance tomography (ECT), which enables the measurement of the porosity distribution in fluidized beds. It is based on the differences in permittivity of the fluidizing gas and the solids material. ECT is a very powerful technique, non-invasive, fast and relatively cheap. Porosity tomograms can be measured at a frequency of up to 100 Hz. A drawback of ECT is the low spatial resolution of about one tenth of the bed diameter. A 30 cm diameter bed was chosen to reduce the wall effect on the fluidization behavior. ECT is able to detect bubbles of 3 cm diameter. To our knowledge, only two groups performed ECT measurements on a fluidized bed operating at elevated pressure. Sidorenko and Rhodes [2004] were the first and they succeeded to perform measurements in a 15 cm bed. Cao et al. [2008] performed ECT measurement in a 20 cm diameter bed up to 11 bar.

It is difficult to define experimental conditions that enable a straightforward comparison of results obtained at different operating pressures. Three approaches were proposed in literature. A constant superficial velocity is not advisable, since the minimum fluidization velocity ( $u_{mf}$ ) decreases with increasing operating pressure. A constant excess velocity is used more frequently and adds a constant value to the minimum fluidization velocity. The third approach is to keep the ratio of the superficial velocity and the minimum fluidization velocity constant. For example Wiman and Almstedt [1998] use a constant excess velocity, assuming that the total bubble volume remains constant. In this work we will compare results obtained from two approaches using: i) a constant excess velocity equal to the minimum fluidization velocity at 1 bar and ii) a superficial velocity equal to three times the minimum fluidization velocity.

Although in industry often chemical reactions occur in the reactor, this work focuses on the fluidization behavior without chemical reactions. In all experiments nitrogen is used as a fluidization agent at room temperature. Nitrogen mimics the behavior of ethylene which is used in industry, since viscosity and density are similar. Nitrogen is used instead of air to avoid dust explosions, which can occur in polymeric dust.

## 6.2 Experimental set-up

In this section, two different concepts for a pressurized fluidized bed are discussed. Moreover a detailed description of the experimental set-up is given.

### 6.2.1 Overall concept

For a 30 cm diameter bed filled with 1.1 mm diameter polymeric particles about  $200 \frac{m^3}{h}$  of nitrogen is required to reach three times the minimum fluidization velocity at atmospheric conditions. This gas flow can be produced by an average blower. For measurements at 20 bar however, about  $1450 \frac{Nm^3}{h}$  of nitrogen is required, which can be produced by a large expensive compressor. The scheme belonging to this concept is shown in Figure 6.1a. The alternative shown in Figure 6.1b pressurizes the entire loop and recirculates the gas. We chose this concept, because it requires much smaller and hence cheaper compressors. The external compressor can be relatively small since the time to pressurize the system is not critical. The internal compressor is very small since it only has to overcome the internal pressure drop.

### 6.2.2 Process description

#### Pressurized blower

The internal blower to recycle nitrogen is designed for atmospheric conditions. It is a roots blower (type DELTA GMA 10.0 DA KDV), supplied by Aerzen B.V. Duiven, which is a positive displacement pump which operates by pulling nitrogen through a pair of meshing lobes. Nitrogen is trapped in pockets surrounding the lobes and carried from the intake side to the exhaust (see Figure 6.3).



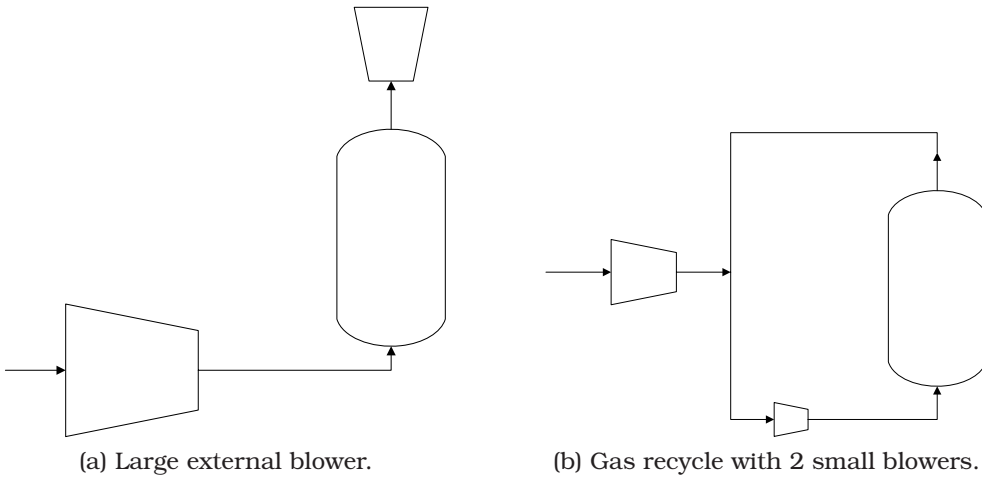


Figure 6.1: Schematic representation of two experimental concepts for the pressurized fluidization setup.

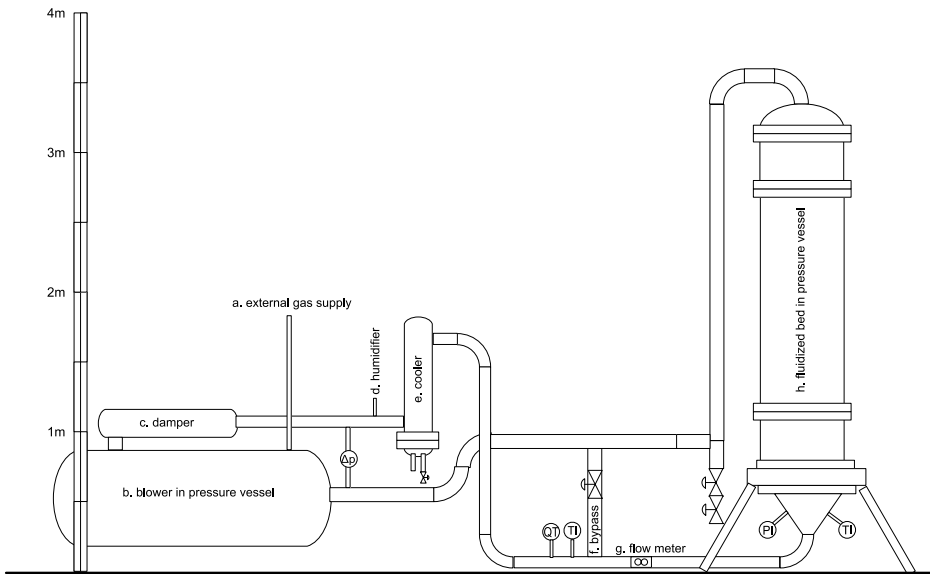


Figure 6.2: layout of the experimental set-up.

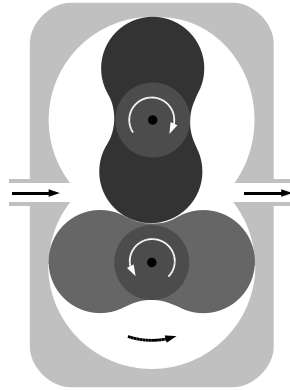


Figure 6.3: Schematic representation of a roots blower with two rotating lobes.

Because of the maximum rotational velocity and the leakage around the lobes the maximum pressure drop of these types of blowers is approximately 800 mbar. Since the pressure drop in the described experimental set-up is below 800 mbar it is a suitable blower. Although the roots blower is not designed to withstand high internal pressures, the blower is entirely placed inside a pressure vessel ensuring a similar pressure inside and outside the blower. The blower operates best at elevated pressures since leakage decreases.

The gap between the lobes should be very narrow and is just a fraction of a millimeter. If glass beads get trapped in this gap they could damage the blower significantly. Fortunately the gas velocity in the blower vessel (Figure 6.2b) is low and entrained glass particles will accumulate in the vessel rather than in the blower. Besides that, there are filters placed on top of the fluidized bed (Figure 6.2h).

The range of operation of the blower is shown in Figure 6.4. Note that the lowest gas velocity is determined by the minimum frequency of the blower. For elevated operating pressures the minimum fluidization velocity drops below the minimum range of the blower. To enable operation at these conditions, a bypass was added to the setup (Figure 6.2f), which enables lower flow rates through the fluidized bed.

The blower produces a fluctuating gas flow. To stabilize the flow a damper is added (Figure 6.2c).

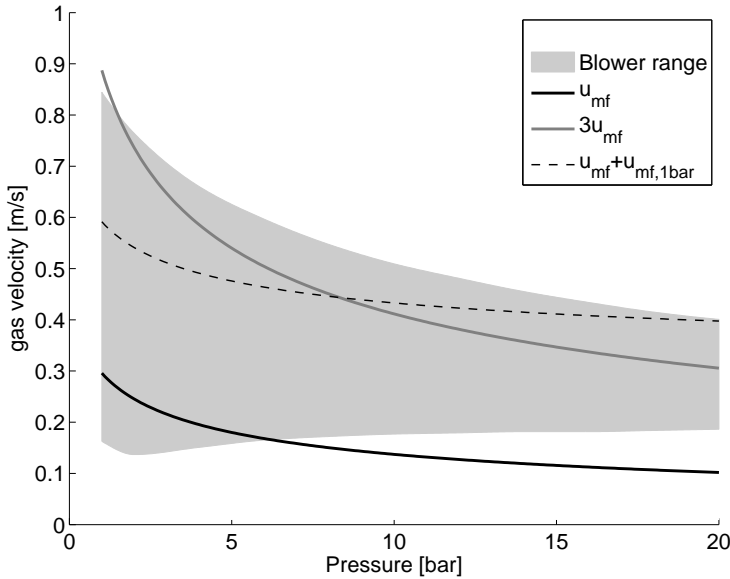


Figure 6.4: Operation range of the blower and typical fluidization velocities for 1.1 mm diameter LLDPE particles.

## Humidifier

Because of friction between particles, particles get charged. The static electricity causes undesired effects such as particles clustering and the formation of sparks. In industry an antistatic agent is usually added at low concentrations to reduce effects of static electricity. Since many antistatic agents used in industry are carcinogenic we prefer to humidify the nitrogen instead. The humidifier sprays water just after the blower (Figure 6.2d). The water droplets vaporize and humidify the gas stream. Water vapor prevents static build up and the related phenomena of clustering and particles sticking to the wall.

Static electricity as such does not affect the ECT measurement, although electric discharges damage the ECT data acquisition module (DAM). Removing the particles from the vessel with a dedicated vacuum cleaner is critical because of rapid static build up.

## Cooler

The blower produces heat that can accumulate in the system, since the system is closed. Therefore, a water cooler is placed just after the blower and the humidifier (Figure 6.2e). Applying the correct cooling rate is important, since too much cooling would result in condensation which would disturb the ECT measurement. In practice, the setup is cooled sufficiently at the tubing and vessel surfaces and the cooler is not required. During warm summer days or long operation at high flow rates it was anticipated that the cooler would be necessary though and therefore included in the design.

## Fluidized bed

The fluidized bed consists of a 30 cm ID PVC tube positioned inside the pressure vessel of 60 cm ID (Figure 6.2h). The bed is filled with particles up to a static height of 60 cm, yielding a bed aspect ratio of two. The ECT measurement technique requires that the setup is made of materials with low conductivity. To this end, the bottom plate is made out of porous PE. A filter is placed on top of the fluidized bed to prevent particles and dust to exit the bed. The set-up is placed in a high-pressure bunker and is fully automatically controlled from outside the bunker.

## Computer

The set-up is controlled by a PC that is placed outside the bunker. At several locations in the set-up temperature, pressure, humidity, flow rate and pressure drop are measured and sent to the PC. The cooler, valves and blower are controlled from the same PC. The ECT measuring technique is controlled separately using an additional PC positioned outside the bunker (see Figure 6.5).

### 6.2.3 ECT Equipment

The ECT sensor consists of twelve electrodes that are placed around the PVC tube. The capacitance measurements are normalized and reconstructed to a  $32 \times 32$  pixel porosity plot, using a Landweber reconstruction algorithm with a relaxation parameter of  $10^{-4}$ , 50 iterations and an inverted Maxwell concentration model. An example of an ECT

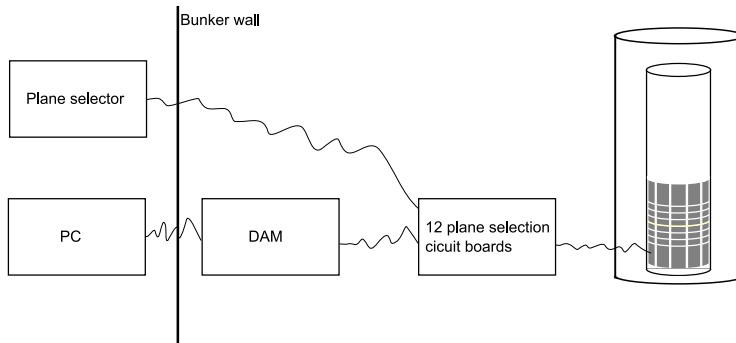


Figure 6.5: Schematic representation of all ECT units. The plane selection box and the ECT laptop are situated outside the bunker. The data acquisition module (DAM) is located inside the bunker. Twelve plane selection circuit boards are placed around the pressure vessel and are connected to the ECT electrodes, which are contained inside the pressure vessel.

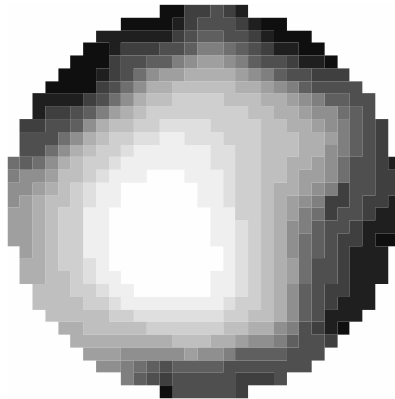


Figure 6.6: Example of a  $32 \times 32$  pixels ECT snapshot of a large bubble moving through the bed. The black color and white color correspond to  $\epsilon_g = 0.4$  and  $\epsilon_g = 1.0$ .

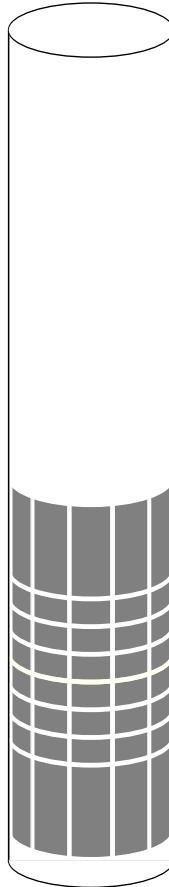


Figure 6.7: Sketch of the ECT sensor placed around the fluidized bed with 6 measurement planes and a guard plane below and above. Each plane consists of 12 electrodes (only 5 are shown here). Height of the inner tube is 150 cm. Height of the guard planes are 17 cm, and each of the 6 measurement planes is 5 cm. The bottom plate of the fluidized bed is situated between the lower guard plane and the lowest measurement plane

measurement result is shown in Figure 6.6. Porosity distributions can be measured for two horizontal planes simultaneously, which are selected from six available planes at different heights. The height of each of the electrodes is 5 cm and the bottom plate is placed directly under the first electrode. Guard planes are placed below and above the measurement planes, each having a height of 17 cm. A schematic representation of the electrodes is shown in Figure 6.7.

Since the data acquisition module (DAM) is able to measure only two planes simultaneously a plane selection system was designed. The plane selection unit is located outside the bunker (see Figure 6.5) and is connected to 12 selection circuit boards that set each of the electrodes to measure or guard. For each electrode and guard electrode, in total  $12 \times 8 = 96$  wires are lead through the wall of the pressure vessel using twelve pressure cable connectors (Conax, Buffalo, US, type PL-16-A12-T-0.5m/1.0m).

Because of the long distance between the electrodes and the plane selection circuit boards the system is very sensitive to external noise. Extensive grounding using aluminum foil improves the signal to noise ratio. Still the system is sensitive to movement of wires, presence of people and poor electrical connections. The measured porosity for a static bed changes significantly over time, i.e sudden jumps and signal drifts are observed over time. Since frequent recalibration of the system is impossible (because the bed cannot be emptied without opening the pressure vessel), we developed a special calibration procedure (see Chapter 3). This procedure assumes that the difference between the full bed capacitance and the empty bed capacitance remains constant. Using this approach only the full bed capacitance is required to recalibrate the ECT system. To make sure that no jumps and signal drift occurs during a measurement the gas flow was stopped at the beginning and end of each to determine the capacitance of the full bed. Figure 6.8 shows an example measurement. Ten seconds after starting the ECT recording the gas supply was activated. It takes about 20 seconds to reach the desired gas flowrate. The next 60 seconds are used for analysis. 20 seconds after the gas supply is stopped, 10 seconds of ECT measurement data is used to check whether the calibration has changed. If the capacitance at the beginning and the end differ more than 5%, the measurement was discarded from further analysis. About one third of all measurements had to be omitted.

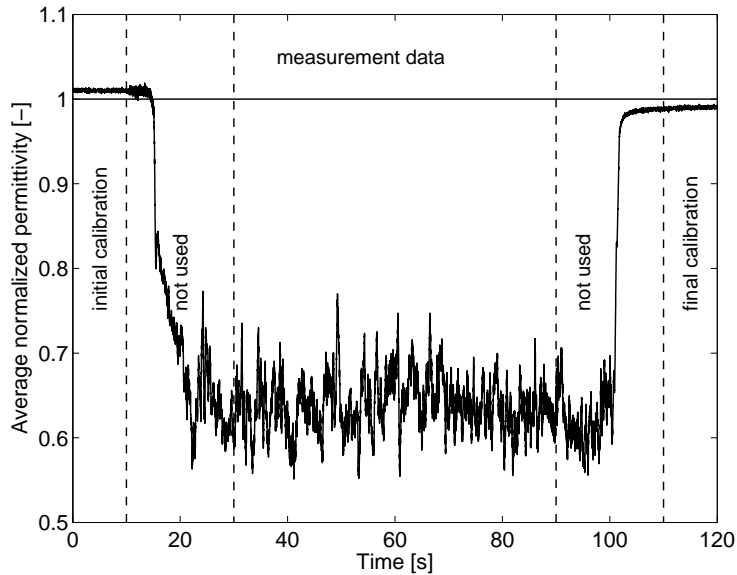


Figure 6.8: Example measurement where the first and last 10 seconds are used to check the calibration. And only the middle minute is used for analysis. This measurement is used since the calibration is just 2% off.

The recorded signals have a noise level of about 5%. It is possible to filter the noise, by taking the median of every 5 frames, whereby the effective measurement frequency drops from 100 Hz to 20 Hz. For porosity distributions this is vital, but for bubble detections this is not preferable, because the reduced measurement frequency makes it hard to track individual bubbles over time.

## 6.3 Results

In this work we present the results of two measurement series. First we will show results for a fluidized bed operated at a constant excess velocity. Subsequently these results are compared to a measurement series for a fluidized bed operated at three times the minimum fluidization velocity. We selected an excess velocity equal to the  $u_{mf}$  at 1 bar (0.3 m/s). The applied gas velocities are listed in Table 6.1 for polymeric particles and in Table 6.2 for glass particles.



Table 6.1: Gas velocity for a constant excess velocity and three times  $u_{mf}$  for 1.1 mm diameter LLDPE particles.

<b>P [bar]</b>	$u_{mf}$	$u_{mf} + u_{mf,1bar}$	$3u_{mf}$
1	0.30	0.59	0.89
2	0.25	0.54	0.74
4	0.20	0.49	0.59
8	0.15	0.45	0.45
16	0.11	0.41	0.34
20	0.10	0.40	0.30

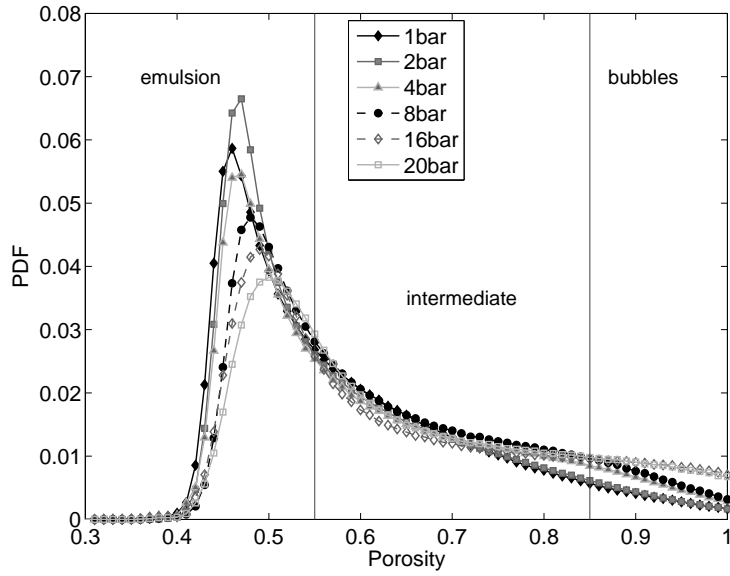
Table 6.2: Gas velocity for a constant excess velocity and three times  $u_{mf}$  for 0.5 mm diameter glass particles.

<b>P [bar]</b>	$u_{mf}$	$u_{mf} + u_{mf,1bar}$	$3u_{mf}$
1	0.21	0.42	0.63
2	0.19	0.40	0.57
4	0.17	0.38	0.50
8	0.14	0.35	0.41
16	0.11	0.32	0.33
20	0.10	0.31	0.30

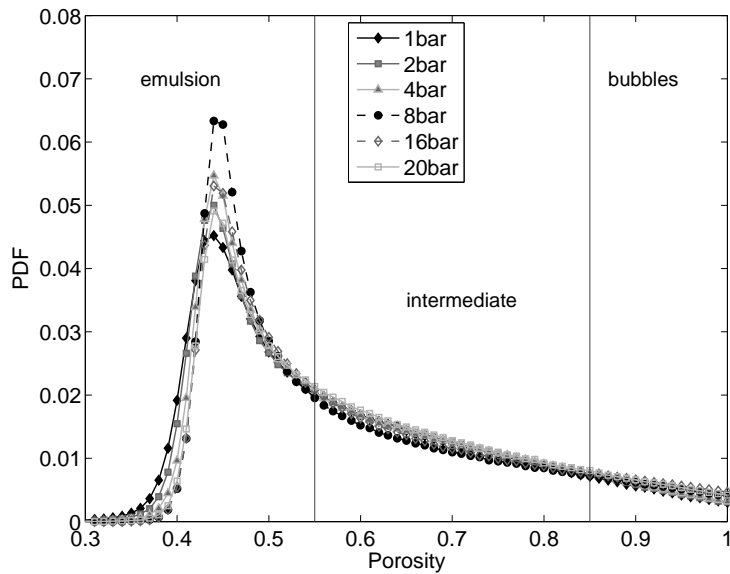
### 6.3.1 Porosity distribution

A probability density function (PDF) of the porosity is a useful representation of the measured porosity distribution. It clearly shows the relative occurrence of the bubble phase and the emulsion phase. The first step in obtaining a porosity PDF is converting the measured normalized permittivity maps into porosity values, for which a 0.6 packing fraction for a randomly filled packed bed is assumed. The final step involves the construction of a histogram of all pixels over all time steps using a porosity bin size of 0.01. For each measurement about 10 million pixels were typically used.

The probability density function (PDF) of the porosity is shown in Figure 6.9. It can clearly be seen that with increasing operating pressure the peak around a porosity of 0.42 moves to higher porosities, in other words the emulsion become less dense with increasing pressure. Although a peak near a porosity of 1.0 is expected representing the presence of bubbles, this is not observed in the results. This is probably due to the low resolution of ECT and smoothing effects of the reconstruction techniques. Especially at high pressures it can be seen that the PDF is not zero at the right side of the plot. In fact about 8% of the PDF is higher than a porosity of 1.0. This unphysical measurement reading has the same origin as the absence of a distinct



(a) LLDPE particles



(b) Glass particles

Figure 6.9: Probability density function (PDF) of the porosity at 10 cm to 15 cm above the distributor. A constant excess velocity of 0.30 m/s above  $u_{mf}$  was used.

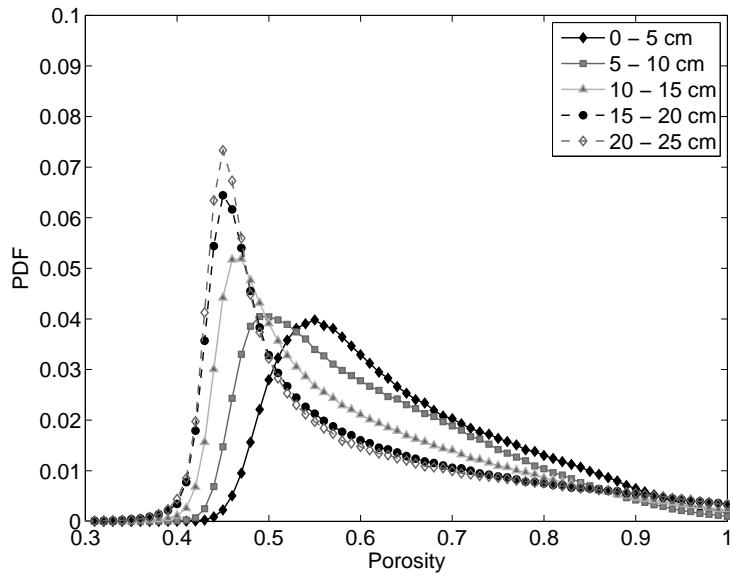
bubble peak. The occurrence of the intermediate zone increases with increasing pressure. For glass particles the effects are less distinct, yet similar to those obtained for LLDPE. Results obtained from CFD simulations as presented in Chapter 4 show similar results as well.

In Figure 6.10 a PDF of the porosity is shown at different heights. It is observed that in the bottom of the bed the intermediate zone occurs more often. The ECT resolution is too low to capture small separate bubbles. With increasing bed height the emulsion phase becomes denser and the bubble sizes increase, because of bubble coalescence. At 20 bar similar trends are observed but curves are shifted to higher porosities. At the lowest plane, just above the bottom plate, at 20 bar the porosity distribution is broad with a maximum at a porosity of 0.68, implying that neither a distinct emulsion phase, nor a distinct bubble phase is clearly observed.

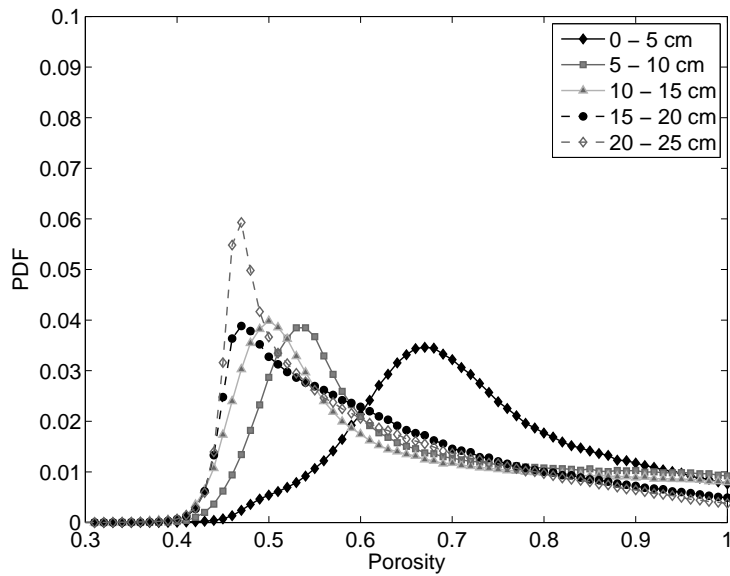
From the time-averaged porosity data, radial profiles were constructed, by dividing the bed into 14 concentric rings, each with the same area containing 58 pixels (see Figure 6.11). The resulting radial porosity distributions are shown in Figure 6.12. A smooth fit is drawn through the measured data points to guide the eye. In the middle of the bed the porosity of the bed is increased with increasing pressure. So the bed expansion takes place in the centre of the bed. At the walls the porosity is slightly decreased. For glass particles similar results are observed, although at pressures exceeding 8 bar the profiles become similar.

### 6.3.2 Porosity fluctuations

Porosity fluctuations are a measure for the bubble size and vigorousness of fluidization. The porosity fluctuation is obtained by taking the standard deviation of the average porosity of a plane. Large bubbles containing no particles cause large fluctuations, while smaller bubbles containing particles cause minor fluctuations. The standard deviations of the porosity obtained at four planes are shown in Figure 6.13. Two trends are observed: i) with increasing height the fluctuations increase, due to bubble coalesce and the presence of large bubbles, and ii) with increasing pressure the fluctuations decrease. The latter is caused by the decrease of bubble size and the less distinct difference between bubbles and emulsion as apparent from in Figure 6.9.



(a) 1 bar



(b) 20 bar

Figure 6.10: Porosity PDF at several heights for LLDPE particles. A constant excess velocity of 0.30 m/s above  $u_{mf}$  was used.

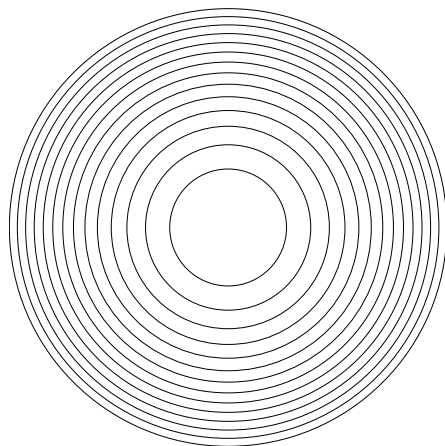


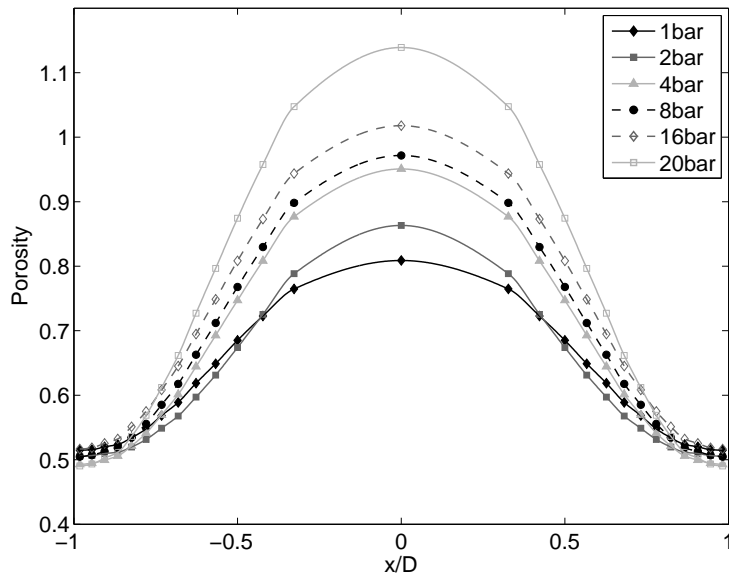
Figure 6.11: For the radial porosity distribution the bed is divided into 14 concentric rings with the same area.

For glass particles the decrease of the fluctuations is rather smooth, while for LLDPE particles the fluctuations decrease from 1 to 6 bar and remain constant for higher pressures. This effect is probably related to the smooth decrease of the minimum fluidization velocity for glass particles and the strong initial decrease in minimum fluidization velocity from 1 to 6 bar for LLDPE particles (see Figure 6.14).

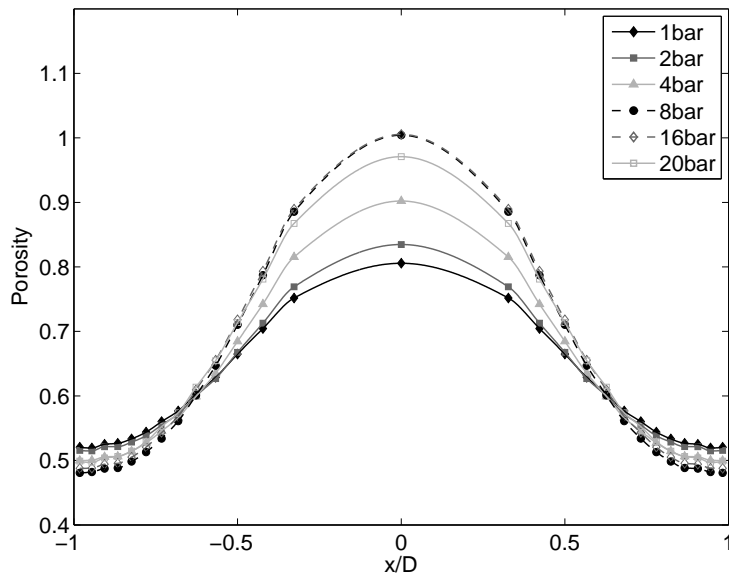
### 6.3.3 Comparison of measurement series

In this section the flow behavior for two different superficial velocities are compared: a constant excess velocity of 0.30 m/s on top of the minimum fluidization velocity, and three times the minimum fluidization velocity. The former is based on the assumption that the excess velocity is responsible for the formation of bubbles. It implies a constant bubble volume production rate at the bottom of the bed. When a superficial velocity of three times the minimum fluidization velocity is used, it is assumed that this gives rise to similar fluidization behaviour.

In Figure 6.15 it was observed that the  $3u_{mf}$  series show a constant PDF of the porosity, whereas the constant excess velocity series shows an increase of the emulsion porosity with increasing operating pressure. This result is confirmed by Figure 6.16, where the average

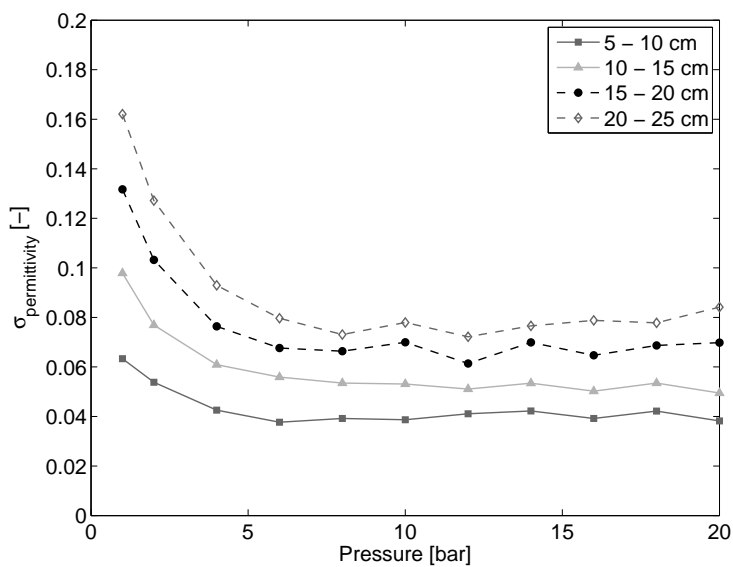


(a) LLDPE particles

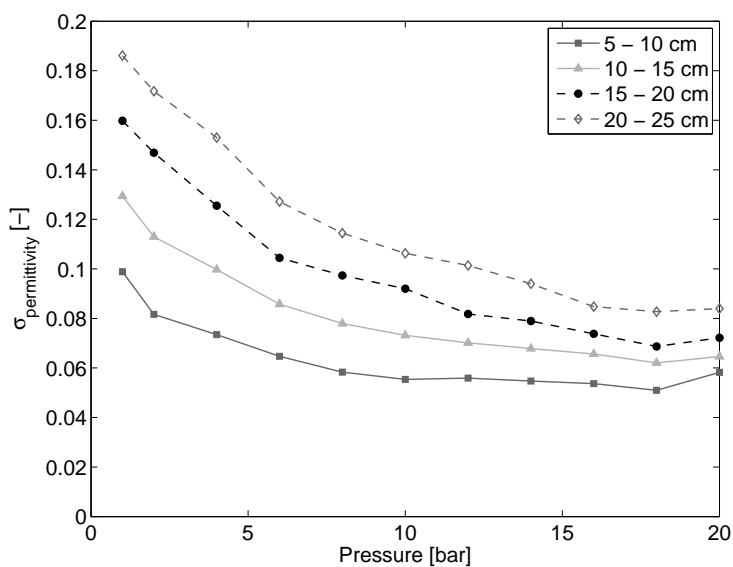


(b) Glass particles

Figure 6.12: Radial porosity distribution at 10 cm to 15 cm above the distributor. A constant excess velocity of 0.30 m/s above  $u_{mf}$  was used.



(a) LLDPE particles



(b) Glass particles

Figure 6.13: Standard deviation of the normalized permittivity at different heights and pressures. A constant excess velocity of 0.30 m/s above  $u_{mf}$  was used.

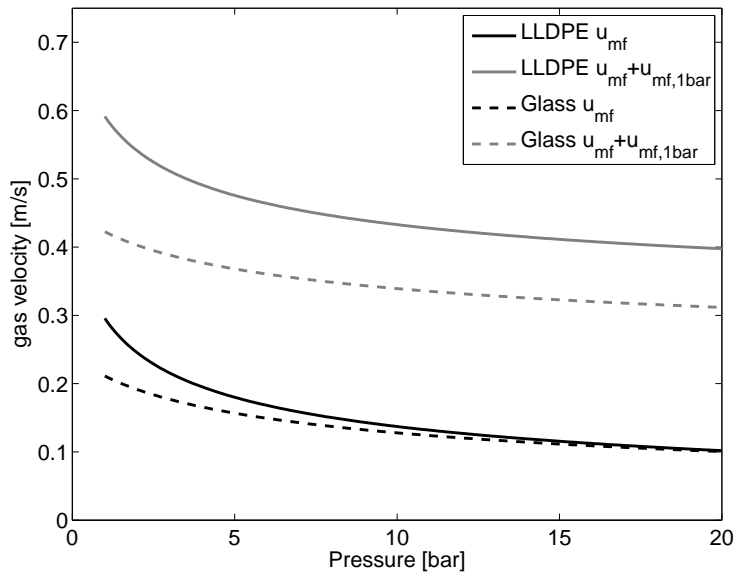


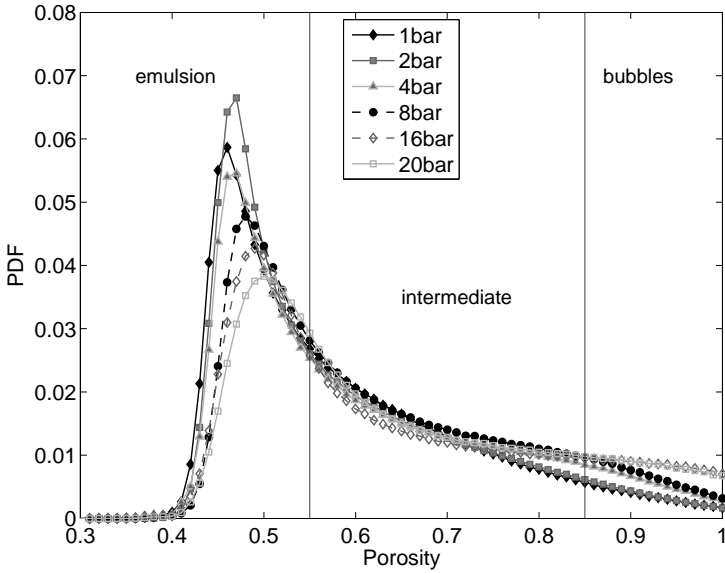
Figure 6.14: Minimum fluidization velocity for 1.1 mm diameter LLDPE particles and 0.5 mm glass particles. The used gas velocities with a constant excess velocity are shown as well.

gas fraction is more or less constant for the  $3u_{mf}$  series, whereas the average gas fraction increases with increasing operating pressure for the constant excess velocity series. For both series it is found that the average gas fraction increases with increasing bed heights, due to bubble coalescence.

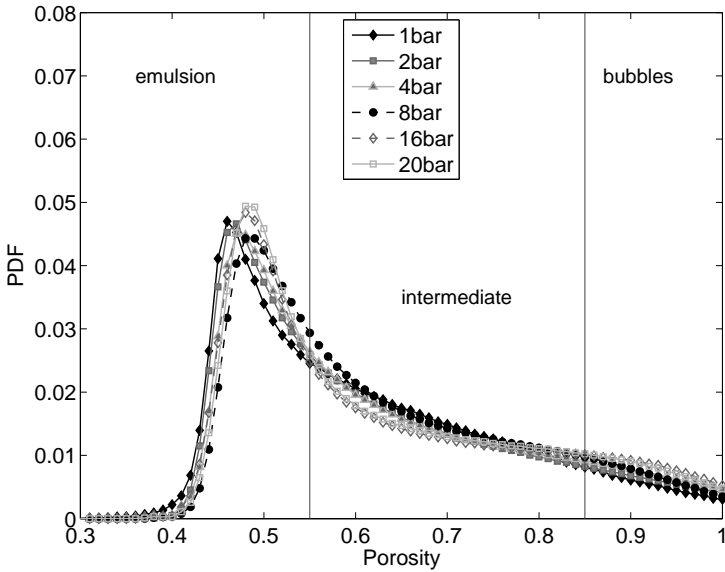
### Cross correlation

The used ECT system enables us to measure at two planes simultaneously. Figure 6.18 shows an example of average plane concentration values for two successive planes. It can be seen that the signal of the top plane has a phase shift compared to the bottom plane. This is caused by the fact that bubbles rising in the bed will pass both planes. The velocity of the bubbles determines the time it takes for them to pass and results in a peak in the signal. The phase shift can be determined with a cross correlation function ( $CCF$ ). This function seeks the best overlapping fit of the two functions by shifting one in time.



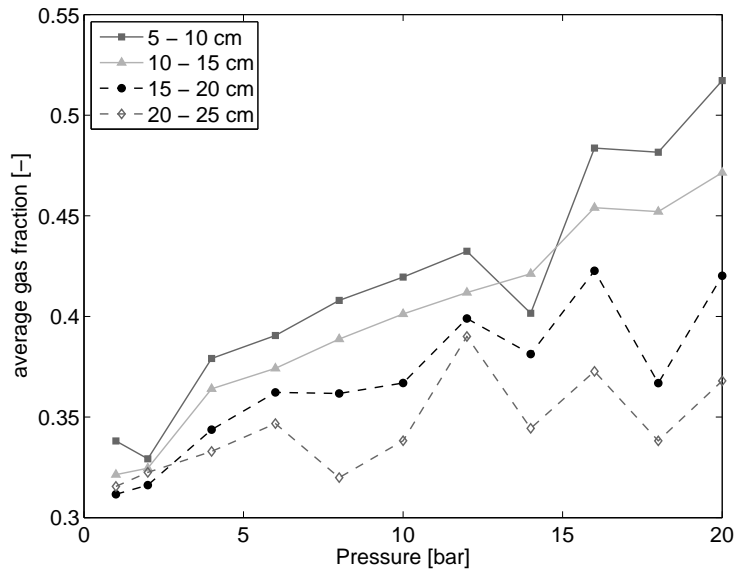


(a) Constant excess velocity



(b) Three times  $u_{mf}$

Figure 6.15: Probability density function (PDF) of the porosity for LLDPE particles at 10 cm to 15 cm above the distributor. A constant excess velocity of 0.30 m/s above  $u_{mf}$  is compared to a measurement series using three times the minimum fluidization velocity.



(a) Constant excess velocity

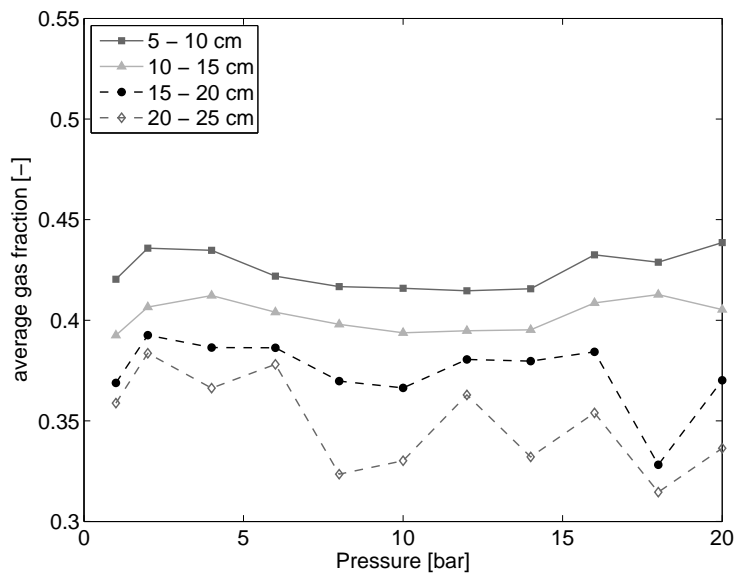
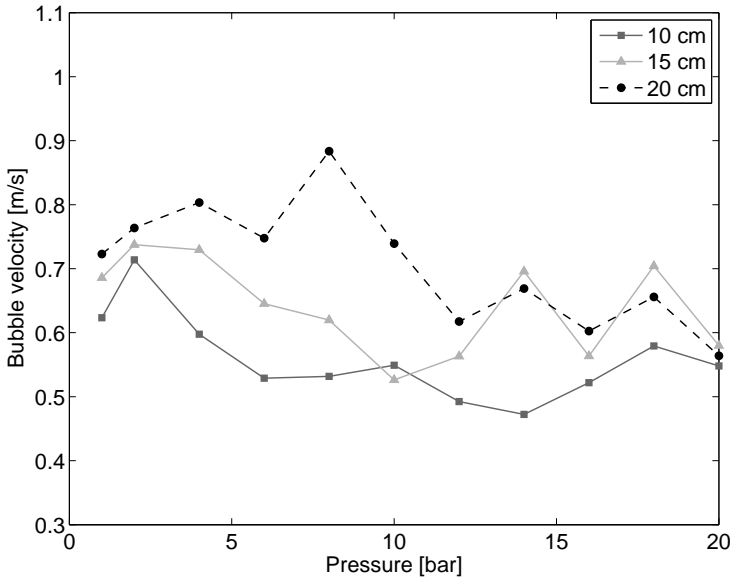
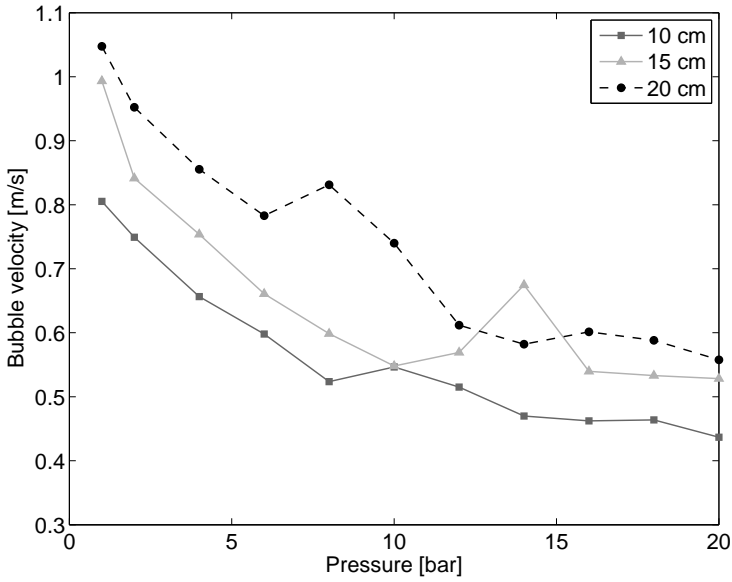
(b) Three times  $u_{mf}$ 

Figure 6.16: Average gas fraction at different heights for LLDPE particles for two measurement series.



(a) Constant excess velocity



(b) Three times  $u_{mf}$

Figure 6.17: Bubble velocity at different heights for LLDPE particles obtained using an overall cross correlation for two measurement series.

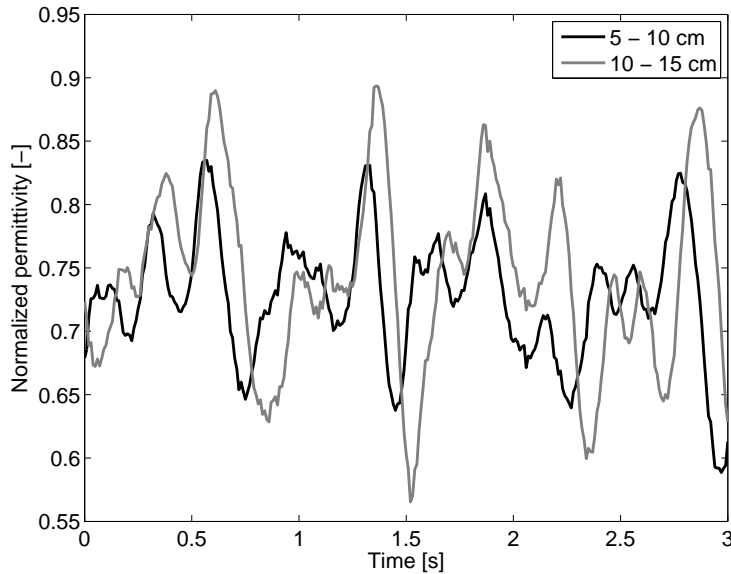


Figure 6.18: Normalized permittivity at neighbouring planes. Bubbles move first through the bottom plane (black) and then through the top plane (grey).

$$CCF = \frac{1}{n} \sum_{t=0}^{t=n} \cdot f_1(t) \cdot f_2(t + m) \quad (6.1)$$

where  $n$  is the number of frames for which the function is applied and  $m$  is the number of frames over which the function is shifted,  $f$  is equal to  $1 - x$ , ensuring that the presence of bubbles (high values of  $f$ ) are being correlated rather than the absence of bubbles (high values of  $x$ ).

The cross correlation function shows a maximum for a certain value of  $m$  (Figure 6.19). A fit can be applied on the cross correlation function to find a better approximation of the maximum value. The derived shift value ( $m$ ) can then be related to a bubble rise velocity using the plane centre distance of 5 cm. As can be observed from Figure 6.18, the phase shift is about 0.05 s. Figure 6.19 confirms this result by showing a peak at  $m = 4$ , corresponding to a time shift of 0.04 s, given the measurement frequency of 100 Hz.

It is interesting to derive a parameter to determine the correlation strength ( $CS$ ) that shows the distinction with which the value for  $m$  was calculated. This can be determined by considering the relative

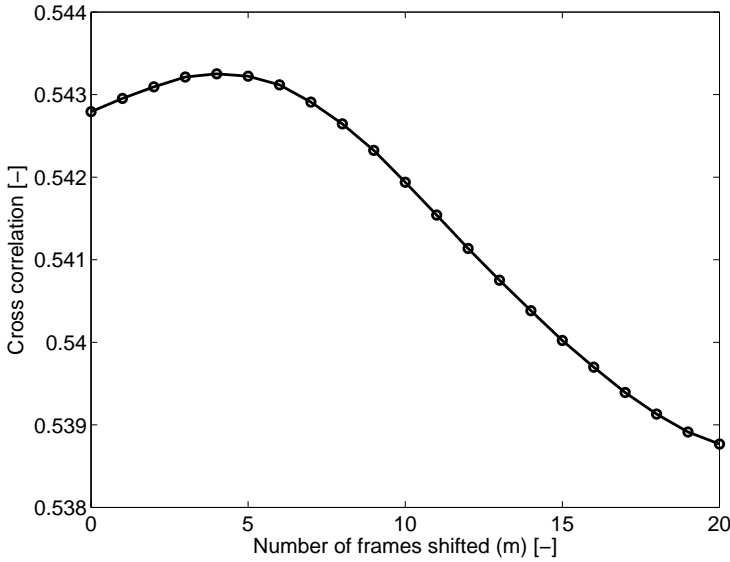


Figure 6.19: Cross correlation result for the data from Figure 6.18.

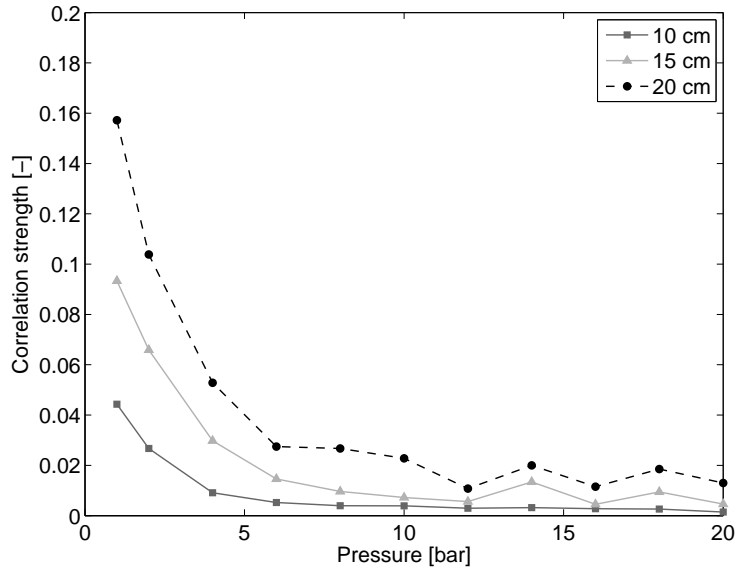
difference between the maximum and minimum value of the correlation:

$$CS = \frac{CCF_{max} - CCF_{min}}{CCF_{max}} \quad (6.2)$$

A very sharp, narrow peak in the cross correlation function indicates that all bubbles rise with similar velocities, while a high variation in velocities will result in a very flat curve.

Surprisingly, the bubble velocity results show rather different trends compared to the average gas fraction results. In Figure 6.17 it can be seen that the average bubble velocity is almost constant for the constant excess velocity series, while it is gradually decreasing for the  $3u_{mf}$  series. It can be concluded that it is not possible to keep the average gas fraction and the bubble velocity the same when the operating pressure is changed. While  $3u_{mf}$  shows a constant porosity distribution and average gas fraction, bubble velocities decrease with increasing operating pressure and the constant excess velocity has a changing porosity distribution and rather constant bubble velocities.

Figure 6.20 shows the correlation strength ( $CS$ ) related to the bubble velocities shown in Figure 6.17. Both series have the same rapid



(a) Constant excess velocity

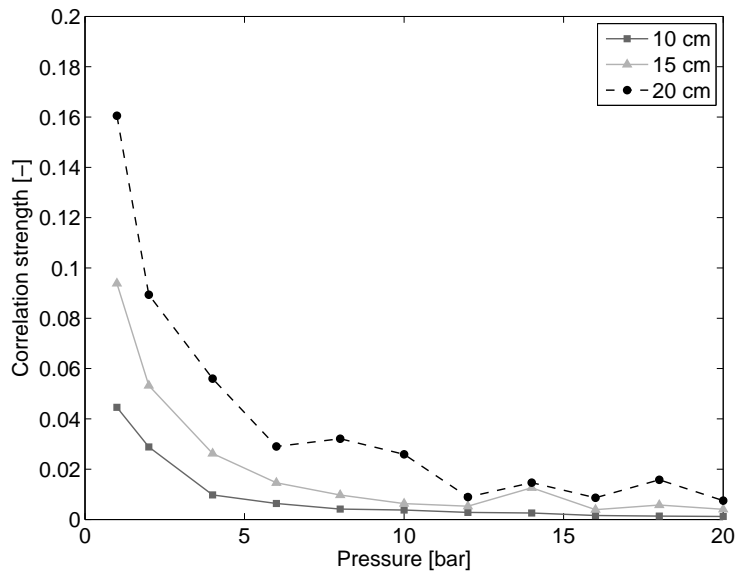
(b) Three times  $u_{mf}$ 

Figure 6.20: Correlation strength for the cross correlation shown in Figure 6.17.

decrease in correlation strength, which indicates that there is a large variety of bubble velocities at elevated pressures.

It can be concluded that it is not possible to keep the average gas fraction and the bubble velocity the same when the operating pressure is changed. While  $3u_{mf}$  shows a constant porosity distribution and average gas fraction, bubble velocities decrease with increasing operating pressure and the constant excess velocity has a changing porosity distribution and rather constant bubble velocities.

## 6.4 Conclusion

In this work ECT was successfully used to investigate the fluidization behavior in a pressurized bed. For experiments with a constant excess velocity it is found that the emulsion phase becomes less dense and more bubbles and intermediate phase appear. Radial porosity distributions show that with increasing pressure the bed expansion occurs mainly in the central portion of the bed. The regions near the walls become slightly denser. Fluctuations in the porosity decrease with increasing pressure, which means that the bubbles become smaller or contain more particles. Finally, it is concluded that using the superficial gas velocity to scale the flow behavior with operating pressure gives ambivalent results. That is to say that experiments with constant excess velocity show constant bubble velocity and changing gas volume fraction, while experiments at three times the minimum fluidization velocity show constant porosity distributions and changing bubble velocities.

# 7

## Epilogue

This thesis contains the results of modelling work and experimental work on pressurized fluidized beds. In this chapter, results from discrete particle model (DPM) simulations, two-fluid model (TFM) simulations and experimental measurements from electrical capacitance tomography (ECT) are compared. Furthermore, overall conclusions are drawn.

### 7.1 Comparison of models and experiments

DPM, TFM and ECT results should be compared with care, because results are calculated differently, with different particles at different velocities. In Figure 7.1, Figure 7.2 and Figure 7.3 probability density functions (PDF) of the porosity are shown for measurement series with a constant excess velocity. In the DPM and TFM, 0.5 mm diameter LLDPE particles at an excess velocity of 0.177 m/s are used, while for the experiments 1.1 mm diameter particles at an excess velocity of 0.3 m/s are used. For the simulations the PDF is obtained from porosities over the entire bed, while for the ECT measurements only porosities are used at 15 to 20 cm above the distributor.

Although the conditions for each of these data sets are not completely the same, overall trends are observed. For DPM, TFM and ECT the emulsion phase becomes less dense with increasing pres-



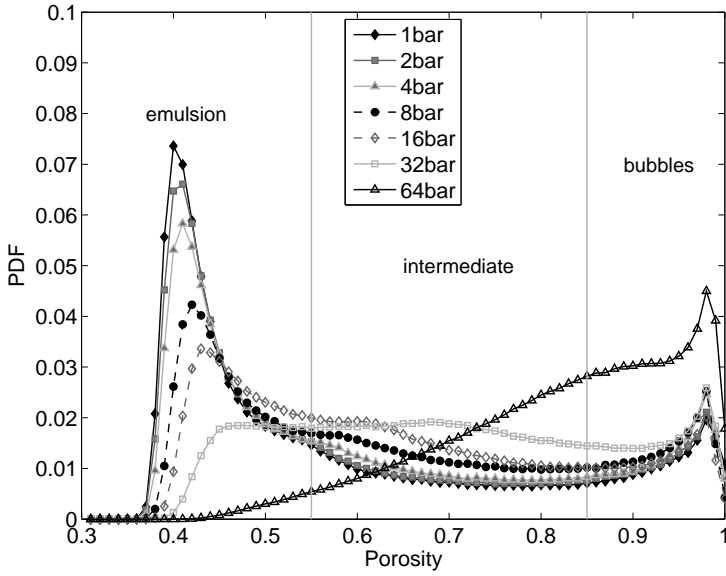


Figure 7.1: Time averaged porosity distribution functions at different operating pressures from DPM simulations.

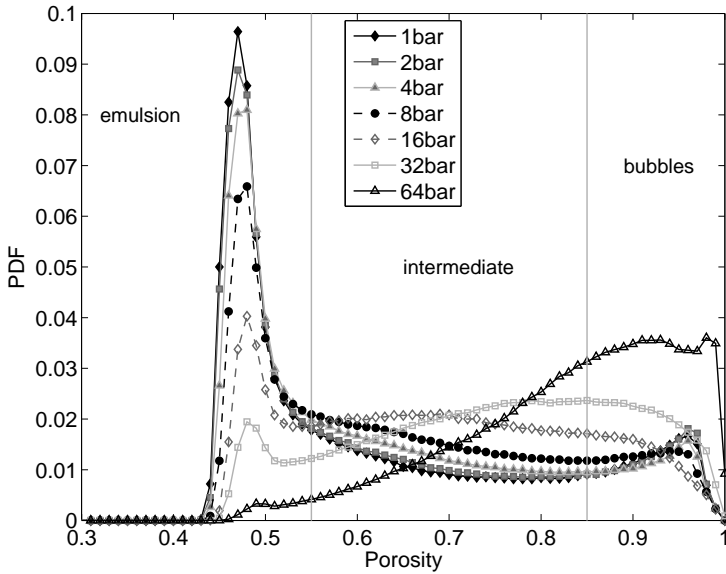


Figure 7.2: Time averaged porosity distribution functions at different operating pressures from TFM simulations.

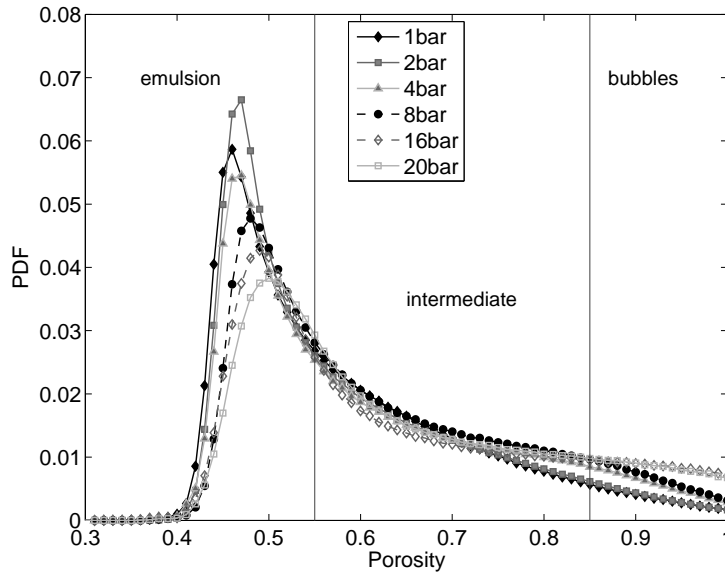


Figure 7.3: Time averaged porosity distribution functions at different operating pressures from ECT measurements.

sure. Furthermore, the bubble and intermediate phase occurs more often as the pressures increases. The main difference between these three results is the absence of a bubble peak for the ECT measurements. This is caused by the smoothing effect of the ECT measurement. An additional difference is the porosity of the emulsion phase. According to the DPM results the emulsion porosity is 0.40, while according to the TFM results and the ECT results it is 0.47. Since the porosity of a randomly packed bed is around 0.40, the results from the DPM are assumed to be most accurate, while the TFM and ECT simulations suffer from smoothing effects. That is to say that, the size of the grid cells (TFM) and the reconstruction techniques (ECT) both have the tendency to blur porosity values. Besides that, the maximum packing fraction is an input parameter for the TFM ( $\epsilon_{s,max} = 0.36$ ) and for the ECT the porosity of a packed bed is set to 0.40. Tuning and investigation of these parameters could possibly improve the results.

The standard deviation in the pressure drop is a measure for the vigorousness of fluidization behaviour. From DPM simulations it is found that pressure drop fluctuations decrease with increasing pressure (see Figure 7.4). Pressure drop was not measured in the experi-

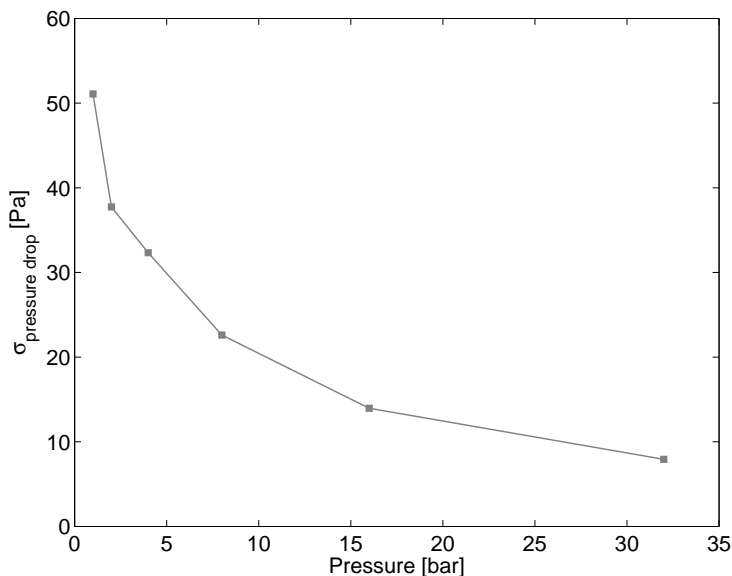


Figure 7.4: Standard deviation in the pressure drop fluctuations of DPM simulations a constant excess velocity of  $2 u_{mf}$ .

mental set-up, although from ECT measurements similar results can be obtained. The fluctuations in the average plane porosity can be measured with ECT. These fluctuations are directly coupled with the pressure fluctuations. The standard deviation of the average plane porosity is shown at different heights in Figure 7.5. Although both figures cannot be compared quantitatively, the observed trends are similar: the fluctuations show a sharp decrease at low operating pressure and decrease slightly or become constant at higher pressure.

## 7.2 Effects of pressure

Although it is very hard to make a fair comparison of fluidization behaviour at varying operating pressures, a few observations and conclusions are presented in this section.

Particles in the same Geldart [1973] group show the same fluidization behaviour at the same multiple value of  $u_{mf}$ . Glass particles ( $\rho = 2526 \frac{\text{kg}}{\text{m}^3}$   $d = 0.5\text{mm}$ ) show similar behaviour as polymeric particles ( $\rho = 750 \frac{\text{kg}}{\text{m}^3}$   $d = 1.1\text{mm}$ ) at three times  $u_{mf}$ . Unfortunately the effect of

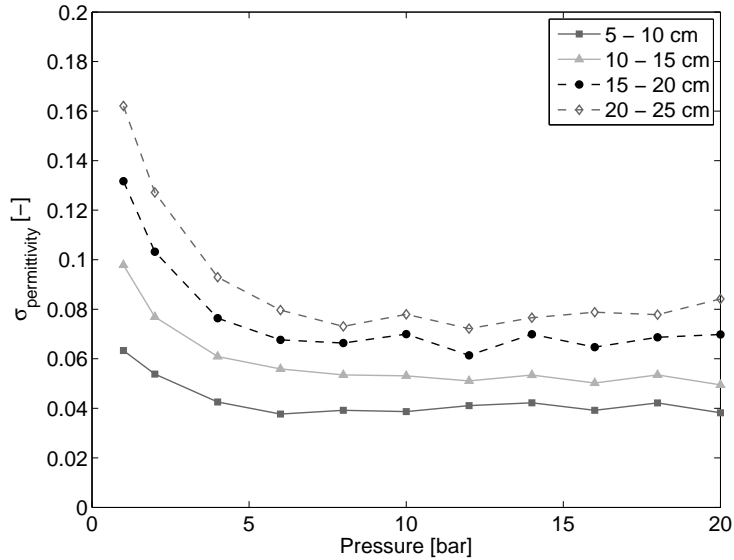


Figure 7.5: Standard deviation of the normalized permittivity at different heights and pressures. A constant excess velocity of 0.30 m/s above  $u_{mf}$  is used.

pressure cannot be incorporated in a simple manner.

According to the Ergun [1952] equation pressure (gas density) influences the  $u_{mf}$ . Two approaches were applied to compare results at different operating pressures: three times  $u_{mf}$  and a constant excess velocity (i.e. superficial velocity minus the minimum fluidization velocity). Experiments with a constant excess velocity show a constant bubble velocity, while experiments at  $3u_{mf}$  show a constant porosity distribution. In other words for porosity structures  $3u_{mf}$  enables a fair comparison, while for bubble behaviour a constant excess velocity does. In the following section only observations of simulations and experiments at a constant excess velocity are presented.

With increasing pressure six observations were made, which are mentioned below

### Emulsion phase becomes more porous.

The emulsion phase becomes more porous with increasing operating pressure. At atmospheric operating pressure the porosity of the emulsion phase is similar to the porosity of a randomly packed bed (0.4),

while at 20 bar the porosity of the emulsion phase rises to 0.5.

#### **Bubble-emulsion structure becomes less distinct.**

In both simulations and experiments it is observed that the clear distinction between bubbles and the emulsion phase gradually disappears with increasing pressure. At atmospheric pressure the emulsion phase is dense and the bubbles are clear voids containing little particles. At high pressure it is no longer possible to observe separate bubbles, although dense and porous regions in the bed still prevail, intermediate porosities occur just as frequent.

#### **Fluidization is more vigorous and bubbles behave more chaotic.**

From animations of simulations results (pressure drop fluctuations and bubble properties) it was observed that the fluidization is more vigorous at elevated pressure. Bubbles move chaotically through the bed and bubbles coalesce and break-up takes place frequently, although it is hard to distinct individual bubbles.

#### **(Micro) mixing is improved via increased granular temperature only caused by increased porosity.**

From DPM and TFM simulations it is observed that solids mixing is improved with increasing operating pressure. Based on DPM simulation results is found that this effect is caused by increased granular temperature. Granular temperature is not directly increased by the elevated operated pressure, but rather via the increased porosity of the emulsion phase, which creates more space for the neighbouring particles to attain different velocities.

#### **Bed expansion limits macro mixing.**

Micro mixing is mixing at the scale of individual bubbles, while macro mixing is at the scale of the entire bed. The micro mixing rate is increased with pressure because of the increased granular temperature. For pressures below 8 bar, macro mixing is enhanced with increasing operating pressure. At higher pressures, the bed expands, which decreases the mixing rate, since particles have to travel larger distances before they can become fully mixed.

## 7.3 Outlook

In this work it has been demonstrated that numerical simulations give detailed quantitative information on the fluidization behaviour of fluidized beds. Since over the past four years computer power increased significantly, this should be used for *more* and *improved* DPM simulations. *More* simulations can be done at different pressures and velocities to get an complete overview of the effect of operating pressure at all regimes. Simulations can be *improved* by studying computationally more expensive systems involving for example: broader particle size distributions (including catalyst particles), non-spherical particles, finer computational grid, cylindrical reactors in stead of cubic reactors.

Since the TFM is suitable to model lab-scale fluidized beds, a 30 cm diameter fluid bed should be simulated to enable a direct comparison to the experimental results obtained in this thesis.

Since pressure fluctuation analysis is commonly used in industry and in academia to investigate fluidization behaviour, ECT results should be directly compared to pressure fluctuations. To measure capacitances and pressure fluctuations simultaneously is not trivial, since the ECT measurement technique is disturbed by the presence of conducting materials, i.e. pressure probes. A solution for this issue needs to be found. Short polymer tubes from the bed to the pressure sensor outside the bed could solve this problem, but will result in some damping in the pressure fluctuation results (see van Ommen et al. [1999]).

ECT is a very powerful technique, but X-ray tomography would produce porosity profiles and distributions with higher resolution. X-ray tomography would enable detailed information about bubble shape, deformation and detailed porosity structures.



# Nomenclature

## Symbols

$C$	Velocity fluctuation	$\frac{m}{s}$
$C$	Capacitance	$F$
$d$	Diameter	$m$
$dt$	Time step	$s$
$e$	Restitution coefficient	—
$\bar{F}$	Force	$N$
$\bar{g}$	Gravitational constant	$\frac{m}{s^2}$
$I$	Moment of inertia	$kgm^2$
$\bar{J}$	Impulse vector	$\frac{kgm}{s}$
$K$	Permittivity distribution	—
$k$	Spring stiffness	$\frac{N}{m}$
$M$	Mixing index	—
$m$	Mass	$kg$
$\bar{n}$	Normal unit vector	—
$N_{part}$	Total number of particles	—
$p$	Pressure	$Pa$
$R$	Particle radius	$m$
$\bar{r}$	Particle position	$m$
$Re$	Reynolds number	—
$S$	Sensitivity map	—
$\bar{S}_p$	Source term	$\frac{kg}{s^2m^2}$
$T$	Torque	$Nm$
$t$	Time	$s$
$\bar{t}$	Tangential unit vector	—
$t_{95\%}$	95% mixing time	$s$
$\bar{u}$	Gas phase velocity	$\frac{m}{s}$
$u_{mf}$	Minimum fluidization velocity	$\frac{m}{s}$
$u_{ex}$	Excess velocity	$\frac{m}{s}$
$V$	Volume	$m^3$
$v$	Particle velocity	$\frac{m}{s}$
$v_\infty$	Slip velocity	$\frac{m}{s}$
$X$	Volume fraction	—



**Greek symbols**

$\beta$	Inter-phase momentum transfer coefficient	$\frac{kg}{m^3 s}$
$\epsilon$	Porosity	—
$\epsilon_r$	relative permittivity	—
$\eta$	Damping coefficient	—
$\theta$	Granular temperature	$\frac{m^2}{s^2}$
$\mu$	Dynamic viscosity	$Pa s$
$\mu$	Friction coefficient	—
$\rho$	Density	$\frac{kg}{m^3}$
$\bar{\tau}$	Stress tensor	$\frac{kg}{s^2 m}$
$\bar{\omega}$	Angular velocity	$\frac{rad}{s}$

**Operators**

$\Delta$	Difference	—
$\nabla$	Gradient	—
$\nabla \cdot$	Divergence	—

**subscripts**

$f$	Fluid
$p$	Particle
$b$	Bubble
$ab$	From particle a to b
$n$	Normal direction
$t$	Tangential direction
$H$	High
$L$	Low
$n$	Normalized
$BP$	Back projection
$E$	Experimentally
$EN$	Experimentally and normalized
$sup$	Superficial
$fit$	Fitted function

**superscripts**

$pp$	Particle to particle
$pw$	Particle to wall
$T$	Transpose

**Abbreviations**

2D	Two dimensional
3D	Three dimensional
CAT	Computer aided tomography
CFD	Computational fluid dynamics
DAM	Data acquisition module
DBM	Discrete bubble model
DPM	Discrete particle model
EFD	Experimental fluid dynamics
ERT	Electrical resistance tomography
FCRE	Fundamentals of chemical reaction engineering
KTGF	Kinetic theory of granular flow
LBM	Lattice Boltzmann model
LBP	Linear back projection
LLDPE	Linear low density polyethylene
MRI	Magnetic resonance imaging
PC	Personal computer
PDF	Probability density function
PE	Polyethylene
PET	Positron emission tomography
PP	Polypropylene
PVC	Polyvinyl chloride
TFM	Two-fluid model



## Bibliography

- B.N. Asmar, P.A. Langston, and A.J. Matchett. A generalised mixing index in distinct element method simulation of vibrated particulate beds. *Granular Matter*, V4(3):129–138, 2002.
- R. Beetstra, M.A. Van der Hoef, and J.A.M. Kuipers. A lattice-boltzmann simulation study of the drag coefficient of clusters of spheres. *Computers and Fluids*, 35(8-9):966 – 970, 2006.
- G.A. Bokkers, M. van Sint Annaland, and J.A.M. Kuipers. Mixing and segregation in a bidisperse gas-solid fluidised bed: a numerical and experimental study. *Powder Technology*, 140(3):176–186, 2004.
- G.A. Bokkers, J.A. Laverman, M. van Sint Annaland, and J.A.M. Kuipers. Modelling of large-scale dense gas-solid bubbling fluidised beds using a novel discrete bubble model. *Chemical Engineering Science*, 61(17):5590 – 5602, 2006.
- P. Cai, Y. Jin, Z.-Q. Yu, and Z.-W. Wang. Mechanism of flow regime transition from bubbling to turbulent fluidization. *AIChE Journal*, 36(2):955–956, 1990.
- G.S. Canada and M.H. McLaughlin. Large particle fluidization and heat transfer at high pressures. *AIChE. Symposium Series*, 74(19): 27–37, 1978.
- J. Cao, Z. Cheng, Y. Fang, H. Jing, Huang J., and Y. Wang. Simulation and experimental studies on fluidization properties in a pressurized jetting fluidized bed. *Powder Technology*, 183(1):127 – 132, 2008.
- J. Centrella and J.R. Wilson. Planar numerical cosmology. ii. the difference equations and numerical tests. *Astrophysical Journal Supplement Series*, 54:229–249, 1984.
- I.H. Chan, C. Sishla, and T.M. Knowlton. The effect of pressure on bubble parameters in gas-fluidized beds. *Powder Technology*, 53(3): 217–235, 1987.

- D.C. Chitester, R.M. Kornosky, L.-S Fan, and J.P. Danko. Characteristics of fluidization at high pressure. *Chemical Engineering Science*, 39(2):253–261, 1984.
- P.A. Cundall and O.D.L. Strack. A discrete numerical model for granular assemblies. *Geotechnique*, 29(1):48–64, 1979.
- A. Darelus, A. Rasmuson, B. van Wachem, Niklasson B.I., and S. Folestad. CFD simulation of the high shear mixing process using kinetic theory of granular flow and frictional stress models. *Chemical Engineering Science*, 63(8):2188–2197, 2008. 0009-2509.
- D. Darmana, N.G. Deen, and J.A.M. Kuipers. Parallelization of an euler-lagrange model using mixed domain decomposition and a mirror domain technique: Application to dispersed gas-liquid two-phase flow. *Journal of Computational Physics*, 220(1):216 – 248, 2006.
- J.F. Davidson and D. Harrison. *Fluidized Particles*. Cambridge University Press, 1963.
- N.G. Deen, M. van Sint Annaland, and J.A.M. Kuipers. Multi-scale modeling of dispersed gas-liquid two-phase flow. *Chemical Engineering Science*, 59(8-9):1853 – 1861, 2004.
- T. Dyakowski, R. B. Edwards, C. G. Xie, and R. A. Williams. Application of capacitance tomography to gas-solid flows. *Chemical Engineering Science*, 52(13):2099–2110, 1997.
- S. Ergun. Fluid flow through packed columns. *Chemical Engineering Progress*, 48:89–94, 1952.
- G.J. Finnie, N.P. Kruyt, M. Ye, C. Zeilstra, and J.A.M. Kuipers. Longitudinal and transverse mixing in rotary kilns: A discrete element method approach. *Chemical Engineering Science*, 60(15):4083–4091, 2005.
- D. Geldart. Types of gas fluidization. *Powder Technology*, 7(5):285–292, 1973.
- D. Gera. On the computation of granular temperature and effective normal stresses in fluidized beds. In *Fluidization X*, Beijing, China, 2003. 341-345.

- D. Gidaspow. *Multiphase flow and fluidization: Continuum and kinetic theory descriptions*. Academic Press, 1994.
- W. Godlieb, N.G. Deen, and J.A.M. Kuipers. Characterizing solids mixing in DEM simulations. In *6th International Conference on Multiphase Flow, ICMF 2007*, page 140, Leipzig, Germany, 2007a.
- W. Godlieb, N.G. Deen, and J.A.M. Kuipers. A discrete particle simulation study of solids mixing in a pressurized fluidized bed. In *The 12th International Conference on Fluidization*, pages 751 – 758, Vancouver - Canada, 2007b.
- W. Godlieb, N.G. Deen, and J.A.M. Kuipers. On the relationship between operating pressure and granular temperature: a discrete particle simulation study. *Powder Technology*, 182(2):250 – 256, 2008.
- M.J.V. Goldschmidt, J.A.M. Kuipers, and W.P.M. van Swaaij. Hydrodynamic modelling of dense gas-fluidised beds using the kinetic theory of granular flow: effect of coefficient of restitution on bed dynamics. *Chemical Engineering Science*, 56(2):571 – 578, 2001.
- M.J.V. Goldschmidt, R. Beetstra, and J.A.M. Kuipers. Hydrodynamic modelling of dense gas-fluidised beds: Comparison of the kinetic theory of granular flow with 3d hard-sphere discrete particle simulations. *Chemical Engineering Science*, 57(11):2059–2075, 2002.
- B. Gompertz. On the nature of the function expressive of the law of human mortality, and on a new mode of determining the value of life contingencies. *Philosophical Transactions of the Royal Society London*, 110:513–584, 1825.
- A.C. Hoffmann and J.G. Yates. Experimental observations of fluidized beds at elevated pressures. *Journal Chemical Engineering Communications*, 41(1-6):133–149, 1986.
- B.P.B. Hoomans, J.A.M. Kuipers, W.J. Briels, and W.P.M. van Swaaij. Discrete particle simulation of bubble and slug formation in a two-dimensional gas-fluidised bed: A hard-sphere approach. *Chemical Engineering Science*, 51(1):99–118, 1996.
- B.P.B. Hoomans, J.A.M. Kuipers, and W.P.M. van Swaaij. Granular dynamics simulation of segregation phenomena in bubbling gas-fluidised beds. *Powder Technology*, 109(1-3):41–48, 2000.

- S.M. Huang, A Plaskowski, C.G. Xie, and M.S. Beck. Capacitance-based tomographic flow imaging system. *Electronics Letters*, 24(7): 418–419, 1988.
- Ø. Isaksen. A review of reconstruction techniques for capacitance tomography. *Measurement Science and Technology*, 3:325–337, 1996.
- A.H. Kharaz, D.A. Gorham, and A.D. Salman. Accurate measurement of particle impact parameters. *Measurement Science and Technology*, 10(1):31, 1999.
- D.L. Koch and R.J. Hill. Inertial effects in suspension and porous-media flows. *Annual Review of Fluid Mechanics*, 33(1):619–647, 2001.
- D. Kunii and O. Levenspiel. *Fluidization Engineering*. Butterworth-Heinemann, Boston, London, Singapore, Sydney, Toronto, Wellington, 1991.
- P.C.M. Lacey. Developments in theory of particulate mixing. *International Journal of Applied Chemistry*, 4:257, 1954.
- L. Landweber. An iterative formula for fredholm integral equations of the first kind. *Am. J. Math.*, 73:615–624, 1951.
- J. Li and J.A.M. Kuipers. On the origin of heterogeneous structure in dense gas-solid flows. *Chemical Engineering Science*, 60(5):1251–1265, 2005.
- J.M. Link. *Development and validation of a discrete particle model of a spout-fluid bed granualator*. PhD thesis, University of Twente, 2006.
- J.M. Link, L.A. Cuypers, N.G. Deen, and J.A.M. Kuipers. Flow regimes in a spout-fluid bed: A combined experimental and simulation study. *Chemical Engineering Science*, 60(13):3425–3442, 2005.
- L.-S. Lu and S.-S. Hsiau. Mixing in vibrated granular beds with the effect of electrostatic force. *Powder Technology*, 160(3):170–179, 2005.
- Y.T. Makkawi and P.C. Wright. Fluidization regimes in a conventional fluidized bed characterized by means of electrical capacitance tomography. *Chemical Engineering Science*, 57(13):2411–2437, 2002a.

- Y.T. Makkawi and P.C. Wright. Optimization of experiment span and data acquisition rate for reliable electrical capacitance tomography measurement in fluidization studies - a case study. *Measurement Science and Technology*, 13(12):1831, 2002b.
- Y.T. Makkawi and P.C. Wright. Electrical capacitance tomography for conventional fluidized bed measurements—remarks on the measuring technique. *Powder Technology*, 148(2-3):142–157, 2004.
- J.J. McCarthy, D.V. Khakhar, and J.M. Ottino. Computational studies of granular mixing. *Powder Technology*, 109(1-3):72–82, 2000.
- N. Mostoufi and J. Chaouki. Local solid mixing in gas-solid fluidized beds. *Powder Technology*, 114(1-3):23–31, 2001.
- J.J. Nieuwland, M. van Sint Annaland, J.A.M. Kuipers, and W.P.M. van Swaaij. Hydrodynamic modeling of gas/particle flows in riser reactors. *AIChE Journal*, 42(6):1569–1582, 1996.
- P.A. Olowson and A.E. Almstedt. Influence of pressure and fluidization velocity on the bubble behaviour and gas flow distribution in a fluidized bed. *Chemical Engineering Science*, 45(7):1733–1741, 1990.
- P.A. Olowson and A.E. Almstedt. Influence of pressure on the minimum fluidization velocity. *Chemical Engineering Science*, 46(2):637–640, 1991.
- P.A. Olowson and A.E. Almstedt. Hydrodynamics of a bubbling fluidized bed: influence of pressure and fluidization velocity in terms of drag force. *Chemical Engineering Science*, 47(2):357–366, 1992.
- N. Reinecke and D. Mewes. Recent developments and industrial/research applications of capacitance tomography. *Measurement Science and Technology*, 7(3):233, 1996.
- M.J. Rhodes, X.S. Wang, M. Nguyen, P. Stewart, and K. Liffman. Study of mixing in gas-fluidized beds using a DEM model. *Chemical Engineering Science*, 56(8):2859–2866, 2001.
- M.A.I. Schutyser, J.T. Padding, F.J. Weber, W.J. Briels, A. Rinzema, and R. Boom. Discrete particle simulations predicting mixing behavior of solid substrate particles in a rotating drum fermenter. *Biotechnology and Bioengineering*, 75(6):666–675, 2001.



- I. Sidorenko and M.J. Rhodes. Influence of pressure on fluidization properties. *Powder Technology*, 141(1-2):137–154, 2004.
- L.E.L. Sobreiro and J.L.F. Monteiro. The effect of pressure on fluidized bed behaviour. *Powder Technology*, 33(1):95–100, 1982.
- A.N. Tikhonov and V.Y. Arsenin. *Solutions of ill-posed problems*. V. H. Winston & Sons, Washington, D.C.: John Wiley & Sons, New York-Toronto, Ont.-London, 1977.
- M.A. Van der Hoef, R. Beetstra, and J.A.M. Kuipers. Lattice-boltzmann simulations of low-reynolds-number flow past mono- and bidisperse arrays of spheres: results for the permeability and drag force. *Journal of Fluid Mechanics*, 528(-1):233–254, 2005.
- M.A. Van der Hoef, M. Ye, M. van Sint Annaland, A.T. Andrews, S. Sundaresan, and J.A.M. Kuipers. Multiscale modeling of gas-fluidized beds. In *Advances in Chemical Engineering*, volume 31, pages 65–149. Academic Press, 2006.
- M.A. Van der Hoef, M. van Sint Annaland, N.G. Deen, and J.A.M. Kuipers. Numerical simulation of dense gas-solid fluidized beds: A multiscale modeling strategy. *Annual Review of Fluid Mechanics*, 40(1):47–70, 2008.
- J.R. van Ommen, J.C. Schouten, M.L.M. vander Stappen, and C.M. van den Bleek. Response characteristics of probe transducer system for pressure measurements in gas solids fluidized beds: how to prevent pitfalls in dynamic pressure measurements. *Powder Technology*, 106:199–218, 1999.
- D.R. Van Puyvelde. Comparison of discrete elemental modelling to experimental data regarding mixing of solids in the transverse direction of a rotating kiln. *Chemical Engineering Science*, 61(13):4462–4465, 2006.
- G. Verkerk, J.B. Broens, W. Kranendonk, F.J. van der Puijl, J.L. Sikkema, and C.W. Stam. *Binas, informatieboek vwo-havo voor het onderwijs in de natuurwetenschappen*. Wolters-Noordhof, 1986.
- W. Warsito and L.-S. Fan. 3d-ect velocimetry for flow structure quantification of gas-liquid-solid fluidized beds. *Canadian Journal of Chemical Engineering*, 81(3-4):875–884, 2003.

- Y.C. Wen and Y.H. Yu. Mechanics of fluidization. *Chemical Engineering Progress Symposium*, 62:100–111, 1966.
- J. Wiman and A.E. Almstedt. Influence of pressure, fluidization velocity and particle size on the hydrodynamics of a freely bubbling fluidized bed. *Chemical Engineering Science*, 53(12):2167–2176, 1998.
- Li Y. and W. Yang. Image reconstruction by nonlinear landweber iteration for complicated distributions. *Measurement Science and Technology*, 19(9):094014, 2008.
- W.Q. Yang and M. Byars. An improved normalisation approach for electrical capacitance tomography. In *1st World Congress on Industrial Process Tomography*, Buxton, UK, 1999. 215.
- W.Q. Yang and L. Peng. Image reconstruction algorithms for electrical capacitance tomography. *Measurement Science and Technology*, 14(1):R1, 2003.
- J.G. Yates. Effects of temperature and pressure on gas-solid fluidization. *Chemical Engineering Science*, 51(2):167–205, 1996.
- X. Yin and S. Sundaresan. Fluid-particle drag in low-reynolds-number polydisperse gas-solid suspensions. *AIChE Journal*, 55(6):1352–1368, 2009a.
- X. Yin and S. Sundaresan. Drag law for bidisperse gas-solid suspensions containing equally sized spheres. *Industrial and Engineering Chemistry Research*, 48(1):227–241, 2009b.



# List of Publications

## Journal papers

1. N.G. Deen, W. Godlieb, S. Gorter, and J.A.M. Kuipers. Numerical analysis of solids mixing in pressurized fluidized beds. *Industrial & Engineering Chemistry Research*, in press.
2. W. Godlieb, N.G. Deen, and J.A.M. Kuipers. On the relationship between operating pressure and granular temperature: a discrete particle simulation study. *Powder Technology*, 182(2):250-256, 2008.
3. J.M. Link, W. Godlieb, N.G. Deen, and J.A.M. Kuipers. Discrete element study of granulation in a spout-fluidized bed. *Chemical Engineering Science*, 62(1-2):195-207, 2007a.

## Conference proceedings

1. N.G. Deen, W. Godlieb, S. Gorter, and J.A.M. Kuipers. An electrical capacitance tomography study of pressurized fluidized beds. In *Fluidization XIII*, Korea, 2010, in press.
2. W. Godlieb, N.G. Deen, and J.A.M. Kuipers. Discrete particle simulations of high pressure fluidization. In *CHISA 17th International Congress Of Chemical And Process Engineering*, paper 856, Prague, Czech Republic, 2006.
3. W. Godlieb, N.G. Deen, and J.A.M. Kuipers. Characterizing solids mixing in DEM simulations. In *6th International Conference on Multiphase Flow, ICMF 2007*, page 140, Leipzig, Germany, 2007a.
4. W. Godlieb, N.G. Deen, and J.A.M. Kuipers. A discrete particle simulation study of solids mixing in a pressurized fluidized bed. In *The 12th International Conference on Fluidization*, pages 751-758, Vancouver - Canada, 2007b.
5. W. Godlieb, S. Gorter, N.G. Deen, and J.A.M. Kuipers. Dem and tfm simulations of solids mixing. In *Seventh International*

Conference on Computational Fluid Dynamics in the Minerals and Process Industries, Melbourne, Australia, 2009.

6. J.M. Link, W. Godlieb, P. Tripp, N.G. Deen, S. Heinrich, M. Peglow, J. Kumar, J.A.M. Kuipers, M. Schönherr, and L. Mörl. Comparison of fibre optical measurements and discrete element simulations for the study of granulation in a spout fluidized bed. In WCPT5: 5th World Congress on Particle Technology, Orlando, Florida, 2006a.
7. J.M. Link, W. Godlieb, P. Tripp, N.G. Deen, S. Heinrich, M. Peglow, J. Kumar, J.A.M. Kuipers, M. Schönherr, and L. Mörl. Discrete element modeling and fibre optical measurements for fluidized bed spray granulation. In 15th International Drying Symposium, 20-23 August 2006 (paper A 0315), Budapest, Hungary, 2006b.
8. J.M. Link, W. Godlieb, P. Tripp, N.G. Deen, S. Heinrich, J.A.M. Kuipers, and M. Schönherr, M. Peglow. Comparison of fibre optical measurements and discrete element simulations for the study of granulation in a spout fluidized bed. In 3rd International Granulation Workshop, 27-29 June 2007, Sheffield, UK, 2007b.

## Curriculum Vitae

Willem Godlieb werd op 30 april 1979 geboren in Groningen. Hij bracht zijn jeugd door in Zuidhorn en Nieuwe Pekela en bezocht het Winkler Prins College te Veendam.

In september 1998 startte hij met de opleiding Chemische Technologie aan de Universiteit Twente in Enschede. In het kader van deze opleiding liep hij van maart tot en met juli 2003 stage bij Unilever Research te Vlaardingen. In maart 2005 studeerde hij af bij de werkeenheid Fundamentele Aspecten van de Proceskunde (FAP) op de ontwikkeling van een model voor granulatie in een spout geïndustrialiseerd bed.

In juni 2005 trad hij in dienst bij de werk-eenheid FAP om als promovendus een promotieonderzoek te verrichten op het effect van druk op fluidisatie gedrag. De resultaten van dit onderzoek staan beschreven in dit proefschrift.